UNIVERSITÀ DEGLI STUDI DI ROMA

"TOR VERGATA"

FACOLTA' DI INGEGNERIA

DOTTORATO DI RICERCA IN MATERIALI PER L'ENERGIA E L'AMBIENTE

XXI CICLO

Tailoring Materials for Intermediate Temperature Solid Oxide Fuel Cells (IT-SOFCs) Based on Ceramic Proton Conducting Electrolyte

Emiliana Fabbri

A.A. 2008/2009

Docente Guida/Tutor: Proff. Silvia Licoccia and Enrico Traversa

Coordinatore: Prof. Enrico Traversa

To my strong mother

Felix qui potuit rerum cognoscere causas
(Happy he, who has availed to read the causes of things)
Virgilio, Georgiche, II, 489

Acknowledgements

I would like to thank Prof. Silvia Licoccia and Prof. Enrico Traversa. I want to thank them for the patience they had each day I went in their office, for their motivating spirit which encouraged me to go on with my work. Thanks to them for their reproaches and compliments, for the moments they made me gratified and for the moments they made me stronger. It is not only culture what they could teach to me, thank you for the scientist I will become (hopefully).

Thanks to my strong mom. And about that, there would be too much to say. Thank to my family, they all are always so proud of me.

Thanks to my best friends, Alessia, Giorgia, and Simona. I could not do the same in my life without them. If I can go away, it is also thanks to you.

I would like to thanks to Alessandra, for all the time we spent together in the laboratory…..and especially because the beginning is always the hardest time! Thanks to Barbara…because, what is life without gossip! Thanks to Elisabetta for every time she was like a mom with me. Thanks to Cadia for the help. Thanks to Vincenzo, not only for EIS, but for the time he was strong and the time he gave me helpful advice. Thanks to Debora, because for her kindness…and because she made me fall in love with Tokyo! Thanks to Daniele, not only for the thin (this time really thin) film.

Thanks to my colleagues of Tor Vergata University of Rome. Thanks to Francesco Bozza, he enlarged my patience so much. Thanks to Corrado for his songs. Thanks to Francesco Basoli, for his kindness (too much Fra!). Thanks to my American friend, Eric. Thanks to Simone, he is absolutely the funniest. Thank to Laure, because she took me for the first time to NY…my first experience in another world! And thanks to Marco, Milan, Sherif, Zakarya, Catia, Fang; Alma, Chiara, Stefano, Antonio, Alberto, Paolo, Giovanni, Andrea, Masami, Sugata, and to those who I heve forgot (there should be someone) for all the time we spend together. Thank also to my Korean friends at the University of Florida.

Thanks to all the friends who make my days: Fra, Vale, Andrew, Simone, Bartolo, Pietro, Arianna, Luca, Ricky.

Thanks to my dogs, Ettore and now Cesare, we studied hard together.

Table of Contents

List of Figures

Part A: Literature Background

Part B: Experimental Results

List of Tables

PART A: Literature Background

PART B: Experimental Results

Introduction

There are increasing reasons to explore alternatives to conventional energy generation methods (that is to say coal-fired steam turbine and gasoline internal combustion engine). From an ecological point of view, there is the need to reduce the polluting by-products of conventional energy generation. From a socio-economical standpoint, the worldwide demand for energy continues to rise as more and more nations join the group of the industrialized countries, while hydrocarbon fuels go to exhaustion. Finally, from a socio-political perspective, the situation described above has created several and often dramatic tensions between different world economic areas, as evidenced by frequent wars. Lowering the global dependence on oil might reduce such tensions. However, despite all of this, changes in the energy generation methods are extremely slow, as evidenced by the wide (if we cannot say total) use of the internal combustion engine.

The concept of alternative energy has been introduced a long time ago. Several different sources of energy are proposed, which can have the potential to replace conventional generation methods. Popular examples include solar radiation, wind motion, and nuclear fusion. Each of these technologies has its own set of problems that have slowed down its commercialization, but much research is being conducted to overcome these problems. In fact, the research towards the development of alternative, highly efficient, eco-friendly energy production technologies is expanding. There is a general push towards higher efficiencies. At present, automobiles based on internal combustion engines have an overall efficiency of about 20-30%. That is, only 20-30% of the thermal energy content of the gasoline is converted into useful mechanical work and the rest is wasted. Higher efficiencies translate into reduced energy costs per unit of work done.

Fuel cells, an alternative energy technology, have received growing interest in recent years since they represent one of the most promising energy production systems to reduce pollutant emissions. They are electrochemical devices that allow the direct conversion of chemical energy into electrical energy.

Among the different type of fuel cells, solid oxide fuel cells (SOFCs) offer great promise as a clean and efficient technology for energy generation and provide significant environmental benefits. They produce negligible hydrocarbons, CO or NOx emissions, and, as a result of their high efficiency, about one-third less CO_2 per kW/h than internal combustion engines. Unfortunately, the current SOFC technology based on a stabilized zirconia electrolyte requires the cell to operate from 700 to 1000°C to avoid unacceptable ohmic losses. These high operating temperatures demand specialized (expensive) materials for fuel cell interconnectors, long start-up time, and large energy input to heat the cell up to the operating temperature. Therefore, if fuel cells could be designed to give a reasonable power output at intermediate temperatures (IT, 400-700°C), tremendous benefits may result. In particular, in the IT range ferrite steel interconnects can be used instead of expensive and brittle ceramic materials. In

addition, sealing becomes easier and more reliable; rapid start-up is possible; thermal stresses (namely, those caused by thermal expansion mismatches) are reduced; electrode sintering becomes negligible. Combined together, all these improvements result in reduced initial and operating costs.

Therefore, the major trend in the present research activities on SOFCs is the reduction of the operating temperature. The problem is that lowering the operating temperatures lowers the electrolyte conductivity, whereas the electrode polarization greatly increases, reducing the overall fuel cell performance. Considering the described scenario, it is clear how the study of materials assumes a considerable role in lowering SOFC operating temperature.

Making SOFCs commercially competitive with conventional energy generation methods means developing a highly efficient and environmental friendly energy production device to provide for a global sustainable energy system. IT-SOFCs represent not only a laboratory research activity, but a great challenge for the entire society.

The purpose of the present dissertation is the development of a stable highly-conductive electrolyte and performing electrodes for lower temperature SOFCs.

Chapter 1A presents the physico-chemical principles of SOFCs functioning, the demands imposed on the components materials, together with a literature survey on the state of-the art technology. Starting from more “conventional” oxygen ion conducting electrolytes, the need for reducing the operation temperature leads to a discussion on the properties of proton conducting materials as a feasible alternative to reach the goal of fabricating an IT-SOFCs.

Chapter 2A describes the main properties of ceramic proton conductors. Several perovskite-type oxides, such as doped $BaCeO_3$, $SrCeO_3$, $BaZrO_3$, and $SrZrO_3$, show proton conductivity in the IT range when exposed to hydrogen and/or water vapour containing atmospheres. They are generally known as high temperature proton conductors (HTPCs). The main challenge in the field of HTPC is to find a compound that concurrently satisfies two of the essential requirements for fuel cell application, namely high proton conductivity and good chemical stability under fuel cell operating conditions.

The second part of this dissertation describes the experimental results achieved during the research carried out.

In view of the considerations given in Chapter 2A, Chapter 1B describes the optimization of the sol-gel procedure to prepare Yttrium doped Barium Zirconate (BZY) proton conductor electrolyte. Producing BZY powders with controlled compositional homogeneity and microstructure using a proper synthesis method was expected to improve the electrochemical performance of this electrolyte. The same sol-gel procedure was also used to synthesize $BaCe_{0.8}Y_{0.2}O_{3-\delta}$ (BCY) proton conductor electrolyte. The performance of the synthesized BZY and BCY proton conductors were examined in terms of chemical, microstructural, and electrochemical characteristics

Chapter 2B presents the application of the optimized synthetic procedure to the preparation of different proton conductor electrolytes. To further improve the electrochemical performance of barium zirconate electrolyte, the B-site of the BZY perovskite structure was doped with Ce producing several

$BaZr_{0.8-x}Ce_xY_{0.2}O_{3-\delta}$ compounds ($0.0 \leq x \leq 0.8$). The prepared samples were analyzed in terms of chemical stability, electrical conductivity, microstructural characteristics, and finally under fuel cell tests.

Chapter 3B describes a different approach for the preparation of a performing HTPC electrolyte. To obtain a highly conductive and chemically stable proton conductor electrolyte, a sintered Y-doped barium cerate (BCY) pellet was protected with a thin BZY layer, grown by pulsed laser deposition. The overall performance of the bilayer electrolyte turned out to be of great interest for practical use in IT-SOFCs application. However, the measured fuel cell performances were negatively affected by the interface of the Pt electrodes with the BZY layer. For this reason the development of a superior cathode was considered to be crucial to make IT-SOFCs based on proton conductors competitive with the more established SOFCs using oxygen-ion conductor electrolytes. Such issue was addressed in Chapter 4B.

PART A: LITERATURE BACKGROUND

Chapter 1: Solid Oxide Fuel Cells (SOFCs)

1.1 Fuel Cells: General Aspects

Fuel cells are electrochemical energy conversion devices which can continuously convert the chemically energy of a fuel and an oxidant into electrical energy and heat, without involving direct combustion as an intermediate step.[1]

Recently, fuel cells technology has become highly appealing because of their potential ability to reach high efficiencies.[2]

In addition, fuel cells are attractive energy systems because of their low environmental impact and their modular nature, so that they can be built in a wide range of power requirements as an environmental friendly system.[3]

The range of their applications is extremely vast, including: battery replacement in small portable electronic devices, major and/or auxiliary power units in vehicles, residential combined heat and power generation unit, and large-scale (megawatt size) electrical power station.[1]

The basic structure, or building block, of a fuel cell consists of an anode and a cathode separated by an electrolyte. The operating principle is similar to that of a battery, with the fundamental difference that in a fuel cell the chemical energy is provided by a fuel and an oxidant stored outside the cell, allowing fuel cell power generation as long as the reactants are supplied to the electrodes.[4]

There are several types of fuel cells. They can be classified by the electrolyte type, the operating temperature, the charged mobile species in the electrolyte, and whether the fuel is reformed outside or inside the cell.[5,6] The most common classification of fuel cells is by the type of electrolyte and includes:

- *Proton Exchange Membrane Fuel Cell (PEMFC).*
- *Alkaline Fuel Cell (AFC).*
- *Phosphoric Acid Fuel Cell (PAFC).*
- *Molten Carbonate Fuel Cell (MCFC).*
- *Solid Oxide Fuel Cell (SOFC).*

Figure 1.1 illustrates state-of-the art of fuel cell electrolytes, together with the mobile ionic species, the operating temperature, and fuels and materials typically utilized.

Operating at high temperatures reduces ohmic losses and favours electrode activity. However, especially for portable applications, a relatively low working temperature would be preferred as it enables rapid start-up and minimizes the thermo-mechanical stresses induced by thermal cycling.

Solid electrolyte systems obviate the need to contain corrosive liquids and thus solid oxide and polymer electrolyte fuel cells are generally preferred by many developers over alkali, phosphoric acid or molten carbonate fuel cells.

In particular, PEMFCs have garnered much attention especially because of their potential applicability to transportation systems. One problem of this type of fuel cells is that the electrolyte membrane is fairly permeable to fuel molecules (such as hydrogen and methanol), thus reducing their performance.

AFCs, though providing high power densities, are considered by most impractical because of their reactivity with CO_2, which leads to the formation of non-conducting alkali carbonates in the electrolyte. Nevertheless, some commercialization efforts are underway.

PAFCs, the leading technology in the early 1990s, have been largely abandoned because of their inability to reach high power density.

MCFCs, because of the high operating temperature, are widely used for stationary power generation system. This fuel cell technology is able to reach high efficiency, but presents the disadvantage of containing a corrosive liquid as electrolyte.

Research and development efforts in SOFC technology continue in both industrial and academic laboratories across the world. SOFCs obviate the need to contain corrosive liquids and offer fuel flexibility, high efficiency, modularity and reliability. Most of those efforts are directed toward large scale stationary power system development. Furthermore, SOFCs have recently shown promising potential applications on smaller scale power supply units for auxiliary systems.[4,5,7].

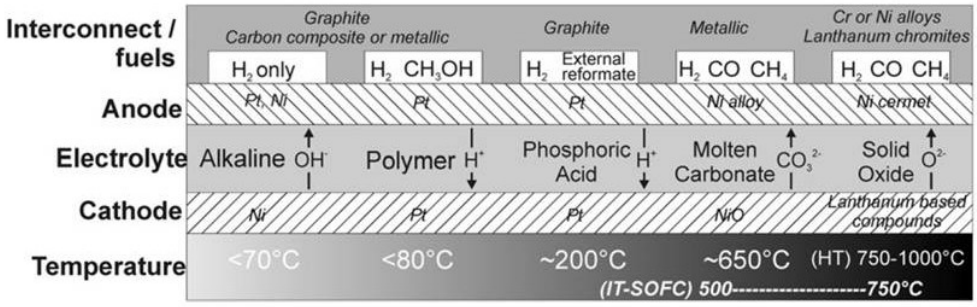

Figure 1.1: Summary of different types of fuel cells, including operation temperature and materials used.[1]

1.2 Solid Oxide Fuel Cells: Basics

SOFCs are solid state devices that use an ion-conducting ceramic material as electrolyte. Their typical operating temperature is from 700 to 1000°C and thus they are generally classified as *high temperature (HT) fuel cells.*

This type of fuel cell provides many advantages over traditional energy conversion systems including high efficiency, reliability, modularity, fuel adaptability, and very low levels of NO_x and SO_x emissions. Compared to the other fuel cell technology, the main SOFCs benefit is the use of a solid electrolyte. A great advantage offered by SOFC is also fuel flexibility, allowing a variety of hydrocarbon fuels to be utilized. Furthermore, because of their high operating temperature, natural gas fuel can be reformed within the cell stack eliminating the need for an expensive, external reformer. Solid oxide fuel cells have shown very high reliability when operated continuously. For example, a 100 kW system fabricated by Siemens-Westinghouse has successfully produced power for over 20.000 hours without any measurable degradation in performance.

All the above highlighted advantageous characteristics make SOFCs a potential competitive power generation system.[5,7,8]

The basic SOFC cell consists of two electrodes in contact with a dense ceramic electrolyte. To obtain higher power and voltage output with respect to a single SOFC, individual cells are connected in series to form a 'stack'. In a fuel cell stack each cell is electrically connected to its adjacent in series, anode with cathode, using an electrically conducting interconnector which also serves to distribute reactants across the surface of the electrodes by properly designed flow channels [1]

The SOFC ceramic electrolyte must allow oxygen ions (O^{2-}) to migrate from the air electrode (cathode) to the fuel electrode (anode) where they react with the fuel (H_2, CO, etc.) to generate an electrical voltage. The negative electrode (anode) must promote the oxidation of the fuel, while the positive electrode (cathode) must catalyze the reduction of the oxidant.

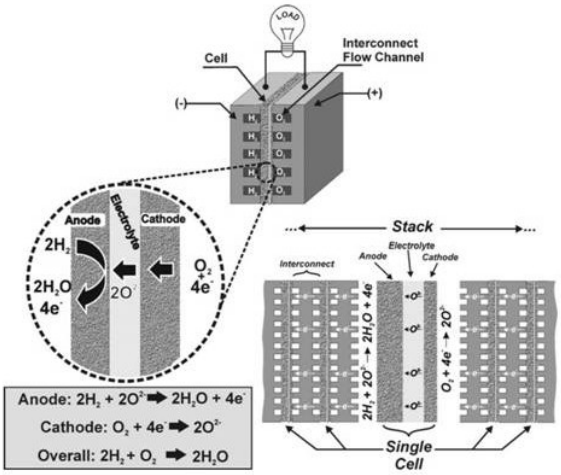

Figure 1.2: Scheme of a SOFC operation (with hydrogen as fuel) and assembly of cells into stacks. [1]

During operation, oxygen molecules combine with the electrons supplied by the cathode, being reduced into oxygen ions, which are then injected into the electrolyte (Equ. 1.a):

$$\frac{1}{2}O_{2c} + 2e^- \Leftrightarrow O_e^{2-} \tag{1.a}$$

where the subscripts ‘c’ and ‘e’ stand for cathode and electrolyte, respectively.

The process of the oxygen ions moving through the electrolyte can be thought as an equivalent process of oxygen vacancies (which can be considered simply as point defects in a periodic oxide lattice, where a normally occupied oxygen site is left vacant) migrating from the anode side towards the cathode side, which is given by Equ. 1.b using the Kröger-Vink notation:

$$\frac{1}{2}O_2 + 2e^- + V_O^{\bullet\bullet} \leftrightarrow O_O^x \tag{1.b}$$

The electrolyte, conducting ions, must block electrons. When the oxygen ions emerge on the anode side of the electrolyte, they react with fuel (for example H_2) to form H_2O and electrons:

$$O_e^{2-} + H_{2a} \leftrightarrow H_2O + 2e^- \tag{2}$$

where the subscript ‘a’ stands for anode.

Electrons produced during the last reaction are released to the anode (which is also electrically connected to the external circuit). Thus the circuit is complete and useful work can be done in the external circuit.[8]

Combining Equ.1.a and Equ.2, the overall SOFC basic reaction is thus:

$$\frac{1}{2}O_2 + H_2 \leftrightarrow H_2O \tag{3}$$

1.3 SOFC Performance

1.3.1 Thermodynamic Concepts

Considering a fuel cell as a reversible system, the change in Gibbs free energy (ΔG) associated to the fuel cell basic reaction corresponds to the maximum electrical work (W_{el}) available for conversion into usable work:

$$W_{el} = \Delta G = -nFE_{rev} \tag{4}$$

Where: n is the number of electrons involved in the cell reaction,
F is the Faraday constant,
E_{rev} is the reversible open circuit voltage of the cell.

Therefore, the reversible cell voltage is related to the variation of the Gibbs free energy via:

$$E_{rev} = \frac{-\Delta G}{nF} \tag{5}$$

Reactant partial pressures and concentrations affect the Gibbs free energy, and thus the cell voltage. The reversible cell voltage at given temperature and pressure can be calculated by the so called *Nernst Equation*: [8,9]

$$E_{rev} = E^0 + \frac{RT}{nF}\ln\left(\frac{p_{H_2} \cdot {p_{O_2}}^{1\backslash 2}}{p_{H_2O}}\right) \tag{6}$$

Where: E° is the reversible cell voltage at standard pressure
pressures are in bar,
water is produced in the form of steam.

However, the actual operating voltage is decreased with respect to the reversible open circuit voltage (Equ.5) because of irreversible processes, which will be examined in the following paragraph.

1.3.2 Polarization Curve

The performance measurement of a fuel cell is given by its voltage-current characteristic or polarization curve.[2] When current is drawn from the cell, the actual voltage is decreased from E_{rev} because of irreversible losses. The difference between the E_{rev} and the actual voltage (V) of the fuel cell is indicated by several terms, such as overpotential, overvoltage, polarization, or voltage drop and is usually given by the symbol η.

Even when current is not drawn from the cell, the open circuit voltage (OCV) that can actually be measured at the terminals of a fuel cell is lower than the theoretical value calculated on the basis of thermodynamic data (E_{rev}). In high temperature cells, in which reaction kinetics at the electrodes are fast, deviations from this voltage are attributed to gas leaks across the electrolyte generally due to poor density and/or cracks, or to partial electronic conduction through the electrolyte. In low temperature cells, the slow reaction kinetics at the electrodes may prevent the measurement of the equilibrium potential even under otherwise ideal conditions (no electronic conductivity, no gas cross-over).[2]

When current flows in the external circuit of the cell, several irreversible processes contribute to the whole cell overpotential. The main losses can be classified in: activation, ohmic and mass transport polarizations.[6,8,9]

At low current densities, the shape of the polarization curve is primarily determined by the a*ctivation polarization*. This loss is caused by slow electrode reactions, and thus it represents the most important irreversibility in low temperature fuel cells. At increased fuel cell operating temperatures, activation polarization becomes less significant.[3,9] This type of polarization is mostly due to the cathode electrode because the rate of oxygen reduction at the cathode is orders of magnitude slower than the rate of hydrogen oxidation reaction at the anode. The anode activation polarization becomes important when fuels other than hydrogen are used, e.g. methanol.

Increasing the current density drawn from the cell, the shape of the polarization curve becomes approximately linear, reflecting the effect of *ohmic polarization*. This irreversible loss has no correlation with any chemical process at the electrodes and it represents the voltage drop across the resistive components of the cell. In most fuel cells the ohmic polarization is mainly caused by the electrolyte, though the cell resistance related to interconnectors or bipolar plates can also be important.[9] This kind of polarization can be reduced using highly conductive materials, thin electrolytes, and better performing interconnectors.

When current density is further increased, the polarization curve begins to bend down because of *mass transport or concentration polarization*. This kind of loss comes from a reduction of reactant concentrations at the electrodes. The change in concentration gives rise to a reduction in reactant partial pressure at electrode surfaces, which results in a decreased cell voltage.[6,9] The main source of this polarization is again the cathode, because oxygen diffusivity is significantly lower than that of hydrogen due to the larger oxygen molecule size.

Considering all the irreversible losses, the actual cell potential can be described according to:

$$V = E_{rev} - \eta_L - \eta_A - \eta_{iR} - \eta_C \quad (7)$$

where E_{rev} is the reversible voltage, η_L accounts for the voltage losses due to leaks or partial electronic conduction across the electrolyte, η_A is the activation overpotential due to slow electrode reactions, η_{iR} is the overpotential due to ohmic resistances in the cell, and η_C is the overpotential due to mass diffusion limitations.

Figure 1.3 highlights the impact of all the polarizations on the reversible voltage.

The power density reaches the peak at intermediate voltage, while the efficiency, given by the ratio of the actual voltage (V) and the reversible voltage (E_{rev}), is greatest at low current density.

As estimated by B.C.H. Steele,[10] the combined area-specific resistivity (ASR) of the cell components (electrolyte, anode and cathode) should be below 0.5 Ωcm^2 (and ideally approach 0.1 Ωcm^2) to ensure high power densities, with the targets of 1 $kWdm^{-3}$ or 1 $kWkg^{-1}$ often mentioned for transport applications.

The need to minimize cell resistivity has a major impact on the selection and processing of the cell components. Polarizations can be reduced by optimizing the properties of fuel cell components, such as microstructure, exchange kinetics, charge transport properties, and so on. Thus, the development of better performing materials is the key point to obtain power density suitable for SOFC commercialization.

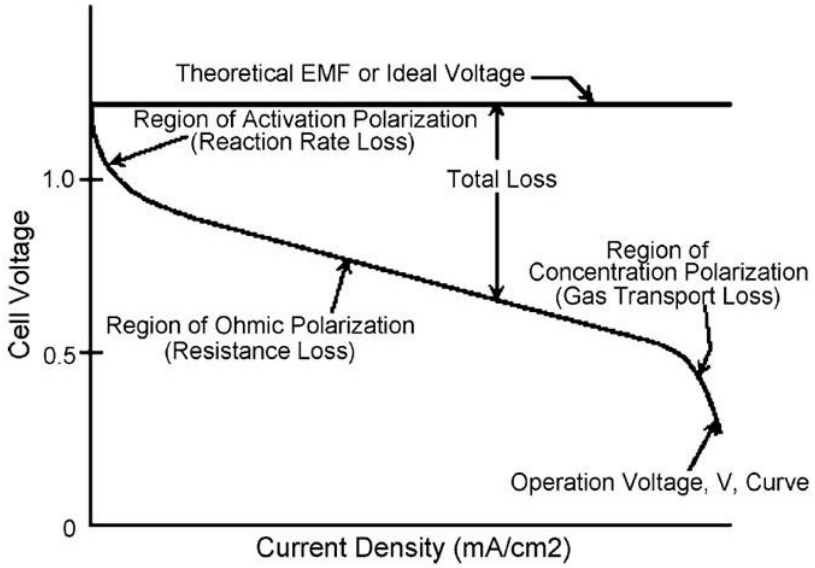

Figure1.3: Ideal and actual fuel cell voltage characteristic.

1.4 SOFC Components

As previously mentioned, the unit block of a SOFC consists of a dense ceramic electrolyte separating two porous electrodes, the cathode on the oxidant side and the anode on the fuel side.

1.4.1 Electrolyte

The electrolyte has a large impact on fuel cell performance through its contribution to the ohmic internal resistance.[1] For optimum cell performance, the electrolyte must have a fully dense structure to maximize its conductivity and minimize reactant cross-over. Furthermore, it should present high ionic conductivity (typically higher than 10^{-3} Scm^{-1}) at the required operating temperature, whereas the electronic conductivity should be negligible.

The ionic conductivity of an electrolyte material depends on the concentration of the ionic charge carriers, and their mobility, via:

$$\sigma = \mathrm{n} * \mathrm{q} * \mu \tag{8}$$

where σ is the ionic conductivity, n is the number of mobile ions in a given volume of lattice, q is the ion electrical charge and μ is the ion mobility. Equation 8 can be also expressed in the form of the Arrhenius relationship:

$$\sigma T = A\exp[-E_a/(kT)] \tag{9}$$

where Ea is the activation energy for ion migration, A is the pre-exponential factor which is a function of concentration and vibrational frequency of the charge carries, and k is the Boltazman constant.

The above equations highlight two primary variables that should be exploited to increase the electrolyte ionic conductivity: the concentration of mobile ions and the activation energy for their migration. In particular the former should be maximized and the latter minimized.

The electrolyte microstructure, i.e. the electrolyte grain size, and the concentration and location of possible impurities can have a significant influence on the total conductivity. In the presence of poor conductive grain boundary, the smaller the grain-boundary volume within the electrolyte, the higher its conductivity. Formation of poorly conducting secondary phases may limit ionic migration through the electrolyte.

Other important characteristics of a good SOFC electrolyte are: sufficient mechanical resistance for long-term operation, good thermal and chemical compatibility with the reactant environment and the contacting materials, a thermal expansion coefficient similar to that of the electrodes and contacting components, cheap and simple forming properties so that thin layers can be easily fabricated.[1,8]

1.4.2 Electrodes

The demands on fuel cell electrodes are perhaps even more extreme than those on the electrolyte. An ideal electrode should be able to transport both gaseous (or liquid) species, ions (electrolyte) and electrons (electrode), and at the points where all three meet, the so-called triple phase boundaries (TPB), the electro-catalysts must be fast.[11] Thus, a good electrode should present continuous channels made of pores to allow rapid transport of reactant gases at the TPB, it should present high electronic conductivity and high catalytic activity toward oxidant reduction (cathode) or fuel oxidation (anode). Furthermore, a suitable electrode material should not exhibit any reaction with neighbouring electrolyte and interconnector. Finally, it should have thermal expansion coefficient close to those of adjacent components.[12]

The electrical impedance of the electrodes is essentially comprised of activation polarization, ohmic resistance, contact resistance, and concentration polarization. Activation polarization is related to the charge transfer processes and depends on TPB and electrocatalytic activity of the electrode itself. If an electrode exhibits exclusively electronic conduction, the effective electrochemical reaction zone (ERZ) is mainly limited to the physical TPB. In contrast, the use of a mixed-conducting electrode is expected to drastically enlarge the ERZ over the entire electrode-gas interfacial area as shown in figure 1.4. Large ERZ zone results in a significant drop in the activation polarization.[13]

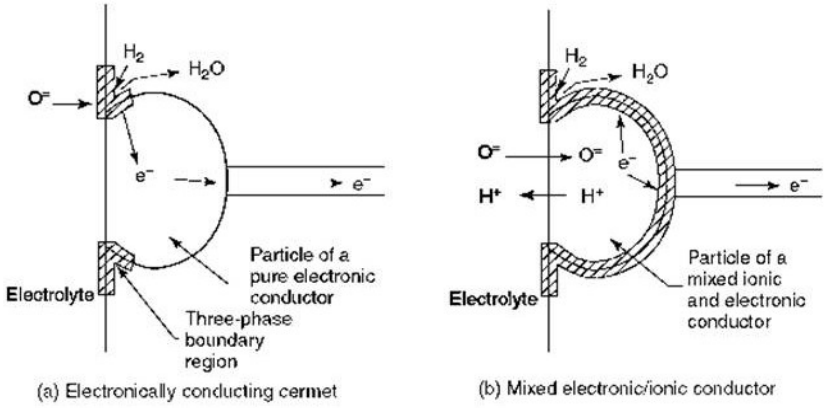

Figure 1.4: Illustration of the TPB regions of different SOFC anode materials. Similar extension of the boundary is obtained in mixed conducting cathode materials. [4]

The ohmic electrode resistance is related to its conduction properties, and therefore, is determined by the magnitude of its electrical resistivity and thickness. The contact resistance derives mainly from poor adherence between electrode and electrolyte. Finally, concentration polarization is related to the transport of gaseous species through the porous electrodes and, thus, its magnitude is dictated by the microstructure of the electrode, e.g. the volume percent porosity, the pore size, and the tortuosity factor.

Regarding the *negative electrode (anode),* it should present high electrocatalytic activity toward oxidation of fuel gases, and preferably good catalytic activity toward hydrocarbon reforming.

Furthermore, the fuel electrode must be stable in reducing environment, should be electronically conducting, and must have sufficient porosity (20–40%) to allow the transport of the reactant and product gases to/away from the electrolyte/anode interface. For application with hydrocarbon fuels, it is also important for the anode to display an excellent carburization resistance.

The use of composite anodes increases the number of sites where the anode reaction can occur, improving the electrode performance.[8] When using an electronic conducting anode, the electrochemical reaction can only occur at the three-phase boundary. In that case, if there is a breakdown in connectivity in any one of the three phases, the anode reaction cannot occur. If ions from the electrolyte cannot reach the reaction site, if gas-phase fuel molecules cannot reach the site, or if electrons cannot be removed, then that site cannot contribute to the performance of the cell.[14] A schematic illustration of the region between the electrolyte and the anode where the TPB exists is shown in figure 1.5.

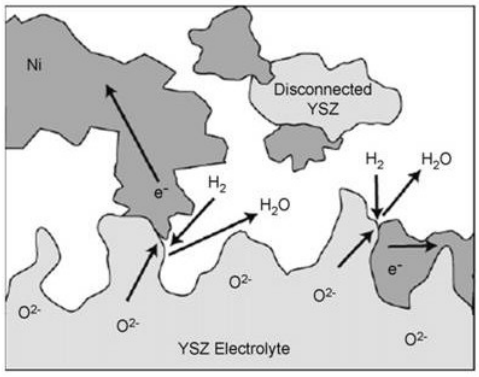

Figure 1.5: Schematic diagram of Ni/YSZ anode three-phase boundary. [14]

The reducing conditions present on the fuel side permit the use of a metal such as nickel (alternately cobalt or ruthenium) as fuel electrode. Nickel is as an excellent electrocatalyst for hydrogen oxidation and provides high electronic conductivity. Ni is also a good reforming catalyst which allows carrying out internal reforming of hydrocarbon fuels directly on the anode.[6,8,9] If methane is used as

fuel, it can be easily converted to hydrogen via internal steam reforming as shown by Equ. 10, or via catalytic partial oxidation as indicated by Equ. 11:

$$CH_4+H_2O\rightarrow CO+3H_2 \quad (10)$$

$$2CH_4+O_2\rightarrow 2CO+4H_2 \quad (11)$$

The gas produced can then be electrochemically oxidized as:

$$H_2+O^{2-}\rightarrow H_2O+2e^- \quad (12)$$

$$CO+O^{2-}\rightarrow CO_2+2e^- \quad (13)$$

Nickel presents good catalytic activity not only for the steam reforming but also for methane cracking (Equ. 14), thus carbon deposition occurs rapidly unless sufficient steam is present.[8] Carbon can be deposited on the anode surface by the Boudouard reaction (Equ. 15).

$$CH_4\rightarrow C+2H_2 \quad (14)$$

$$2CO\rightarrow C+CO_2 \quad (15)$$

Formation of carbon deposits on Ni particles results in high activation polarization, which leads to decreasing cell performance.[13]

The *positive electrode (cathode)* must be porous and electronically conductive as the anode, but it must be electrocatalytic active toward oxidant reduction. In the case of a pure electronic conducting cathode material the reduction of oxygen is generally thought to be confined close to the electrode/electrolyte interface, where the gas has simultaneous access to both the electronically and ionically conducting phase (TPB). Increasing the electrode ionic conductivity, oxygen reduction becomes possible in a wider interface area around the TPB. Using a mixed ionic-electronic conductor (MIEC) cathode, the electrochemical reaction zone is enlarged over the entire cathode-gas interfacial area (see figure 1.6). Extending the active region, oxygen reduction kinetics is improved. In the case of a pure electronic conducting cathode material, the TPB can be increased adding an ionic conducting phase to form a porous composite microstructure.[15]

It is generally admitted that the oxygen reduction reaction can comprise several elemental steps: oxygen diffusion in the gas phase, oxygen dissociative adsorption, oxygen incorporation and oxygen ion diffusion in the cathode bulk (if MIEC cathode), surface transport of O^{2-} at the electrode-electrolyte interface, incorporation of oxygen into the electrolyte via TPB, and oxide ion transfer from the cathode to the electrolyte (if MIEC cathode). Each of these individual reaction steps contribute to the overall electrode polarization.[15]

Although there is agreement about the reaction pathways, there remains uncertainty and disagreement about the nature of the rate-limiting step. For MIEC cathode, in analogy to a porous metal catalyst, many workers apply a traditional paradigm in which O_2 reduction is limited by charge-transfer process occurring locally at the TPB. However, much evidence suggests that oxygen absorption and transport in the bulk of the mixed conductor play a significant (if not dominant) role in determining the electrode polarization.[16]

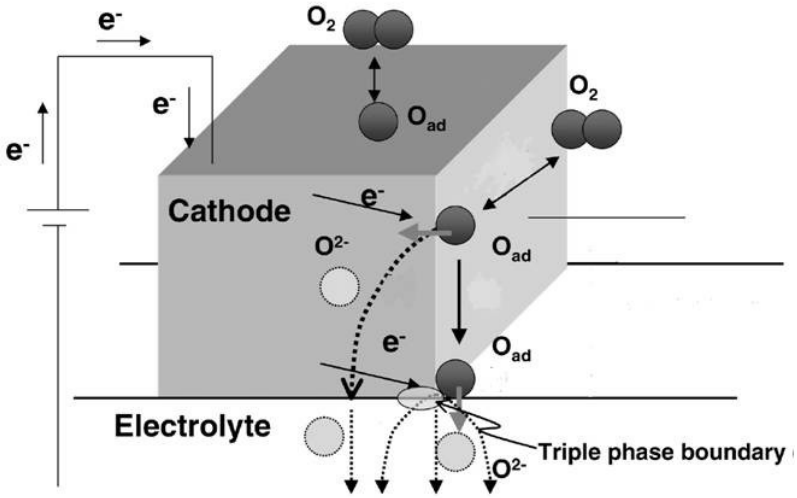

Figure 1.6: elemental step of oxygen reduction for a mixed oxygen-ion/electron conducting cathode. [17]

The most commonly used parameter to determine the rate-limiting step in the cathode reactions is the measurement of the electrode resistance as a function of both temperature and oxygen partial pressure.

It has been observed that gas-phase diffusion inside the electrode pores becomes significant only at low oxygen partial pressure.[18,19]

The dissociative adsorption of oxygen from the surrounding gas phase on the electrode surface is given by the equation:

$$O_2 \leftrightarrow 2O_{ad} \tag{16}$$

It has been shown that surface oxygen vacancies promote dissociative adsorption of oxygen.[20,21] If dissociative adsorption is the rate-limiting step, the electrode resistance has been found proportional to $(P_{O_2})^{-1/2}$.[22]

The oxygen exchange redox reaction which takes place at the triple phase boundary interface, is given by:

$$O_{ad} + V_O^{\bullet\bullet} + 2e^- \leftrightarrow O_O \tag{17}$$

It should be pointed out that in the case of a MIEC cathode the oxygen exchange redox reaction can occur also on the electrode surface between the adsorbed oxygen and the bulk electrode material. This reaction step is expected to vary as the fourth root of the oxygen partial pressure.[23].

For a MIEC cathode, one must consider the process of oxygen transport from the electrode/gas surface to the electrode/electrolyte interface through the bulk electrode material, which occurs by diffusion of oxide vacancies in the mixed conductor. The bulk diffusion resistance is expected to vary inversely with the concentration of oxygen vacancies. When the vacancy concentration is small, the diffusion resistance would be proportional to the square root of the oxygen pressure.[24]

Finally, the transfer of oxide species from the MIEC electrode to the electrolyte across the two-phase boundary is given by:

$$O_{O(electrode)} + V^{\bullet\bullet}_{O(electrolyte)} \leftrightarrow O_{O(electrolyte)} + V^{\bullet\bullet}_{O(electrode)} \qquad (18)$$

1.4.3 Additional Components

Additional components in a complete SOFC power generator system are the *interconnectors or bipolar plates*, which link up individual cells in a stack. In addition to providing electronic conduction pathways, the interconnectors serve to keep oxidant and fuel gases separate from each other. Thus, an ideal interconnector has high electronic conductivity (its resistance contributes to the overall ohmic losses in the stack), excellent impermeability to gases to minimize direct mixing of oxidant and fuel during cell operation, chemical stability under both oxidizing and reducing conditions, and non-reactivity with the other SOFC system components.[8]

In addition to the interconnectors, planar SOFCs require *sealant materials* to isolate anode and cathode chambers.

1.5 Materials for SOFC

Up to now, the most used SOFC electrolyte has been Y_2O_3-stabilized ZrO_2 (YSZ), an oxygen-ion conductor.[3-11] The yttrium oxide dopant serves dual roles: it stabilizes the high temperature zirconia cubic phase and generates oxygen vacancies through the following defect reaction written in the Kroger–Vink notation:

$$Y_2O_3 \rightarrow 2Y_{Zr}^{'} + 3O_O^x + V_O^{\bullet\bullet} \qquad (19)$$

i.e. an oxygen vacancy is created for every mole of the dopant. The conductivity of YSZ at 1000°C is maximum (about 0.1 Scm^{-1}) at about 10 mol.% yttria.[12]

Regarding the anode materials, usually, a cermet of Ni-YSZ is utilized.[3,5-8,11,12] The YSZ phase provides a thermal expansion coefficient closer to that of the electrolyte and allows a better adhesion between the anode and the electrolyte. Furthermore, it constitutes a framework for the dispersion of Ni particles and acts as an inhibitor for Ni powder coarsening during both sintering and cell operation. The additional advantage of using a composite anode is that it can provide a means of extending the anode reaction zone. In the attempt to decrease the resistance at the anode /electrolyte interface, several developers are also investigating bi-layer anodes.[14]

Although Ni-YSZ cermets have been successfully used in SOFCs, there are some challenges remaining. As previously mentioned for pure Ni anode, when carbon-containing fuels are used, the carbon deposition occurring on the electrode surface can block the anode reaction.[8,11] One approach to overcome this limitation is to replace nickel with copper, which does not catalyze C–C bond formation, reducing carbon deposition.[25] Ni-YSZ anodes can also be poisoned by sulphur.

Most of the cathode materials for HT-SOFC are made of electronic conductors, such as Sr doped $LaMnO_3$ (LSM).[3,5-8,12]. The electronic conductivity of lanthanum manganite is due to hopping of an electron hole between the Mn +3 and +4 valence states. This conductivity is enhanced by doping with a divalent ion such as calcium or strontium. The reactivity and interdiffusion studies have proved that interactions between doped lanthanum manganite and yttria stabilized zirconia electrolyte are minimal at 1000°. [8,12] As for the anode, to increase the triple phase boundary density, an ionic conducting phase is usually added to form a composite cathode and multi-layers are also used.[17]

The interconnectors utilized to date are expensive metals or ceramics materials, which represent the main cost penalties in HT-SOFC development. Low cost interconnector materials, such as stainless steel, cannot be used because of their thermal mismatch with the other SOFC components at high temperature and their rapid degradation. Doped $LaCrO_3$ was used by Siemens Westinghouse because of its high electronic conductivity.[3,5,7,12] Its conductivity is enhanced as lower valence ions (e.g. Ca, Mg, Sr, etc.) are substituted on either the La or the Cr sites. However, this material is particularly difficult to process because of chromium oxide evaporation at high temperatures.[3] Moreover, it can also exhibit

structural failure when exposed to the large chemical potential gradients imposed by the cathodic and anodic gaseous environments.[26] Research efforts are mainly focused in reducing SOFC operating temperature, which certainly allow the use of cheaper interconnectors.[5]

For the sealing materials the usual approach is the use of glasses that have a transition temperature close to the operating temperature of SOFC. A particular problem is the migration of silica from such glasses, which can cause cell degradation.[9]

1.6 SOFC Configurations

Several configurations have been investigated for a SOFC unit block. Tubular and planar designs are primary SOFC configurations.[5]

Tubular SOFC was pioneered by the US Westinghouse Electric Corporation (now Siemens Westinghouse Power Corporation or SWPC) in the late 1970s. The original design used a porous calcia-stabilized zirconia support tube, 1 to 2 mm thick, onto which the cylindrical anodes were deposited. By a masking process, the electrolyte, interconnector, and finally the fuel electrode were deposited on top of the anode. The process was reversed in the early 1980s so that the air electrode became the first layer to be deposited on the zirconia tube, and the fuel electrode was on the outside. This configuration became the norm for the next 15 years. The problem with the tubular design has been the low power density and the high fabrication costs.[1] The low power density is a result of the long path for the electrical current through each cell and the large voids within the stack structure, as shown in Figure 1.7. The high costs are due to the expensive methods for the electrolyte and the electrode deposition, i.e. electrochemical vapour deposition (EVD). Most recently, the zirconia support tube has been eliminated from the design and the tubes are now made from air-electrode materials, resulting in an air-electrode-support (AES) onto which the electrolyte is deposited by EVD, followed by plasma spraying of the anode.[5] One great advantage of the tubular design of SOFC is that high-temperature gas-tight seals can be eliminated.

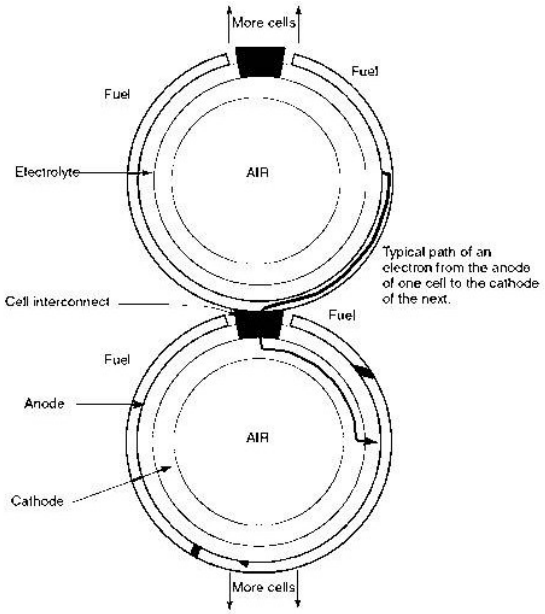

Figure 1.8: Tubular SOFC configuration.

Alternatively to the tubular SOFC, planar configuration and a monolithic design have been developed for many years. This bipolar or flat-plate structure enables a simple electrical connection in series between the cells, without long current path as for the tubular cell. Thus, the bipolar flat-plate design results in lower ohmic losses than in the tubular arrangement. This leads to a superior stack performance and a much higher power density. Another advantage of the planar design is that low-cost fabrication methods, such as screen printing and tape casting can be used. Otherwise, one of the major disadvantages of the planar design is the need for gas-tight sealing around the edge of the cell components.

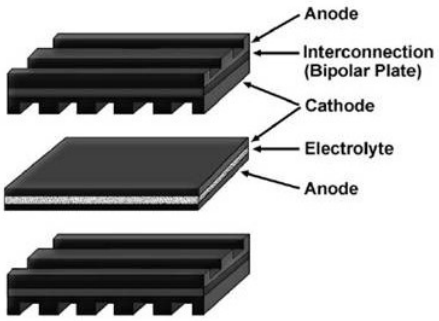

Figure 1.8: Planar SOFC configuration.

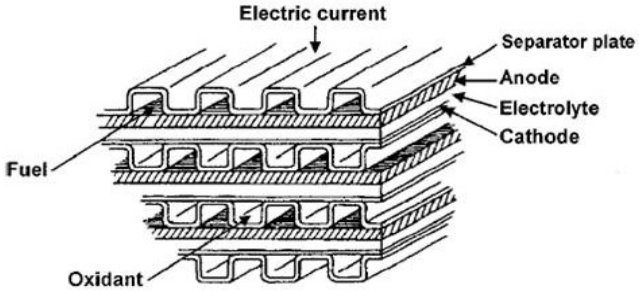

Figure 1.9: Typical planar SOFC stack arrangement.

1.7 Intermediate Temperature (IT) SOFCs

As illustrated in Section 1.2, HT-SOFCs have emerged as a promising energy conversion technology.[5] However, HT-SOFCs are still much too costly for widespread commercialization.[3] Several of the challenges hindering the commercialization of SOFC technology are the consequence of the high temperatures required for their operation. High operating temperatures preclude the use of cheap interconnectors, such as stainless steel, because of degradation and thermal mismatch with the other components. Thermal stress caused by the high operating temperature can induce system degradation and failure at glass seal.[3]

Lowering SOFC operating temperature can reduce fabrication costs, simplifies the thermal management, aids in faster start up and cool down procedures, and diminishes the power consumption for reaching the operating temperature. Furthermore, it results in less degradation of the cell and stack components, increasing the cell life time.[5,7]

New SOFC possible applications can be opened lowering their operation temperature. While HT-SOFCs dominate the applications in the kW to MW power range, using combined cycle technology, SOFCs working at relative low temperatures can be also particularly suitable to supply power in the range of ~1 kW to a few ten kW for distributed units. The development of smaller intermediate temperature stacks for distributed units is being stimulated by electrical supply liberalization policies.[26] Achieving a faster start-up and shut-down time make SOFCs a viable technology also for mobile applications, as auxiliary power units or traction power in vehicles, sometimes hybridized with battery technology.[1]

In recognition of all mentioned advantages in lowering the operating temperature, many efforts have been oriented to develop SOFC working at intermediate temperature (IT) 400–700 °C.

In the attempt to reduce the operating temperature, the increasing electrolyte resistivity is one of the problems to overcome. In fact, the ion transport mechanism in ceramic electrolytes is a thermally activated process. The electrolyte resistance can be lowered either by decreasing the electrolyte thickness or with alternative materials of high electrical conductivity in the IT range.

B.C.H. Steele [10,26,27] used the following approach to determine the trade-off between electrolyte conductivity and thickness in order to give a suitable power density (with respect to cell area). It is assumed that adequate fuel cell performance is obtained when the electrolyte area specific resistance (ASR) is less than 0.15 Ωcm^2. If an electrolyte is produced with a thickness of 15μm, it follows that the specific ionic conductivity required to achieve the target ASR (σ=thickness/ASR) should be higher than 10^{-2} Scm^{-1}.

The reduction of SOFC operating temperature also causes large overpotential at the electrode/electrolyte interface. In particular, the cathode plays a critical role in establishing intermediate temperature because the oxygen reduction kinetics are several orders of magnitude slower than the

kinetics related to the fuel oxidation.[17,28,29] One way to reduce cathode overpotential is to realize composite electrodes. It is believed that the observed improved performance is due to the increased triple phase boundary (TPB) density.

A general classification of IT-SOFCs can be based on the charge conduction mechanism of the electrolyte: IT- SOFCs based on oxygen-ion conductor electrolyte and IT- SOFCs based on proton conductor electrolyte.

1.7.1 IT-SOFC based on Oxygen-Ion Conductor Electrolyte

Yttria stabilized zirconia (YSZ), which has been extensively used as electrolyte material for SOFCs operating at high temperatures, becomes a poor oxygen-ion conductor on reducing the operating temperatures to 400-700°C (IT). Scandia doped zirconia shows higher conductivity than YSZ, but it has not been used as electrolyte material because of its instability and also because of the high cost of scandia.[30]

Highly oxygen-ion conductive electrolytes at intermediate temperature are doped ceria, doped bismuth oxide and doped lanthanum gallate.[3,8,10,30] Since all these electrolytes are oxygen-ion conductors, the electrochemical reactions that take place at the electrode/electrolyte interfaces are the same as those described in Chapter 1.2 for HT-SOFCs.

The ionic conductivity of doped ceria is approximately one order of magnitude greater than that of stabilized zirconia for comparable doping conditions. This is a result of the larger ionic radius of Ce^{4+} (0.087 nm in 6-fold coordination) than Zr^{4+}(0.072 nm), which produces a more open structure through which oxygen ions can easily migrate. The maximum ionic conductivity occurs at 10–20 mol% for most of the dopants. It is generally found, and it is the case for ceria based electrolytes, that the highest oxygen ion conductivity is observed when the aliovalent doping cation radius is closest to the ionic radius of the host cation. For this reason, gadolinium doped ceria (CGO) is the most performing and extensively studied ceria based electrolyte. Despite its good oxygen-ion conductivity, ceria exhibits also electronic conductivity since Ce^{4+} can be partially reduced to Ce^{3+} under the reducing conditions prevailing in the anode compartment above 800 K. [1,3,10,30]

Lanthanum gallate is a perovskite oxide that doped with divalent ions, typically Sr and Mg onto the La and Ga sites, respectively, achieves high mobile oxygen vacancies concentration and thus high electrical conductivity. Moreover, its conductivity is entirely ionic over a wide range of oxygen partial pressure. One problem regarding lanthanum gallate electrolyte is that it suffers from reactivity with nickel, which is the most typical SOFC anode.[3,10,30]

Finally, Bi_2O_3 based oxides are particularly interesting among the oxygen ion-conducting materials due to their high ionic conductivity with respect to other solid electrolytes. The fast ionic transport is characteristic of the stabilized δ-Bi_2O_3 phase, which has a fluorite-type structure with high

oxygen vacancy concentration, and the γ-$Bi_4V_2O_{11}$ phase (parent of the so-called BIMEVOX materials). Unfortunately, Bi_2O_3-based materials possess a number of disadvantages, including thermodynamic instability in reducing atmospheres, volatilization of bismuth oxide at moderate temperatures, high corrosion activity and low mechanical strength. Hence, the applicability of these oxides in electrochemical cells is considerably limited.[30] The stabilization of the high-diffusivity δ-Bi_2O_3 phase down to temperatures significantly lower than the α→δ transition temperature (978–1013 K) can be achieved by the substitution of bismuth with rare-earth dopants (such as Y, Dy or Er) and their combinations with higher valence cations, such as W or Nb .[3,30,31]

Assuming that the electrolyte component should not contribute more than 0.15 Ωcm^2 to the total cell ASR,[10,26,27] for a film of 15 μm thickness, the associated electrolyte ionic conductivity value should exceed 10^{-2} Scm^{-1}. Examination of figure 1.10 indicates that the ionic conductivity of $(ZrO_2)_{0.9}(Y_2O_3)_{0.1}$ (YSZ) attains this target value around 700 °C, for $Ce_{0.9}Gd_{0.1}O_{1.95}$ and $La_{0.9}Sr_{0.1}Ga_{0.8}Mg_{0.2}O_{2.85}$ the relevant temperature is 500-550° C. However, note that these are representative values of conductivity for each electrolyte, and actual values will depend on the microstructure, exact level of doping, fabrication and sintering processes. The highest values of electrical conductivity in figure 1.10 are achieved by $Bi_2V_{0.9}Cu_{0.1}O_{5.35}$. Unfortunately, the high instability of this electrolyte in the anode reducing environment makes it not suitable for practical application.

Figure 1.10 highlights also that using an electrolyte supported cell, calling for a thickness of at least 150 μm, all the above mentioned electrolytes would require higher operating temperature to reach the conductivity values equal to 10^{-2} Scm^{-1}. Otherwise, the use of thinner electrolyte films than 15 μm would allow the operating temperature to be lowered.

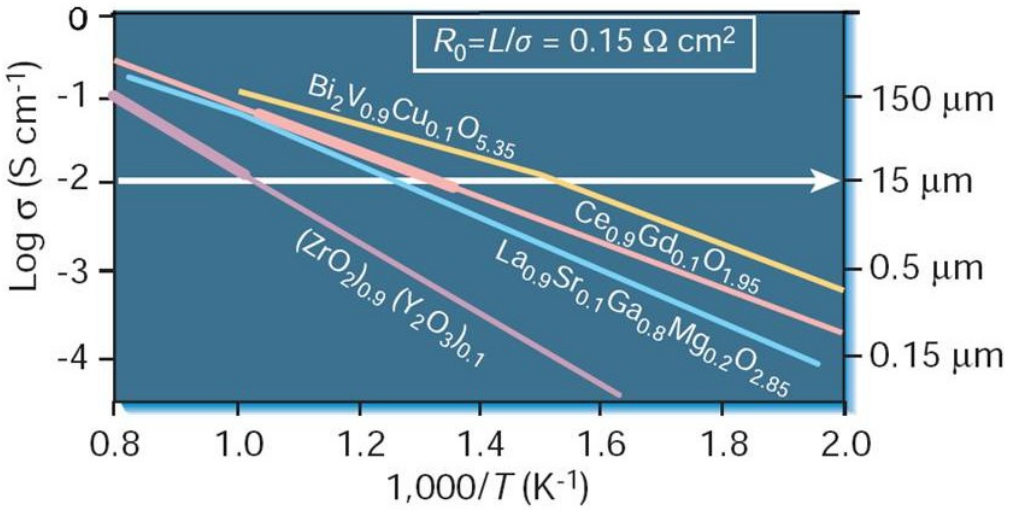

Figure 1.10: Specific conductivity versus reciprocal temperature for selected solid-oxide electrolytes. [10]

The choice of anode materials for an IT-SOFC using an oxygen-ion conducting electrolyte is usually based on Ni-doped ceria cermet.[13] As for the HT-SOFC, nickel is chosen because of its high electronic conductivity and high catalytic activity towards hydrogen oxidation. The use of doped ceria as the oxygen-ion-conducting phase reduces the thermal expansion mismatch between the anode and the electrolyte and also results in lowering the charge-transfer polarization, increasing the triple phase boundary.[27] Using Ni-doped ceria cermet as anode and working with hydrocarbon fuels, the reduction of the operating temperature does not eliminate the problem of carbon deposition on Ni. This can only be avoided by improving the present anode materials. For example, McIntosh et al. [32] replaced Ni cermets with composites containing Cu and ceria or samaria-doped ceria. It has been suggested that Cu is not catalytically active for carbon deposition but it is an efficient current collector.[33,34]

Regarding cathode materials, lanthanum strontium manganite (LSM), which is known as the most promising cathode material for HT-SOFC, presents high polarization when temperature is lowered below 800°C. The medium temperature performance can be enhanced when a second ionically conducting phase, such as doped ZrO_2 or CeO_2, is added to LSM due to the extending TPB. For several characteristics, also $La_{1-x}Sr_xCo_{1-y}Fe_yO_{3-\delta}$ (LSCF) perovskite material has attracted much interest for application in IT-SOFC based on oxygen-ion conducting electrolytes. Primarily, LSCF is not only a good electronic conductor, but it shows also relatively high ion conductivity, which allow the extension of the cathode reaction zone and promotes fast oxygen surface exchange.[35,36] Moreover LSCF presents a good thermal and chemical compatibility with the most performing IT oxygen-ion electrolytes.[36] To increase the triple phase boundary and thus reduce cathode polarization, LSCF has been often mixed with an oxygen-ion conducting phase, such as doped CeO_2, to form composite cathodes.[35-40] Recently, $Ba_{1-x}Sr_xCo_{1-y}Fe_yO_{3-\delta}$ (BSCF) perovskite oxide has been proposed as an alternative cathode material for IT-SOFC application.[41] BSCF presents good cathode performance as result of the high rate of oxygen diffusion through the material.

1.7.2 IT-SOFC based on Proton Conductor Electrolyte

A different approach for reducing SOFC operating temperature is the use of high temperature protonic conductors (HTPCs) as electrolyte material. In the recent years, HTPCs have been widely investigated for application in IT-SOFC because they present some advantages compared to an oxygen-ion conductor electrolyte. The main benefit of the HTPCs is that they can achieve high proton conductivity also at rather low temperatures (350-600 °C) because of the low activation energy for proton conduction (0.3-0.6 eV).[42-44] Furthermore, when hydrogen is used as fuel, a proton conductor electrolyte offers the benefits of generating water at the cathode, and thus the fuel does not become

diluted during cell operation. Consequently, as long as oxygen is plentiful, cell voltage remains high and the efficiency does not become reduced.[3,45]

One important purpose of developing fuel cells is the exploitation and utilization of natural gas as the energy source. When, for example, methane is used as fuel in an oxygen-ion-conducting electrolyte fuel cell, the product of the electrochemical reaction is CO_2 and H_2O (Equs. 10-11) on the anode side. Otherwise, for fuel cells with a proton conducting electrolyte, methane can, in principle, undergo a dehydrogenation reaction to produce other high-molecular hydrocarbons, which are excellent industrial feedstock, without CO_2 generation.[46-48]

$$2CH_4 \rightarrow C_2H_4 + 2H_2 \quad (19)$$

$$2CH_4 \rightarrow C_2H_6 + H_2 \quad (20)$$

Therefore, a proton conductor electrolyte should be able to operate both as membrane for the dehydrogenation reaction and as electrolyte in a fuel cell. This actually represents a cogeneration system, where hydrocarbons are directly used as fuel to produce electricity as well as chemical products through the process of the dehydrogenation reaction.[45] In light of this advantage, the use of a proton conductor electrolyte opens the possibility to realize innovative cells such as methane-coupling SOFC, H_2S-fueled SOFC for desulfurization, zero emission methane SOFC, etc.,. The working principles of such systems are illustrated figure 1.11.[45]

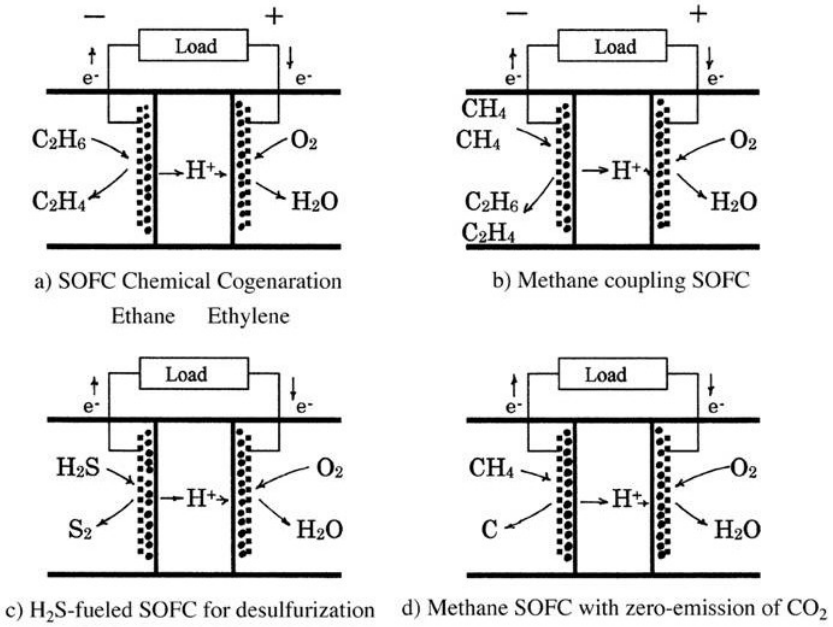

Figure 1.11: Novel SOFCs using proton-conducting ceramics: (a) Ethane SOFC for chemical cogeneration ethylene: (b) methane-coupling SOFC for producing C_2-compounds; (c) H_2S-fueled SOFC for desulfurization; (d) methane SOFC with zero emission of CO_2.[45]

HTPCs show proton conductivity when exposed to hydrogen and/or water vapour containing atmospheres. The identified compounds are oxides with perovskite-related structure ABO_3. They have in the A site an alkaline earth element, such as Ba, Sr, and Ca, while the B site is occupied by a rare earth element, usually Ce and Zr. To promote protonic conductivity, it is paramount to dope the B-site with suitable trivalent elements, such as Y, Nd, Sm, Yb, In, Eu, Gd, etc. Doping with a trivalent elements leads to the formation of oxygen ion vacancies, which play an important role in the production of mobile protons.[49] Protons incorporated in the HTPC structure are generally not bound to any particular oxygen ion, but are instead free to migrate from one ion to the next. This easy migration results in high proton conductivity at rather low temperatures.[3]

Among the HTPCs, doped barium cerate and doped barium zirconate have been widely investigated as electrolyte materials. However, none of these compounds concurrently satisfies two of the essential requirements for IT-SOFC application: high proton conductivity and good chemical stability under fuel cell operating environment. Yttrium-doped barium cerate (BCY) shows the best performance in terms of proton conductivity (about 10^{-2} Scm^{-1} at 600°C), but it reacts with acidic gases (e.g., CO_2, SO_2) and steam.[50] Therefore, the reactivity of BCY is an important drawback that makes it not suitable as electrolyte material for fuel cell applications. On the other hand, yttrium-doped barium zirconate (BZY) has a good chemical stability under CO_2 and water containing atmosphere. However, the poor sinterability of barium zirconates leads to the presence of a large, poor conductive grain boundary surface, resulting in quite low electrical conductivity (about 10^{-3} Scm^{-1} at 600°C).[51] Moreover, due to its high refractory nature the processing of dense electrolyte membranes from $BaZrO_3$-based materials, remains a significant challenge.[42] The very high sintering temperature (around 1700°C) required for its densification can favour chemical reactions at electrode interfaces and makes it impossible to retain electrode porous microstructure.[52]

The highly refractory nature of $BaZrO_3$-based materials has delayed the discovery of their high bulk conductivity, claimed firstly by Kreuer.[44,53] Measuring the conductivity of a sintered pellet, the presence of high grain-boundary impedances may hide the bulk arc either because of the limited frequency range or because of poor resolution between bulk and grain boundary. Kreuer has shown that single crystal zirconates are needed to measure the bulk conductivity,[53] which even exceeds the conductivity of the best oxide ion conductors at temperatures below 700°C.[44] Since doped $BaZrO_3$ has been recognized as one of the most promising proton conducting solid electrolyte, at least for its bulk properties, growing interest has been oriented toward this material. In fact, the possibility of overcoming its low sinterability and high grain boundary resistance may lead to the development of an excellent electrolyte for intermediate temperature fuel cells.

Up to now, several approaches to develop a suitable proton conducting material have been reported in literature. Interesting new stable compounds have been recently investigated, even though their proton conductivity is still inferior to that of the perovskite oxides.[54,55] Another approach reported in the literature is the investigation of solid solutions between cerate and zirconate, which

might couple the good characteristics of the two materials minimizing the side effects.[43,50,51,56-59] Some work has been oriented toward the overcoming of doped $BaZrO_3$ poor sinterability by adding sintering aid such as ZnO [52,60] or by processing using wet chemical route.[61] However, up to now, lower conductivity values (compared to pure BCY) are the price to be paid for chemical stability. Therefore, research aimed at the identification of a highly conductive and chemically stable proton conductor electrolyte is very active at present.

Regarding electrode materials, while there is a large literature on electrodes for application with oxygen-ion conducting electrolytes, scarce fundamental studies on cathode transport behaviour, as well as microstructure investigation have been carried out for cathodes working on IT-SOFCs based on a proton conductor electrolyte.

Platinum has been extensively used for fuel cell experiments. However, besides the elevated cost, Uchida et al.[62] have pointed out that the overpotential of Pt cathode in a proton conductor fuel cell could not be negligible below 900°C

Recently, anode of NiO mixed with a proton conductor phase has been used to take advantage of the enhanced triple phase boundary of composite electrodes.[63-65] Even hydrogen-permeable membranes made of Pd or Pd_xAg_{1-x} have been used in anode supported fuel cell.[66,67]

In the attempt to lower the operating temperature, cathode overpotential represents the main challenges for fuel cell application. As previously reported, good results have been obtained using MIEC cathode for oxygen-ion conductor electrolytes. The same MIEC cathodes, generally cobalto-ferrites, have been used as cathode materials for application in proton conductor fuel cells.[68-73] However, in this case, the overall fuel cell performances were mainly lowered by cathode overpotential. Therefore, it is evident how the development of a superior cathode material is demanded if IT-SOFCs based on proton conductors are to compete with the more established SOFCs using an oxygen-ion conductor electrolyte.

1.8 SOFC Ceramic Processing

SOFCs use a ceramic electrolyte. Because of the high cost of precious metals, generally also the electrodes are fabricated with ceramic materials. The microstructural characteristics of a ceramic material can strongly influenced its electrical behaviour. Microstructural parameters depend on the powder processing, fabrication and sintering conditions employed to produce the ceramics.

A brief description of the most common ceramic synthesis and deposition procedures follows.

1.8.1 Ceramic Powder Processing

Several synthesis procedures are available for the production of ceramic powders. A brief description of the most common synthetic methods is given below.

Solid State process is a conventional ceramic processing involves calcining mixtures of the respective oxides, nitrates or carbonates at high temperatures (1300-1600 °C).[74] Solid state reaction is a diffusion controlled process which requires intimate contact and uniform distribution of reactant species to obtain a single phase and uniform product, so long mixing is necessary.[75] The high temperature calcination process generally results in large particle size of the final product.

Sol gel is an attractive synthetic technique due to its potential for producing high-purity nanocrystalline powders with excellent compositional homogeneity. It is a wet chemical procedure, generally based on hydrolysis and condensation reaction of metal alkoxides. Calcination of the resulting gel produces powders with good compositional homogeneity and high purity. Among the numerous modifications of the basic sol-gel processes, much attention has been focused on the so-called Pechini process in which the desired metal cations are solvated in a solution using a chelating agent, such as citric acid or ethylene diamine tetracetic acid (EDTA). A polyhydroxy alcohol, such as ethylene glycol, is then added to the solution to promote esterification reaction. Metal ions are chelated by the carboxyl groups and remain homogeneously distributed in the polymeric network.[76] Further heating of the solution leads to gelation.

Homogeneous Oxalate Coprecipitation is a synthetic procedure in which ammonium oxalate is added to the oxide or nitrate solution to cause precipitation of the powder. The oxalate is highly reactive and thus shortens the reaction time as well as the particle size.[77] The process imparts good homogeneity and the reactions proceed rapidly at low temperatures.

Glycine Nitrate Process allows the fabrication of high-purity nanocrystalline powders with excellent compositional homogeneity. Glycine is used as a fuel that can burn the metal nitrates. A small amount of heat is required to ignite the mass where the fuel and the oxidizer are intimately mixed. However, lab scale reactions actually do not proceed perfectly and result in multi-phase product.[78]

1.8.2 Ceramic Film Deposition

The use of a thin electrolyte reduces the ohmic polarization of the cell, resulting in higher power density output. For this reason great efforts have been devoted on the development of an economically and technically competitive method for thin film electrolyte deposition. Also the desired quality of the resulting films leads to the choice of the processing procedure.[78]

Ceramic layer fabrication methods can be classified in chemical, physical and ceramic powder processing.

- *Chemical methods*

Chemical methods include a large variety of thin electrolyte deposition techniques, such as chemical vapour deposition (CVD), liquid precursor route and spray pyrolysis.

CVD is a chemical process in which one or more gaseous species are adsorbed on a substrate surface where a chemical reaction with oxygen leads to a dense thin film. The deposition rate is typically 1-10 μm h^{-1}, depending on the evaporation rate and substrate temperature. CVD allows the fabrication of uniform, pure, reproducible films, and to deposit in sites difficult to reach by other deposition techniques.[79] A modified CVD process is the electrochemical vapour deposition (EVD), which is usually used to fabricate dense thin film on porous substrates. The first step of EVD procedure involves the substrate pore closure by a normal CVD reaction. Once the pores are closed, oxygen ions diffuse through the film due to the presence of a large electrochemical potential gradient, and finally reach the metal vapour on the opposite side reacting to form the metal oxide product.

Liquid precursor route is a deposition technique in which a suspension, prepared by dispersing the powder in a solution, is deposited on a substrate and sintered to burn off the organics and get a dense film. This deposition method allows the fabrication of thin, dense and well defined film with controlled purity and homogeneity. The desired microstructure is determined by the precursor reactivity and the deposition conditions.[80] The substrate can be coated either by spin- or dip-coating techniques.[81] The film and substrate material must be chemically compatible and there should be no thermal expansion mismatch between the layers to obtain a crack free deposition.

Spray pyrolysis is a chemical method in which a metal salt solution is sprayed onto a hot substrate to obtain the corresponding metal oxide film. Spray droplets reaching the hot substrate surface undergo pyrolytic (endothermic) decomposition. Three different atomizers can be used for the generation of the spray: blast atomizer (using a stream of gas at high velocity), ultrasonic atomizer (using an ultrasonic irradiation), and, electrostatic atomizer (using high voltage). The atomization technique determines droplet size distribution, efficiency and spray angle. The usual deposition rates are 1-5 μm h^{-1}.[79]

- *Physical methods*

The most common physical methods for ceramic layer processing are the thermal spray technique, the laser deposition technique and physical vapour deposition (PVD) technique.

Thermal spray is a generic term for a process in which the depositing material is heated in a gaseous medium and sprayed at high velocity onto a surface. These processes are less applicable to produce thin electrolytes, but they may be also useful for deposition of porous electrodes.[82] The various techniques derived from the thermal spray process have in common the high temperatures involved, the rapid quenching of the ceramic particles on the cold substrate, and the thermal treatment required to improve the film density.[79]

Laser deposition has become a new and important technique for depositing thin film of a variety of materials.[75] The ability to deposit almost any material preserving its stoichiometry has been recognized and finally renewed the interest in this technology. In the pulsed laser deposition (PLD) the laser pulse passes through a window and impinges on the target material which is vaporized and deposited on the substrate in the form of a thin film. The process involves a large number of variables such as wavelength, power density, background gas, pressure, target composition, substrate-target distance, and substrate temperature. PLD requires temperatures around 500-700°C to deposit high-quality crystalline films. It is relatively easy to produce multilayers by substitution of targets into the path of the laser beam.

Physical vapour deposition (PVD) is a generic term for a variety of sputtering techniques such as Radio frequency (RF) sputtering or Reactive DC current magnetron sputtering. The RF sputtering has been widely used for YSZ film deposition.[83] This technique allows the use of various substrate materials, which are generally unheated. RF sputtering deposition rates are generally low (0.25 μm h^{-1}), while reactive magnetron sputtering allows much higher deposition rates (2.5 μm h^{-1}) because of the higher sputtering yield.[79]

- *Ceramic powder processing methods*

Ceramic powder processing methods can be used for deposition of both dense and porous ceramic layers. Tape casting, screen printing, tape calendaring, and electrophoretic deposition have been extensively used for preparing dense electrolyte or porous electrodes of a few tens of microns to 200 μm thickness.[79]

Tape Casting is a suitable technique to produce green tape of different shapes from ceramic powders. Casting is performed by applying highly viscous slurry consisting of a mixture of ceramic powder, organic binder and plasticizer with a movable doctor blade on a removable support. Multi-layer tapes can be fabricated by subsequently casting several layers on top of each other. However, the co-firing of different materials requires the total matching of shrinkage rate throughout the whole binder burn-out and sintering temperature regime. Tape Calendaring is a similar technique to form tape

of controlled size in which the slurry is casting between two-roll mills. The tape thickness is controlled by the spacing of the rolls.

Screen printing is used to produce porous or dense layers with thickness from a few microns to 100 microns. Slurry similar to that prepared for the tape casting is forced through the open meshes of a screen using a squeegee. Good attachment of the layer to the substrate can be achieve by careful control of the powder characteristic and sintering conditions.[79]

Electrophoretic deposition involves the deposition of charge powder particles from a suspension onto a metallic electrode or a conductive substrate by application of an electric field. This technique has the advantages of short operation time and little restriction on the shape of the substrate.

1.9 References

1. D.J.L. Brett, A. Atkinson, N.P. Brandon, S.J. Skinner, *Chem. Soc. Rev*., 37 (2008) 1568.
2. S. Cleghon, J. Kolde, W. Liu, *Handbook of Fuel Cells-Fundamentals, Technology and Application,* J. Wiley and Sons, Ltd, Chichester (2003).
3. S.M. Haile, *Acta Materialia,* 51 (2003) 5981.
4. K. Kordesch, G. Simader, *Fuel Cells and Their Applications*, VHC, Weinheim 1996A.B.
5. A.B. Stambouli, E. Traversa, *Renewable and Sustainable Energy Reviews*, 6 (2002) 433.
6. S. Kakac, A. Pramuanjaroenkij, X.Y. Zhou, *International Journal of Hydrogen Energy*, 32 (2007) 761.
7. S.C. Singhal, *Solid State Ionics*, 152-153 (2002) 405.
8. S.C. Singhal, K. Kendall, *High-temperature Solid Oxide Fuel Cells: Fundamentals, Design and Applications*, Elsevier 2003.
9. J. Larminie, A. Dicks, *Fuel Cell Systems Explained*, John Wiley & Sons Ltd, Second edition 2003.
10. B.C.H. Steele, A. Heinzel, *Nature*, 414 (2001) 345.
11. J.W. Fergus, *Solid State Ionics*, 177 (2006) 1529.
12. S.C. Singhal, *Solid State Ionics*, 135 (2000) 305.
13. W.Z. Zhu, S.C. Deevi, *Materials Science and Engineering*, A362 (2003) 228.
14. C. Sun, U. Stimming, *J. of Power Sources*, 171 (2007) 247.
15. S.B. Adler, *Chem. Rev*., 104 (2004) 4791.
16. S.B. Adler, *Solid State Ionics*, 111 (1998) 124.
17. T. Horita, K. Yamaji, N. Sakai, Y. Xiong., T. Kato, H. Yokokawa, T. Kawada, *J. of Power Sources*, 106 (2002) 224.
18. S.B. Adler, J.A. Lane, B.C.H. Steele, *J. Electrochem. Soc*,. 143(1996) 3554.
19. S.B. Adler, J.A. Lane, B.C.H. Steele, J. *Electrochem. Soc*., 144(1997)1884.
20. V.E. Henrich, P.A. Cox, *Appl. Surf. Sci.*, 72 (1993) 277.
21. J.A. Kilner, R.A. De Souza, I.C. Fullarton, *Solid State Ionics*, 86–88 (1996) 703.
22. H. Fukunaga, M. Koyama, N. Takahashi, C. Wen, K. Yamada, *Solid State Ionics*, 132 (2000) 279.
23. Y. Takeda, R. Kanno, M. Noda, Y. Tomida, O. Yamamoto, *J. Electrochem. Soc*.,134 (1987) 2656.
24. A. Ringuede´, J. Fouletierr, *Solid State Ionics*, 139 (2001) 167.
25. S. Tao, J.T.S. Irvine, *Chem. Rec.*, 4 (2004) 83.
26. B.C.H. Steele, *J. of Materials Science*, 36 (2001) 1053.
27. B. C. H. Steele, *Solid State Ionics*, 129 (2000) 95.
28. M. Camaratta, E. D. Wachsman, *J. Electrochem. Soc.*, 155 (2) (2008) B135.

29. H. Yamaura, T. Ikuta, H. Yahiro, G. Okada, *Solid State Ionics*, 176 (2005) 269.
30. O. Yamamoto, *Electrochim. Acta*, 45 (2000) 2423.
31. V.V. Khartona, F.M.B. Marquesa, A. Atkinson, *Solid State Ionics*, 174 (2004) 135.
32. S. McIntosh, J.M. Vohs, R.J. Gorte, *J. Electrochem. Soc.*, 150 (2003) A470.
33. S. Park, J.M. Vohs, R.J. Gorte, *Nature*, 404 (2000) 265.
34. C. Lu, W.L. Worrell, R.J. Gorte, J.M. Vohs, *J. Electrochem. Soc*., 150 (2003) A354.
35. E. Perry Murray, M.J. Sever, S.A. Barnett, *Solid State Ionics*, 148, (2002) 27.
36. A. Esquirol, J. Kilner, N. Brandon, *Solid State Ionics*, 175 (2004) 63.
37. V. Dusastre, J.A. Kilner, *Solid State Ionics*, 126 (1999)163.
38. B.C.H. Steele, K.M. Hori, S. Uchino, *Solid State Ionics*, 135 (2000) 445.
39. H.J. Hwang, J.W. Moon, S. Lee, E.A. Lee, *J. of Power Sources*, 145 (2005) 243.
40. C. Fu, K. Sun, N. Zhang, X. Chen, D. Zhou, *Electrochimica Acta*, 52 (2007) 4589.
41. Z. Shao, S.M. Haile, *Nature*, 431 (2004) 170.
42. H.G. Bohn, T. Schober, *J. Am. Ceram. Soc*., 83 (2000) 768.
43. K. Katahira, Y. Kohchi, T. Shimura, H. Iwahara, *Solid State Ionics*, 138 (2000) 91.
44. K.D. Kreuer, St. Adams, W. Munch, A. Fuchs, U. Klock, J. Maier, *Solid State Ionics*, 145 (2001) 295.
45. H. Iwahara, Y. Asakura, K. Katahira, M. Tanaka, *Solid State Ionics*, 168 (2004) 299.
46. B. Zhu, I. Albinsson, B.E. Mellander, G. Meng, *Solid State Ionics*, 125 (1999) 439.
47. S. Hamakawa, T. Hibino, and H. Iwahara, *J. Electrochem. Soc.*, 140 (2) (1993) 459.
48. S. Hamakawa, T. Hibino, and H. Iwahara, *J. Electrochem. Soc*., 141 (7) (1994) 1720.
49. H Iwahara, *Solid state Ionics*, 86-88 (1996) 9.
50. S.M. Haile, G. Staneff, K.H. Ryu, *J. Mater. Sci*., 146 (1999) 2038.
51. K.H Ryu, S.M. Haile, *Solid State Ionics*, 125 (1999) 355.
52. S.Tao, J.T.S. Irvine, *J. Of Solid State Chemistry*, 180 (2007) 3493.
53. K.D Kreuer. *Solid State Ionics*, 25 (1999) 285.
54. R. Haugsrud, Y. Larring, T. Norby, *Solid State Ionics*, 176 (2005) 2957.
55. K. Amezawa, Y. Kitajima, Y. Tomii, N. Yamamoto, M. Widerøe, T. Norby, *Solid State Ionics*, 176 (2005) 2867.
56. X. Ma, J. Dai, H. Zhang, D.E. Reisner, *Surface and Coatings Technology* ,200 (2005) 1252.
57. T. Shimada , C. Wen, N. Taniguchi , J. Otomo, H. Takahashi, *J. Power Sources*, 131 (2004) 289.
58. C. Zuo, S. Zha, M. Liu, M. Hatano, M. Uchiyama, *Adv. Mater*. 18 (2006) 3318.
59. A.K. Azad, J.T.S. Irvine, *Solid State Ionics*, 178 (2007) 635.
60. P.Babilo, S.M. Haile, J. *Am.Ceram. Soc.*, 88 (2005) 2362.
61. A. Magrez, T. Schober, *Solid State Ionics*, 174 (2004) 588[A]
62. H. Uchida, S. Tanaka, H. Iwahara, *J. Of Appl. Electrochem*., 5 (1985) 93.

63. N. Maffei, L. Pelletier, A. McFarlan, *Journal of Power Sources*, 136 (2004) 24.
64. P. Ranran, W. Yan, Y. Lizhai, M. Zongqiang, *Solid State Ionics*, 177 (2006) 389.
65. G. Meng, P. Wang, Y. Gu, D. Peng, *Solid State Ionics*, 136–137 (2000) 209.
66. S. Yamaguchi, S. Yamamoto, T. Shishido, M. Omori, A. Okubo, *J. of Power Sources*, 129 (2004) 4.
67. N. Ito, M. Iijima, K. Kimura, S. Iguchi, *J. of Power Sources*, 152 (2005) 200.
68. H. Yamaura, T. Ikuta, H. Yahiro, G. Okada, *Solid State Ionics*, 176 (2005) 269.
69. E. Boehm, A.J. McEvoy, *Fuel Cell*, 1 (2006) 54.
70. H. Iwahara, T. Yajima, T. Hibino, H. Ushida *J. Electrochem. Soc*, 140 (6) (1993) 1687.
71. T. Hibino, A. Hashimoto, M. Suzuki, M. Sano, *J. Electrochem. Soc*, 149 (11) (2002) A1503.
72. P. Ranran, W. Yan, Y. Lizhai, M. Zongqiang, *Solid State Ionics*, 177 (2006) 389.
73. J.R. Tolchard, T. Grande, *Solid State Ionics*, 178 (2007) 593.
74. H. Iwahara, T. Esaka, H. Uchida, N. Maeda, *Solid State Ionics*, 3-4 (1981) 359.
75. N. Bonanos, B. Ellis, K. S. Knight, M. N. Mahmood, *Solid State Ionics*, 35 (1989) 179.
76. S. L. Peschle, M.Cifticioglu, D. H. Doughty, J. A. Voight, in Proc. Mat. Res. Soc. Symp., San Francisco, April 1992, edited by M. J. Hampden-Smith, W. G. Klemperer and C. J. Brinker, Mat. Res. Soc., Pittsburg, PA, (1992) p. 101.
77. M. Toprak, Yu Zhang, M. Muhammed, *Materials Letters*, 4460 (2001) 456.
78. J. Will, A. Mitterdorfer, C. Kleinlogel, D. Perednis, L.J. Gauckler, *Solid State Ionics* 131 (2000) 79.
79. C.J. Brinker, A.J. Hurd, K.J. Ward, in: L.L. Hench, D.R. Ulrich (Eds.), Ultrastructure Processing of Ceramics, Wiley, New York, 1988.
80. W.J. Daughton, S.L. Givens, *J. Electrochem. Soc*. 129 (1982) 173.
81. L.W. Tai, P.A. Lessing, *J. Am. Ceram. Soc*. 74 (1991) 501
82. Y. Miyahara, J. Appl. Phys. 71 (1992) 2309.
83. Nakagawa, H. Yohioka, C. Kuroda, M. Ishida, Solid State Ionics 35 (1989) 249.

Chapter 2: High Temperature Proton Conductors (HTPCs)

2.1 General Aspects

The breakthrough of high temperature proton conductors (HTPCs) came in the early 1980s when Iwahara and co-workers showed that doped $SrCeO_3$ and other perovskite-related oxides presented proton conduction in hydrogen-containing atmosphere at high temperatures.[1] After that, several studies have been focused on these perovskite oxides. The most investigated HTCP are $SrCeO_3$, $BaCeO_3$ and $BaZrO_3$-based oxides.

The HTPC chemical composition is written as $AB_{1-x}M_xO_{3-\delta}$, where M represents a trivalent dopant and δ the oxygen deficiency per perovskite unit cell. The introduction of a trivalent dopant cation in the HTCP perovskite structure leads to oxygen vacancy formation, which has been found paramount for proton conduction.[2-4] Typical trivalent cation dopants are Y, Gd, Sc, and Yb.[1]

Exposing HTPCs to water vapour or hydrogen containing atmosphere at high temperatures (300-800 °C) protons are introduced into their perovskite structure by replacing oxygen vacancies with hydroxide ions and/or interstitial protons. Protons incorporated in this manner are not part of the nominal structure or stoichiometry, but are present as foreign species (defects) remaining from synthesis or in equilibrium with ambient hydrogen or water vapour. The conduction mechanism in HTPC involves hopping of protons which are generally not bound to any particular oxygen ion, but are instead free to migrate from one ion to the next. This easy migration results in the high proton conductivity (as high as 10^{-2} S/cm at 600 °C) and low activation energy for proton conduction (0.3-0.6 eV) observed in these oxides.[5-8]

Surrounding HTPCs with water vapour and/or hydrogen, proton transport dominates the overall electrical transport at temperatures approximately below 600 °C. Higher temperatures can lead to water desorption, thereby reducing the concentration of protonic carriers. On the other hand, proton mobility increases with increasing temperature. Therefore, the optimum temperature for proton conduction is a compromise between proton concentration and mobility. Typically, proton conductivity peaks at around 400–600 °C.[10] At higher temperatures, both oxide ion transport and electron transport can become significant.[9] Typically, above 800 °C and at relatively low oxygen partial pressure, oxygen ion conduction appears. Electronic conduction (p-type) is present in the HTPC structure in an atmosphere free from hydrogen and water vapour, at high temperature and high oxygen partial pressure.

Figure 2.1 shows an overview proposed by Norby [10] of proton conductivity values for selected materials in an Arrhenius-type plot. This figure highlights the presence of a temperature region

(between 200 and 500 °C) where any of the reported conductivity falls. Unfortunately, this is an important temperature range. In fact, even if it may seem to cover a small portion of the Arrhenius plot, it is actually the most desirable operating temperature range for both chemical and energy conversion processes. Operating between 200 and 500 °C should allow good materials stability, almost fast reaction kinetics, and manageable heat recovery for a wide variety of applications.[11]

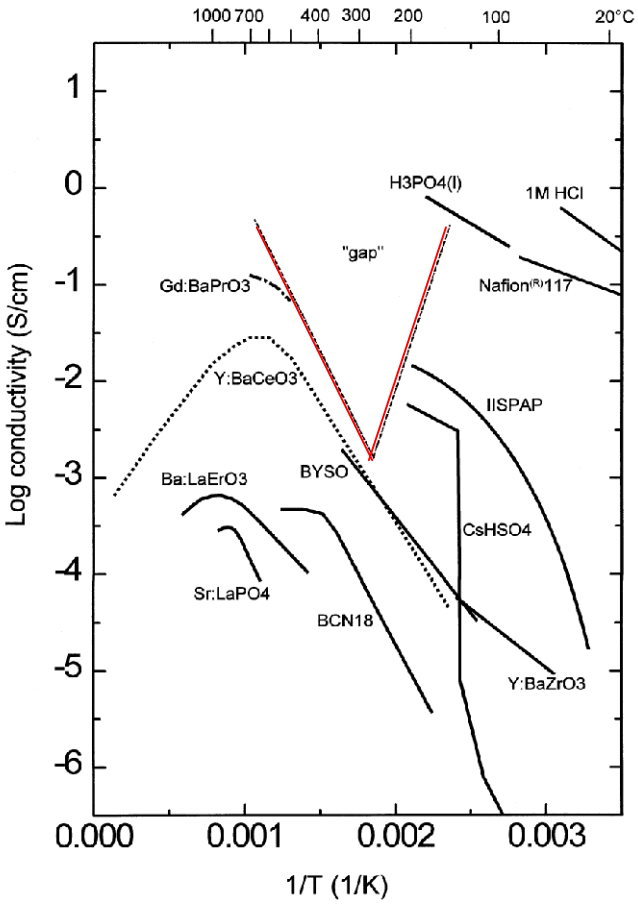

Figure 2.1: Selected literature data for proton conductivity as a function of inverse temperature. [10]

Even if proton conductors offer in general higher conductivity at intermediate temperature compared to oxygen-ion conductors, figure 2.1 highlights that it is still a great challenge to discover a solid electrolyte which is able to work satisfactorily in the so called “Norby gap”. Covering this gap is of prime interest in the breakthrough of a solid electrolyte highly suitable for practical applications.

HTPCs are suitable materials not only for fuel cell electrolyte, but they can be applied to many devices in the field of sensing of hydrogen, energy conversion, and separation of hydrogen. Some of the possible devices using HTPCs are given in Table 2.1.[8].

Function	Phenomena applicable	Devices
EMF	Signal	Hydrogen gas sensor
		Steam sensor
		Hydrocarbons sensor
		Hydrogen sensor for molten metals
		H^+-D^+ isotope sensor
Electrochemical permeation of hydrogen	Power	Fuel cells
	Separation	Hydrogen extractor
		Hydrogen pump for tritium cycle
		Regulator of hydrogen gas pressure
		Steam pump
		Isotope concentrator
	Electrolysis	Steam electrolyser for hydrogen
		H_2S electrolyser for desulfurization
		HCl electrolyser for Cl_2 recovery
		Electrolyser for NOx removal
		Electrolyser for tritium cycle
	Reaction	Membrane reactor for hydrogenation and dehydrogenation of organic compounds

Table 2.1: Possible devices using HTPCs.[8]

Among HTPCs, $BaCeO_3$-based oxides show the highest proton conductivity (about 10^{-2} Scm^{-1} at 600°C).[6] However, as the temperature is raised, they become also oxygen ion conductors and thus their transport number of protons (the ratio between proton conductivity and total electrical conductivity) decreases with temperature.

$SrCeO_3$-based oxides, though achieve rather lower conductivity values than $BaCeO_3$-based oxides, present a proton transport number higher than that of barium cerates.[12]

The most severe problem regarding both barium and strontium cerates based electrolytes is their low chemical stability. They react with acidic gases, e.g. CO_2, and with water vapour to form binary oxides and hydroxides, respectively.[13] Since the use of hydrocarbon fuels (such as methane) can lead to the production of CO_2 and H_2O, the chemical instability of cerates in presence of these gases excludes their application in fuel cell using hydrocarbon fuels.

In comparison to the cerates, $BaZrO_3$-based oxides offer excellent chemical stability against reaction with CO_2 and H_2O. However, barium zirconate-based oxides have shown low conductivity values (about 1 order of magnitude lower than barium cerates for the same operating temperatures). The low electrical conductivity of barium zirconate based oxides is the consequence of the poor

conduction of its grain boundary regions coupled with the material refractory nature. The latter results in small grain size samples with high grain boundary resistance. This fact has also delayed the discovery of their high bulk conductivity, claimed by Kreuer almost twenty years after HTPC breakthrough.[14] The highly refractive nature of the zirconates results also in poor materials densification and the processing of dense electrolyte membranes from these materials remains a significant challenge.[5]

In light of the reactivity of cerates with CO_2 and the difficultly of fabricating dense zirconate electrolytes with large grain size, it is perhaps not surprising that only a few complete cells based on a proton conducing electrolyte have been fabricated and characterized to date.[15]

2.2 HTCP Perovskite Structure

The perovskite structure is a relatively simple crystal structure that has the ABO_3 stoichiometry. In the ABO_3-type structure, the B cation is usually a transition metal element, which forms a six-coordinated octahedron with its neighbouring oxygen ions, and itself is located in the centre. The octahedron is the basic unit for these structures. In fact, the crystal structure of a perovskite can be derived from an assembly of corner sharing metal oxygen octahedral, BO_6, with a larger cation, A, occupying the interstices between these units.[16]

In the case of an ideal cubic perovskite structure, if R_A, R_B, R_O, are the radii of the A, B cations and O anion, respectively, the ratio of R_A+R_O to $2^{½}$ (R_O+R_B) should be unity (the spheres are in direct contact). In a real perovskite system, the structure is rarely ideal at room temperature. Size incompatibilities between the A and the B cations can cause structural modifications to accommodate the non ideal size of cations in the unit cell. These modifications include tilting, distortion, and displacement of the BO_6 octahedral. The result of these distortions occurring in a cubic perovskite unit cell is the formation of lower symmetry tetragonal, orthorhombic or rhombohedral crystal structures, which present values less than unity for the above mentioned ratio. Thus, there can be defined a tolerance factor (*t*):

$$t = \frac{(R_A + R_O)}{\sqrt{2}(R_B + R_O)} \tag{1}$$

describing the extent of distortion of a perovskite structure from the ideal cubic structure due to the mismatch between the A-O and the B-O bond lengths. [9] The range of stability for a perovskite structure in relation to the value of the tolerance factor has been found between $0.75< t <1$. [17] The cubic symmetry has been found stable over the range $0.95< t <1$, while compounds having tolerance numbers in the range $0.75< t <0.9$ typically posses orthorhombic or rhombohedral symmetry.[17]

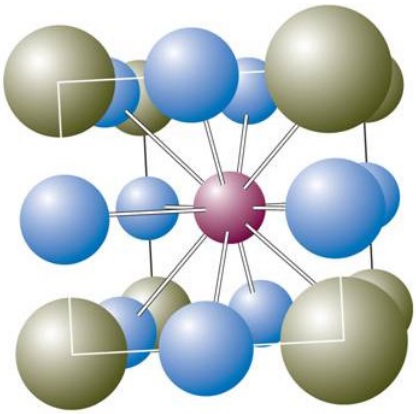

Figure 2.2: Perovskite structure (ABO_3), where the violet sphere is the A-cation, the green spheres the B-cations, and the small blue spheres are the oxygen ions.

The A cation presents valence 2+ and generally has larger ionic radius than the B cation. The coordination number of the A cation is 12. Any cation, which prefers six coordination, could occupy the B position even if its valence is different from 4+. However, for balancing the valence charges, the average valence at B has to be 4+. The flexibility of the B cation makes oxygen anion deficiency possible.[16]

HTCPs are perovskite oxides ABO_3. Doping the B site with a 3+ valence element results in the creation of oxygen vacancies for balancing the valence charge. The introduction of a trivalent dopant M(III) into the ABO_3 perovskite structure is normally assumed to occur via Equ. 2 (written in Kroeger-Vink notation):[9]

$$2B_B^{\,x} + \mathrm{O}_\mathrm{O}^{\mathrm{x}} + M_2O_3 \leftrightarrow 2M'_B + V_O^{\bullet\bullet} + 2BO_2 \qquad (2)$$

The oxygen vacancies form directly as a result of the replacement of the M(III) ions in the B sites of the ABO_3 perovskite structure. The relation between the M(III) concentration and the concentration of the oxygen vacancies created by doping, is given by:[18]

$$[V_O^{\bullet\bullet}] = \tfrac{1}{2}[\mathrm{M(III)}] \qquad (3)$$

with the respect of dopant solubility limit in the host perovskite structure.

The kind of dopant cation and its content have a large impact on the conduction properties of the HTPC perovskite oxides since cations can change the lattice spacing, which influences ion mobility.[19] If the B cation and the dopant present almost the same ionic radii, the site exchange should not introduce any significant lattice distortion in the perovskite structure. Differently, dopants with ionic radii significantly larger than the B cation can create distortions. The change in unit cell volume is normally a measure of the strain induced by doping, and, therefore, of the mismatch between dopant and host ions.[4] Iwahara et al.[19] found that as the ionic radius of the dopant increases, the contribution of oxide ion to the total conduction grows markedly. This is consistent with the fact that large ions enlarge the free volume and favour oxide-ion conduction.

The defect chemistry of these doped ABO_3 perovskites can be complicated by the possibility of partial incorporation of the dopant onto the A site, and not only the B site as desired. The consequence is that fewer oxygen vacancies can be created.

In the following, the crystal structure of the most studied HTPCs ($BaCeO_3$, $SrCeO_3$, $BaZrO_3$ based oxides) will be described in detail.

By neutron diffraction and Raman spectrometry methods, undoped barium cerate has been found to be orthorhombic, space group Pnma, evolving toward ideal cubic perovskite structure upon

heating.[20] The low temperature phases of $BaCeO_3$ contain two crystallographically non-equivalent oxygen sites. In doped $BaCeO_3$, at low temperature the oxygen vacancies do not equally occupy these sites, indicating that they are also energetically non-equivalent. By contrast, in the high temperature phases, the oxygen sites are crystallographically and energetically equivalent.[4,21]

$SrCeO_3$ and its doped derivates are isostructural to $BaCeO_3$, as shown by neutron diffraction [22] and by a single crystal X-ray investigation.[23] However they display a greater distortion from cubic symmetry than $BaCeO_3$, based oxides because of the smaller ionic radius of Sr^{2+} (0.144 nm) compared with Ba^{2+} (0.161 nm).[25] Furthermore, $SrCeO_3$ based oxides do not show temperature induced polymorphism, retaining the orthorhombic structure with two O^{2-} anions with different symmetries to a temperature of at least 1000°.[21] This fact probably results in lower oxygen-ion conductivity and minor water uptake capacity of $SrCeO_3$ based oxides with respect to the $BaCeO_3$ based compounds.[4] Therefore, the lower conductivities and the higher activation energies observed for $SrCeO_3$-based oxides with respect to $BaCeO_3$-based oxides may come from the larger lattice distortion of the strontium cerates compared to barium cerates.[24]

$BaZrO_3$-based oxides have a cubic structure, space group Pm3m. The lattice constant of undoped barium zirconate is 4.1973 Å as reported in the ICSD database, no. 90049. In Y doped barium zirconate, the lattice constant increases linearly with increasing yttrium concentration (as a result of the larger ionic radius of Y^{3+} relative to Zr^{4+}). [25]

2.3 Proton Incorporation and Stability

Protons may be taken up to form hydroxide defects in the oxide structure in presence of water vapour and/or in hydrogen containing gases. Surrounding the specimens with a dry hydrogen atmosphere, the formation of hydroxide defects occurs via:

$$H_2 + 2O_0^x \leftrightarrow 2(OH)_o^\bullet + 2e^- \tag{4}$$

However, the most important reaction leading to the formation of protonic defects is considered the dissociative adsorption of water.[13] Water from the gas phase eventually dissociate into a hydroxide ion and a proton. The hydroxide ion fills an oxygen vacancy, and the proton forms a covalent bond with lattice oxygen. In Kröger-Vink notation this reaction is given by:[9,13,26]

$$H_2O + V_O^{\bullet\bullet} + O_0^x \leftrightarrow 2(OH)_o^\bullet \tag{5}$$

which is exothermic so that protons dominate at low temperatures and oxygen vacancies at high temperatures.[10] According to Equ.5, the saturation value of the proton uptake is equal to twice the initial oxygen vacancy concentration.[26]

Equ.5 may be considered an amphoteric reaction. In fact, in the above reaction a water molecule is split into a hydroxide ion and a proton, so that the oxide acts as an acid in the adsorption of the (OH) ions by oxygen vacancies and as a base in the protonation of the lattice oxygen ions.[13]

Both Equ.4 and Equ.5 may alternatively be written in terms of formation of interstitial protons. However, it is well established that protons are generally not free but spend most of their time bound to oxygen ions.[27] The reason is that protons, infinitesimally small particles, are incapable of occupying a regular interstitial position in the lattice and are inevitably attracted to the electron cloud of neighbouring oxygen ions. The result is that protons remain associated with these oxygen ions, forming a hydroxide ion.[28] For that reason, reactions written in terms of the formation of hydroxide ions are usually preferred; however, the two ways of looking at the defect are equivalent for defect structure evaluations and the two different notations are often used interchangeably.[27,28]

Proton incorporation can also occur with positively charged holes according to:

$$H_2 + 2h^\bullet + 2O_0^x \leftrightarrow 2(OH)_o^\bullet \tag{6}$$

$$H_2O + 2h^\bullet + 2O_0^x \leftrightarrow 2(OH)_o^\bullet + 1/2\,O_2 \tag{7}$$

Generally, because the formation of protonic defects is accompanied by a significant weight increase, the concentration of protonic defects is usually measured by thermal gravimetric analysis.[13]

Figure 2.3 shows normalized hydration isobars of different perovskite oxides. They highlight both the dehydration temperature, which is taken as a measure of the stability of protonic defects, as well as the solubility limit. It has been observed that the water solubility limit approaches the dopant concentration only for cubic perovskite or perovskite with tolerance factor closed to unity, i.e., structures with only one oxygen site.[14]

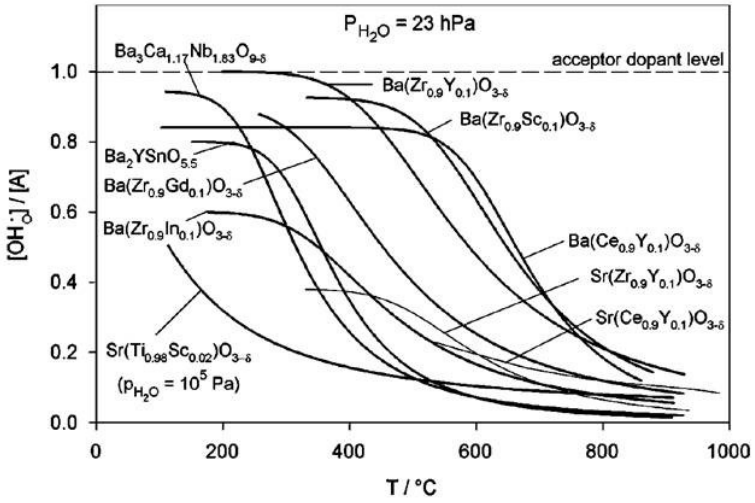

Figure 2.3: Normalized hydration isobars (p_{H_2O}= 23 hPa) for different perovskites. [13]

The equilibrium constant of the hydration reaction (K), which defines the upper temperature limit with respect to dehydration, can be calculated from the data point of the hydration isobar, considering the saturation limits (S) as the maximum defects concentration observed at low temperature. Varying water partial pressure for a given temperature yields the equilibrium constant K of the hydration reaction for that temperature.[7,14] Since the hydration reaction shows approximately Arrhenius behaviour , the hydration enthalpies and entropies can be obtained according to:[7,14]

$$\ln K = \frac{T\Delta S^{\circ} - \Delta H}{kT} \tag{8}$$

Figure 2.4 displays the trend of K for perovskite oxides with Ba in the A-site and Ce, Zr, Nb, and Ti occupying the B-site.[13] It shows that preferentially basic oxides stabilize protonic defects.[13.] In order Sr › Ba and Ti › Nb › Zr › Ce for the occupation of the A and B sites of the perovskite structure, respectively, the electronegativity of the cations decreases and the equilibrium constant for the hydration reaction increases.[13] Therefore, not only structural parameters, but even chemical parameters influence the formation and stability of protonic defects.

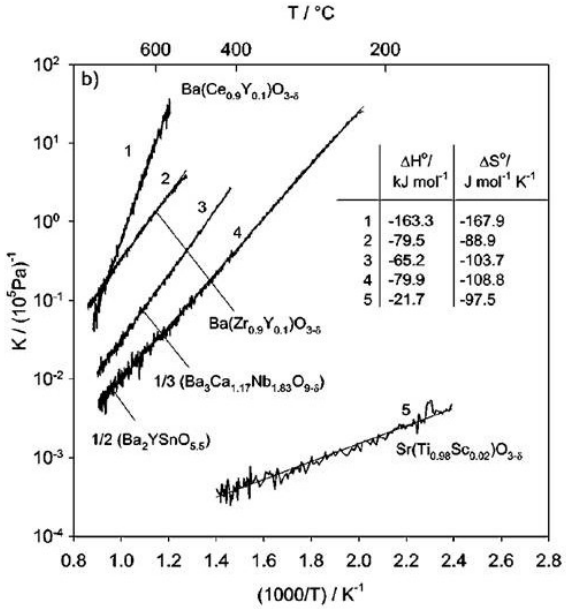

Figure 2.4: the equilibrium constant K of the hydration reaction (Equ.4), calculated from the concentrations of protonic defects.[13]

Figure 2.5 shows the equilibrium constant of the hydration reaction for BZY doped with different elements and the relative thermodynamic data. While the ionic radii of the dopant did not follow a systematic trend with the thermodynamic data, the stability of protonic defects seems to be greatly increased in the case of dopant with high basicity. However, this trend is less significant than that observed for the variation in basicity of the main constituents of the oxides in the perovskite structure.[7]

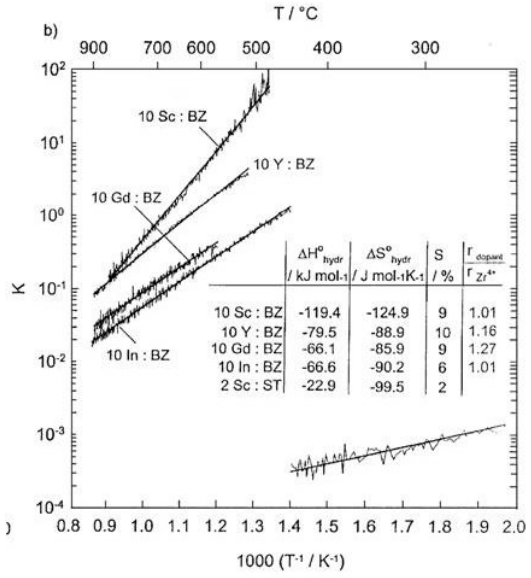

Figure 2.5: The equilibrium constant K of the hydration reaction, for the BZY perovskite doped with different kinds of acceptor dopants.[7]

2.4 Proton Mobility

Two possible mechanisms have been proposed for proton transport in perovskite oxides: hopping between adjacent oxygen ions at normal lattice site positions (Grotthuss-type mechanism) and/or OH^- conduction (vehicle mechanism).[26-29]

Proton conduction mechanism has been controversial for a long time. However, isotope effect (H^+/D^+) measurements on perovskite oxides [26,30] have recently suggested that proton transfer occurs between fixed oxygen sites via the Grotthuss-type mechanism, rather than diffusion of hydroxyl ions.

The principal features of the transport mechanism are: rotational diffusion of the protonic defect around an oxygen ion and proton transfer toward a neighbouring oxide ion.[31] There are conflicting experimental and computational data as to whether transfer or rotation is the rate-determining step. Rotational diffusion has been shown by several experiments [32-35] and by quantum molecular dynamics (MD) simulations [36,37] to be fast with a low-activation barriers (below 0.1 eV), suggesting the proton transfer reaction as the rate-limiting step. On the other hand, experiments based on infrared (IR) spectra analysis[38] showed the presence of strong hydrogen bond interactions, which favour fast proton transfer reactions rather than fast reorientation processes, the latter requiring the breaking of such strong bonds.[31]

For Grotthuss-type proton conduction, the dynamics of oxygen atoms in the neighbourhood of the hydroxide ion influence both the proton transfer and the reorientation step. In particular, those dynamics related to oxygen/oxygen separation, can enhance proton transfer rates. Shortening the oxygen/oxygen separations results in a decreased energetic barrier for proton transfer; for oxygen/oxygen separations $\leq$250 pm even a barrierless (adiabatic) proton transfer can be achieved. The OH^- reorientation rate can be affected by the dynamics of the oxygen atoms. Reorientation can occur more easily increasing the oxygen/oxygen separations, thus lowering the hydrogen bond interaction between nearest neighbour oxygen atoms.[37] Therefore, short oxygen separations favour proton transfer, while large oxygen separations allow rapid reorientation rate. Recently, a reanalysis of a quantum MD simulation demonstrated that both short and large oxygen separations correspond to similar free energies of the entire system, suggesting that the two elemental conduction steps have similar probabilities.[31,39]

Figure 2.6 shows a possible proton diffusion path from the oxygen ion A to the oxygen ion B in doped $BaCeO_3$ HTPC. The proton may move from position 1 to position 2 by its rotational motion around oxygen atom A. Upon bending of the Ce-O bond, the proton can reach position 3, where a hydrogen bond to oxygen atom B can be formed. At this position the proton can move to position 4 if the energetic barrier for proton transfer is reduced by shortening the bond length between A and B. After a successful transfer, the Ce-O bending motion eventually breaks the hydrogen bond and the proton ends up in position 5 which is equivalent to the starting position 1.[37]

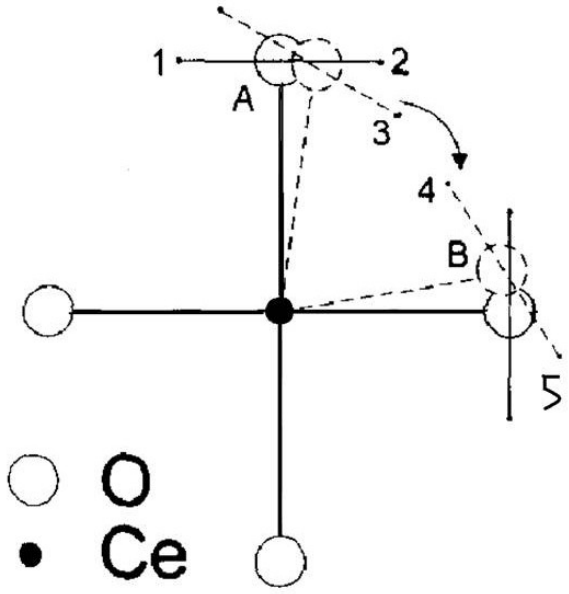

Figure 2.6: Suggested proton diffusion path from oxygen ion A to oxygen ion B. Starting at position 1 the proton passes through positions 2, 3, and 4 to arrive at position 5 which is equivalent to position 1.[37]

Deviations from the ideal cubic perovskite structure may lead to higher activation enthalpy for proton conduction. Studies on structural and dynamical features of protonic defects in Y doped $BaCeO_3$ and Y doped $SrCeO_3$ have investigated this correlation.[40] In the distorted structure of Y doped $SrCeO_3$ the cubic oxygen site degenerates into two sites with probabilities of 1/3 (O_1) and 2/3 (O_2). These oxygen atoms present different chemical interactions with the cations, and therefore have different basicity. [13] This situation leads to different bonding energies between protons and the oxygen on different sites. By contrast, in the high temperature phases of $BaCeO_3$ based oxides, these oxygen sites are crystallographically and energetically equivalent.[4] The different crystal structure of $BaCeO_3$ and $SrCeO_3$ based oxides has been found to affect their proton conduction properties. Whereas in $SrCeO_3$ based oxides proton transport must involve transfer between chemically different O_1 and O_2 sites, in $BaCeO_3$ based oxides protons may show proton transport via the equivalent oxygen sites. This could explain the higher activation enthalpy and lower conductivity in $SrCeO_3$ compared with $BaCeO_3$ based oxides.[24,40]

The mobility of protonic defects is very sensitive not only towards local structural distortions, but also towards local chemical perturbations induced, for example, by acceptor dopants. Traditionally, for oxygen ion conductors, aliovalent dopants were chosen on the basis of the best ionic radius match. However, this approach sometimes fails when used for proton conductor oxides. For example, although the ionic radius of Sc^{3+} and In^{3+} match very well with that of Zr^{4+} and Y has a significantly higher ionic radius than Zr^{4+}, Y doped $BaZrO_3$ shows much higher proton mobility than Sc or In doped $BaZrO_3$ (figure 2.7).[13]

This finding indicates that the chemical matching (electronegativity of the cations and the corresponding acid/base properties of the oxide ions) is very critical for the both the stability (as it has previously reported) and the mobility of protonic defects in the perovskite structure.

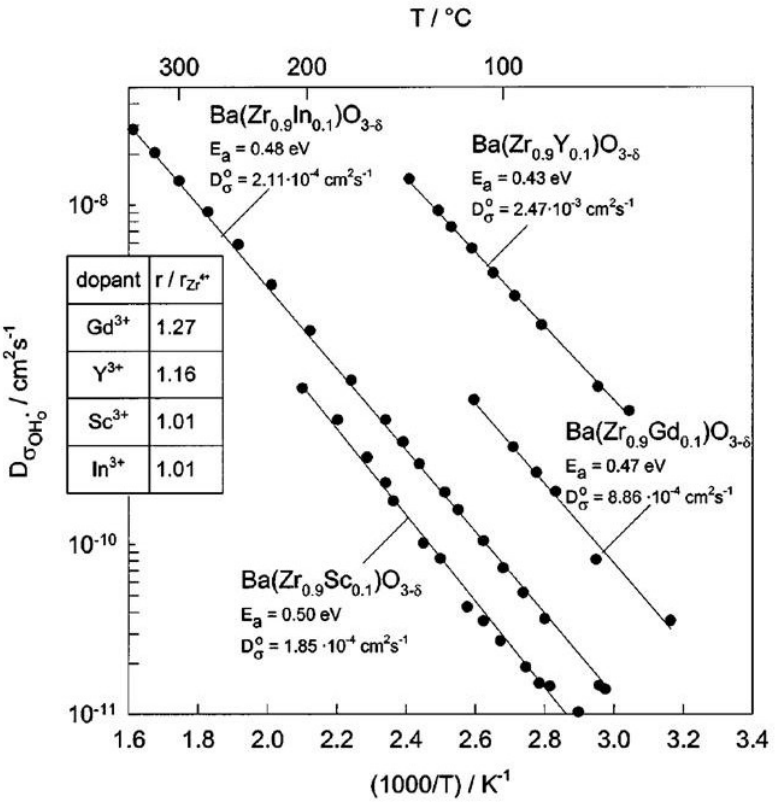

Figure 2.7: Proton mobility in $BaZrO_3$ doped with different acceptor dopants.[7,13]

For Y doped barium zirconate, the activation energy for proton mobility, and also the thermodynamics of hydration, are almost unchanged for different dopant levels. In fact, although Y on the Zr site expands the lattice locally, it actually leaves the acid/base properties of the coordinating oxygen almost unchanged. Differently, the most common observation is a decreasing proton mobility and an increasing activation enthalpy with increasing dopant concentration, as observed, for example, in Y doped $BaCeO_3$. [13]

2.5 Chemical Stability

Highly basic oxides, advantageous to stabilize protonic defects, can easily react with acidic or amphoteric gases, such as CO_2, SO_2, or H_2O to form carbonate, sulphates or hydroxides, respectively. Therefore, high proton defects stability is an antagonistic property with respect to the chemical stability for the considered oxides. In fact, HTCP chemical stability increases in the order cerate ‹ zirconate ‹ titanate, with a trend opposite to that of protonic defect stability.[13]

Barium cerate reacts with CO_2 according to Equ.9, or with H_2O according to Equ.10. However, reaction (10) is not particularly relevant at the operating temperatures expected for a fuel cell,[9] and thus the remainder of the discussion will be limited to reaction (9).

$$\mathrm{BaCeO_3} + CO_2 \rightarrow BaCO_3 + CeO_2 \quad (9)$$

$$\mathrm{BaCeO_3} + \mathrm{H_2}O \rightarrow Ba(OH)_2 + CeO_2 \quad (10)$$

The reaction of an ABO_3 perovskite with CO_2, as given for $BaCeO_3$ above, can be broken into the following two reactions:[9,41,42]

$$\mathrm{ABO_3} \rightarrow AO + BO_2 \quad (11)$$

$$\mathrm{AO} + \mathrm{CO_2} \rightarrow ACO_3 \quad (12)$$

Data on the formation enthalpy of the perovskite from the binary oxides (Equ.11) and on the stability of the carbonate with respect to AO oxide (Equ.12) help to understand the thermodynamics of the above reactions. [38] Table 2.2 summarizes the formation enthalpy values of the main HTPC perovskite.

ABO_3	$\Delta H°$[kJ/mol]	Method	Source
$BaCeO_3$	-54	solution calorimetry	[43]
	-57	solution calorimetry	[44]
	-52	solution calorimetry	[45]
$SrCeO_3$	-49	differential calorimetry	[46]
	-5	solution calorimetry	[43]
	-6	solution calorimetry	[44]
$BaZrO_3$	-128	galvanic cell	[47]
$SrZrO_3$	-74	galvanic cell	[47]

TABLE 2.2: Thermodynamic parameters for the reaction (9) for the standard state T=298.15 K and p=1 atm.

The most negative values of the $BaZrO_3$formation enthalpy reflects the high chemical stability of this oxide compared to the others reported in Table 2.2.

It has been observed that ΔH° for the formation of the perovskite from the individual oxides shows a correlation with the perovskite tolerance factor *t*.[9] This is somehow not surprising since both reflect the compatibility of cations with the perovskite structure. The standard formation enthalpy of some HTPC perovskite oxide are plotted as a function of their tolerance factor in figure 2.8. Increasing perovskite tolerance factor, an increasing stability in the order cerates ‹ zirconates ‹ titanates can be observed.[48]

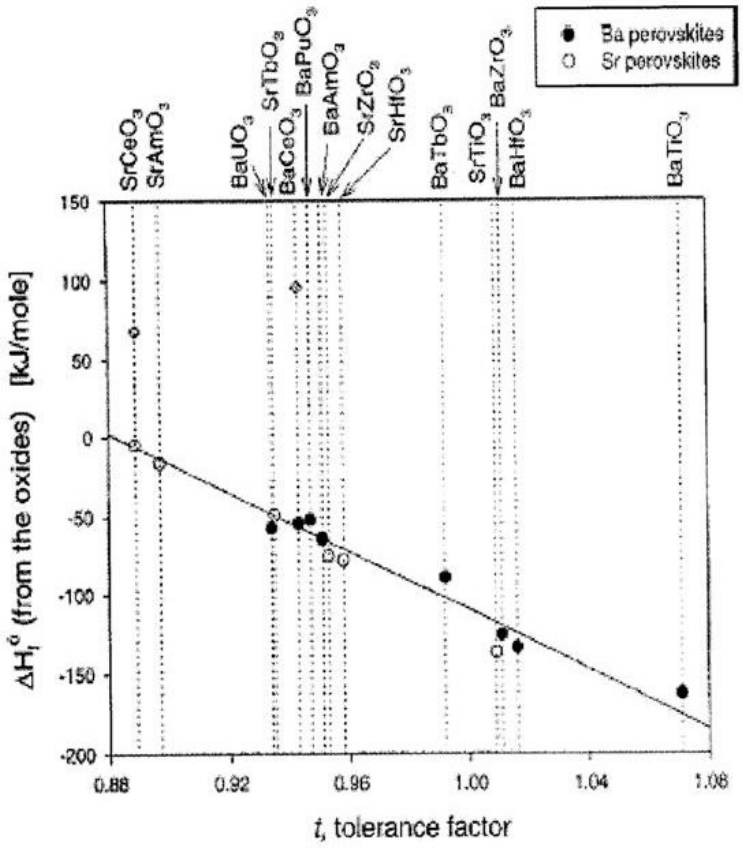

Figure 2.8: The negative of the enthalpy of reaction (11) plotted as a function of perovskite tolerance factor.[9]

Notable exceptions are two data points with positive ΔH° for $BaCeO_3$ and $SrCeO_3$ as determined by Gopalan and Virkar.[49] The discrepancy between these results and those of the calorimetric measurements for cerates [43-48] has been not easily resolved. The weight of the experimental evidence suggests that the enthalpy of formation from the oxides for both $BaCeO_3$ and $SrCeO_3$ should be negative as determined calorimetrically.[9]

ABO_3	ΔH°[kJ/mol]	Method	Source
$BaCeO_3$	-214	Calculated	[9]
	-357	Galvanic cell	[50]
$SrCeO_3$	-229	Calculated	[9]
	-298	Galvanic cell	[50]
$BaZrO_3$	-140	Galvanic cell	[48]
$SrZrO_3$	-160	Galvanic cell	[48]

TABLE 2.3: Thermodynamic parameters for the reaction: ABO_3+CO_2 ACO_3+MO_2 for the standard state, T=298.15 K and p=1 atm.

Table 2.3 shows the enthalpy values for the formation of the carbonate from the perovskite oxides (Equ.12).

The data presented in Table 2.3 suggest that the zirconates, especially $BaZrO_3$, are more stable against carbonate formation than the cerates.

For the considered perovskites, reduction of the crystallographic symmetry has a larger effect on the stability of protonic defects than on the thermodynamic stability. The stability of $BaCeO_3$ and $SrCeO_3$ with respect to carbonate formation is very similar, but protonic defects are better stabilized in $BaCeO_3$ than in $SrCeO_3$, which has a stronger orthorhombic distortion. [50]

2.6 Partial Ionic and Electronic Conductivities

The necessary presence of oxygen vacancies for proton defect generation in HTPCs implies that also oxygen-ion conductivity can occur in some conditions. Furthermore, hole conduction appears as consequence of oxygen incorporation which produces holes according to:

$$\frac{1}{2}O_2 + V_o^{\bullet\bullet} \leftrightarrow O_0^x + 2h^{\bullet} \qquad (13)$$

With increasing temperature, the appearance of positively charged defects generally occurs in the order: hydroxide ions, holes, and oxygen vacancies.[38] The temperature at which this happens depends on the dopant concentration, the external oxygen and water vapour partial pressure, and the equilibrium constants of all the involved reactions.

In complete absence of hydrogen and water vapour, Equ.13 indicates that oxygen ions are the main charge carriers at low oxygen partial pressure.[12,51]. Increasing oxygen partial pressures, electronic (p-type) conduction appears consuming oxygen vacancies and thus reducing the oxygen ion conduction. [18,51-54] It should be pointed out that elevated temperatures (T≥700-800°C) favour water desorption from these perovskite structures and thus electronic or oxygen-ion conduction can appear also water vapour containing atmospheres. Therefore, in humidified oxygen containing atmosphere the incorporation of O_2 to form holes (Eq.13) competes, in a determined temperature range, with the dissolution reaction of H_2O to generate protons (Eq.5) since both consume oxygen vacancies.

Rare-earth-doped BaCeO is a good example of a mixed conductor exhibiting large contributions of all three conductivities (protonic, oxygen-ion and p-type) depending on the surrounding conditions. [10] The magnitude of the p-type electronic conductivity depends on the valence states of the cations involved, and thus, most of these materials show only small values of partial electronic conductivity. Some of them can also exhibit electronic n-type conduction under sufficiently reducing conditions. The oxides with considerable n-type conduction contain a readily reducible cation. Thus, the n-type conduction is relatively high in BaCeO and other cerates, while is not almost negligible in the zirconates.[10]

From all the above considerations, it is evident that protonic, oxygen-ion, p-type and n-type electronic conductivity depend strongly on external parameters, such as temperature, gas surrounding atmosphere, oxygen and water partial pressure. Figure 2.9 shows the predominant defect species in the p_{O_2}-p_{H_2O} plane for Yb-doped strontium cerate.[54]

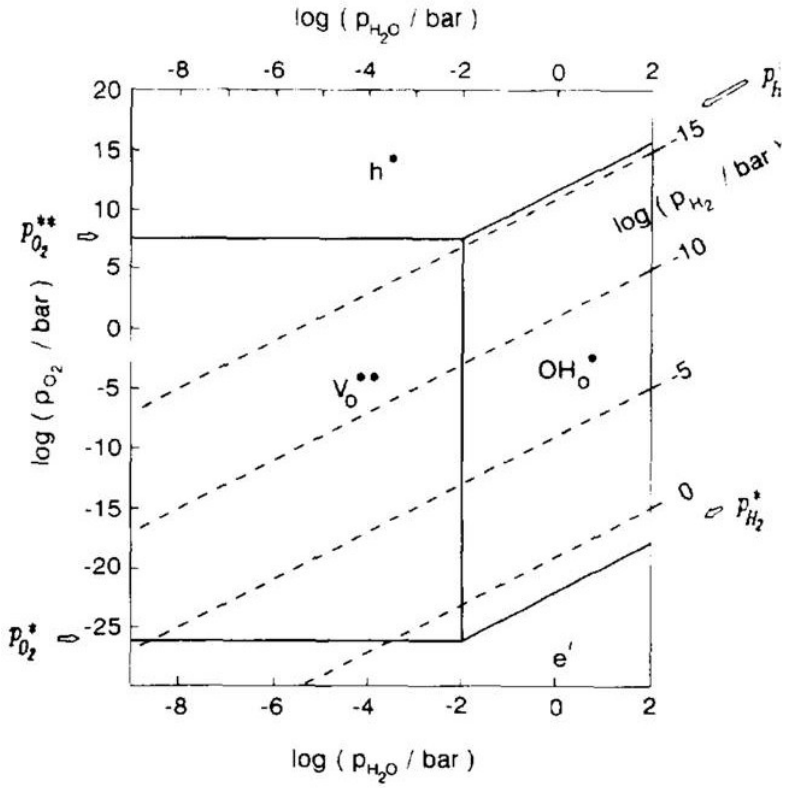

Figure 2.9: Predominant defect species in the p_{O_2}-p_{H_2O} plane for Yb-doped strontium cerate. [54]

In general, appreciable electronic conductivity limits the application as electrolyte materials because it decreases cell open circuit voltage. Differently, mixed protonic-electronic conduction could be a key property for anode or cathode materials working in a SOFC based on a proton conductor electrolyte.

2.7 References

1. H. Iwahara, T. Esaka, H. Uchida and N. Maeda. *Solid State Ionics,* 3/4 (1981) 359.
2. H. Uchida, N. Maeda, H. Iwahara, *Solid State Ionics*, 11 (1983) 117.
3. H. Iwahara, T. Yajima, T. Hibino, H. Ushida, *J. Electrochem. Soc*, 140 (6) (1993) 1687.
4. N. Bonanos, K.S. Knight, B. Ellis, *Solid State Ionics*, 79 (1995) 161.
5. H.G. Bohn, T. Schober, *J. Am. Ceram. Soc*. 83 (2000) 768.
6. K. Katahira, Y. Kohchi, T. Shimura, H. Iwahara, *Solid State Ionics*, 138 (2000) 91.
7. K.D. Kreuer, St. Adams, W. Munch, A. Fuchs, U. Klock, J. Maier, *Solid State Ionics*, 145 (2001) 295.
8. H. Iwahara, Y. Asakura, K. Katahira, M. Tanaka, *Solid State Ionics*, 168, (2004) 299.
9. S.M. Haile, G. Staneff, K.H. Ryu, *J. of Materials Science*, 36 (2001) 1149.
10. T. Norby, *Solid State Ionics*, 125 (1999) 1.
11. T. Norby, *Nature*, 410 (2001) 877.
12. H. Iwahara, *Solid State Ionics*, 77 (1995) 289.
13. K.D.Kreuer *Annu. Rev. Mater. Res*., 33 (2003) 333.
14. K.D Kreuer. *Solid State Ionics*, 25 (1999) 285.
15. S.M. Haile, *Acta Materialia*, 51 (2003) 5981.
16. Z.L. Wang, Z.C. Kang, *Functional and Smart Materials*, 1998, Plenum Press, NY.
17. A.F. Sammells, R.L. Cook, J.H. Wright, J.J. Osborne, R.C. MacDuff, *Solid State Ionics*, 52 (1992) 111.
18. R.V. Kumar, *J. of Alloys and Compounds*, 408–412 (2006) 463.
19. H. Iwahara, T. Yajima, H. Ushida, *Solid State Ionics*, 70/71, (1994) 267.
20. F. Genet, S. Loridant, C. Ritter, G. Lucazeau, *J. Phys. Chem. Sol*., 60 (1999) 2009.
21. P.J. Shlichta, *Solid State Ionics*, 28-30 (1988) 480.
22. J. Ranlov, B. Lebech, K. Nielsen, *J. Mater. Chem*., 5 (1995) 743.
23. J. Ranlov, K. Nielsen *J. Mater. Chem*., 4 (1994) 867.
24. J.X. Wang, L.P. Li, B.J. Campbell, Z. Lv, Y. Ji, Y.F. Xue, W.H. Su, *Materials Chemistry and Physics*, 86 (2004) 150.
25. Y. Yamazaki, P.Babilo, S. M. Haile, *Chem. Mater*,(2008).
26. A.S. Nowick, Y.Du, *Solid State Ionics*, 77 (1995) 137.
27. N. Bonanos, *Solid State Ionics*, 145 (2001) 265.
28. T. Norby, *Solid State Ionics*, 40/41 (1990) 857.
29. Yajima, H. Iwahara, *Solid State Ionics*, 50 (1992) 281.
30. *Solid State Ionics* 69 (1994) 303.

31. K.D. Kreur *Solid State Ionics,* 136–137 (2000) 149.
32. M. Pionke, T. Mono, W. Schweika, T. Springer, T. Schober, *Solid State Ionics,* 97 (1997) 497.
33. T. Matzke, U. Stimming , C. Karmonik , M. Soetramo, R. Hempelmann , F. Guthoff, *Solid State Ionics,* 86–88 (1996) 621.
34. R. Hempelmann, M. Soetramo, O. Hartmann, R. Wappling, *Solid State Ionics,* 107 (1998) 269.
35. K.D. Kreuer, A. Fuchs, J. Maier, *Solid State Ionics,* 77 (1995) 157.
36. W. Munch,G. Seifert ,K.D. Kreuer,J. Maier, *Solid State Ionics,* 97 (1997) 39.
37. W. Munch, G. Seifert , K.D. Kreuer, J. Maier, *Solid State Ionics,* 86–88 (1996) 647.
38. K.D. Kreur, *Solid State Ionics,* 97 (1997)1.
39. *Solid State Ionics* 136-137 (2000) 183
40. W. Munch, K.D. Kreuer,S. Adams,G. Seifert, J. Maier, *Phase Transitions,* 68 (1999) 567.
41. Solid State Ionics 77 (1995) 185.
42. Solid State Ionics 136 (2000) 313.
43. J Goudiakas, R. G. Haire, J . Fuger, *J. Chem.Thermodynamics*, 22 (1990) 577.
44. E.H P . Cordfunke, A.S. Booij, M.E.Huntelaar, *ibid.*, 30 (1998) 437.
45. L.R. Mensch, N. Mensi, in Proceedings of the 15th Rare Earth Research Conference, June 15–18, 1981, Univ. of Missouri, Rolla, edited by G. J. McCarthy and J. J. Rhyne (Plenum Press, New York, 1982) p. 279.
46. R. Saha, R. Babu, K. Nagarajan, C.K. Mathews, *Thermochimica Acta*, 120 (1987) 29.
47. K.T. Jacob, Y. Waseda, *Met. Mat. Trans*., 26B (1995) 775.
48. M. Scholten, J. Schoonman, J.Miltenburg, HAJ. Oonk, *Solid State Ionics,* 61 (1993) 83.
49. S . Goplan, A.V. Virkar, *J. Electrochem. Soc.*, 140 (1993) 1060.
50. S.M. Haile, *Solid State Ionics,* 44 (1991) 305.
51. N. Bonanos, *Solid State Ionics*, 53-56 (1992) 967.
52. V.V. Kharton, I.P. Marozau, G.C. Mather, E.N. Naumovich, J.R. Frade, *Electrochim. Acta*, 51 (2006) 6389.
53. P. Pasierb, M. Wierzbicka, S. Komornicki, M. Rekas, *J. Power Sources*, 173 (2007) 681.
54. T. Schober, W. Schilling, H. Wenzl, Solid State Ionics, 86-88 (1996) 653.

PART B: EXPERIMENTAL RESULTS

Chapter 1: Optimization of a Soft Chemistry Procedure for HTPC Synthesis and Their Characterization

1.1 Introduction

Literature conductivity values related to doped barium zirconate electrolytes vary more than one order of magnitude suggesting that the fabrication processes have a significant influence on the electrical properties of these proton conductor electrolytes.

Solid state reaction synthesis procedure requires high calcination temperature (1400-1500°C) and long annealing time (10-30 h), leading often to the formation of uncontrolled particle size (typically larger than 1 μm). Differently, wet chemical methods allow the reduction of the processing temperature, producing powders with controlled compositional homogeneity, purity, and microstructure down to nanometric scale.

In this work, a sol gel synthetic procedure was optimized to control microstructure and single phase formation of $BaZr_{0.8}Y_{0.2}O_{3-\delta}$ (BZY) electrolyte at relative low processing temperatures. A wet chemical method able to reduce calcination and sintering temperature can greatly improve the electrical performance of BZY electrolyte. When BZY powder is produced by solid state reaction, high sintering temperatures (1700-2200°C) are required for its densification, and this lead to barium evaporation from the BZY structure. Reduction of barium content favors the incorporation of the Y dopant on the A site instead that on the B site of the ABO_3 perovskite structure, decreasing oxygen vacancies and thus proton concentration. This results in lower proton conductivity.

The same sol gel synthesis was optimized also for the preparation of $BaCe_{0.8}Y_{0.2}O_{3-\delta}$ (BCY) proton conductor electrolyte.

The choice of Y as a dopant for both electrolytes was based on the good ionic radius match between yttrium and cerium, and because it has been identified as a perfect acceptor dopant for barium zirconate, as reported in Chapter 2.4, Part A.[1]

The BZY and BCY synthesized powders were characterized by X-ray diffraction (XRD) and thermogravimetric (TG) analysis. The chemical stability of BCY and BZY was tested exposing the calcined powders to CO_2 atmosphere at high temperature and performing XRD analysis after the treatment. The chemical stability of BCY and BZY proton conductor electrolytes was tested carrying out a CO_2 thermal treatment. CO_2 is generated at the anode side when hydrocarbons are used as fuel during cell operation.

BZY showed good chemical stability, while BCY completely decomposed in barium carbonate and cerium oxide. On the basis of this result, only BZY had been tested as electrolyte material in hydrogen-air breathing fuel cell tests.

1.2 BCY and BZY Powder Synthesis and Characterization

The synthesis of BZY and BCY was carried out by sol-gel process reacting the metal nitrates in the presence of citric acid (CA) as a chelating agent. The synthesis parameters (solvent choice and reactants concentration) were optimized to obtain BZY and BCY single phase powders at relative low processing temperatures.

Water (W) and ethylene glycol (EG) were used as solvents. The starting materials were commercial $Ba(NO_3)_2$ (3% H_2O, Aldrich, 99.999%), $C_e(NO_3)_3x6H_2O$ (Aldrich, 99.9%), $(CH_3CO_2)xZr(OH)y$ (Aldrich) and $Y(NO_3)_3x6H_2O$ (Aldrich,99.9%).

Several BZY and BCY powder samples were prepared using different molar ratios citric acid:total metal content (CA:TMC) with each one of the two solvents: 1:1 (batch 01, 01EG and 01W), 2:1 (batch 02, 02EG and 02W) and 3:1 (batch 03, 03EG and 03W). Appropriate molar ratios of metals and CA were mixed in a minimum volume of solvent to obtain a transparent solution. The solutions were heated to 150 °C under continuous stirring until obtaining a viscous gel. By further heating, the gel was converted into a pale yellow ash that was ground in a ball mill overnight.

Figure 1.1 presents a scheme of the different sol gel synthesis procedures.

Figure 1.1: Scheme of the different sol gel synthesis procedures.

The 02W and 02EG BZY and BCY precursors were characterized by thermogravimetric (TG) analysis. TG curves are shown in figure 1.2.

For all the batches the main weight loss occurred around 200-500°C because of the decomposition of organic matrix. The weight loss reached ~50% and ~60% of the total weight for the BZY 02W and 02EG batch, respectively. In the case of BCY the observed weight loss was larger reaching ~70% and ~90% of the total weight for the 02W and 02EG batch, respectively.

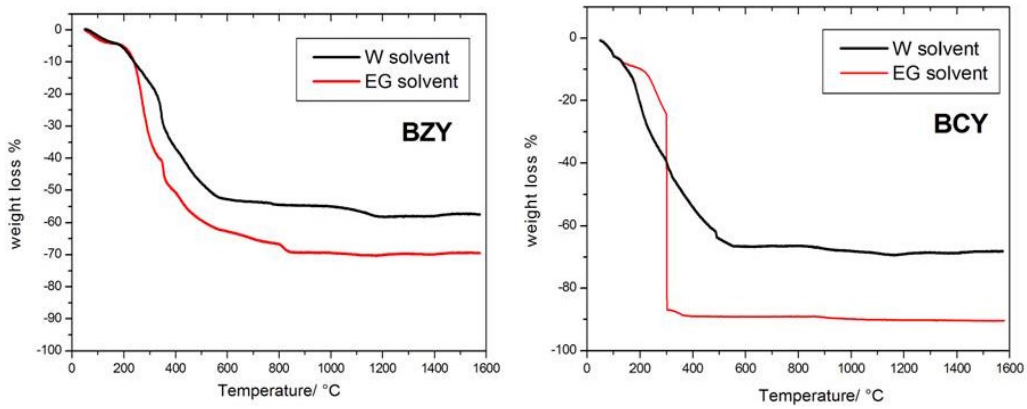

Figure1.2: TG curves of the 02W and 02EG precursors for the BZY and BCY oxides.

At temperature above 500°C the decomposition of organic matrix was almost completed and the TG curves of BCY and BZY precursor followed a similar trend. At 800°C, the total weight loss of the samples prepared in water solvent was lower than what observed for the samples prepared in ethylene glycol. At 1100-1200°C another weight loss can be observed in the TG curves related to the precursors synthesized using water as solvent, while no significant weight loss occurred for the samples produced using EG above 900 and 500°C for BZY and BCY, respectively.

On the basis of TG analysis, the 02W and 02EG synthesis precursors were heated at 800°C for 5 h to remove organic materials and XRD analysis was performed on the resulting powders. Figures 1.3 and 1.4 show the XRD patterns of the 02W and 02EG BZY and BCY precursors after the thermal treatment. For comparison the patterns relative to the perovskite structures of BZY and BCY (JCPS 81-1386 and 74-1299, respectively) were added.

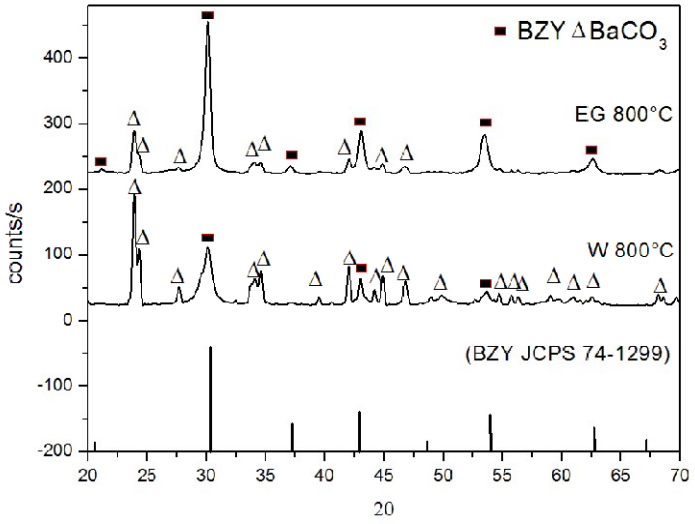

Figure 1.3: XRD patterns of BZY 02W and 02EG precursors after the thermal treatment at 800°C for 5 h.

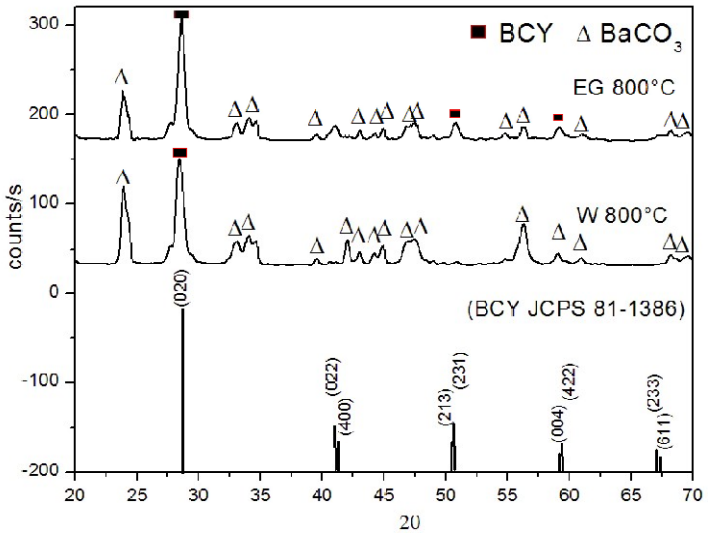

Figure 1.4: XRD patterns of BCY 02W and 02EG precursors after the thermal treatment at 800°C for 5 h.

In the case of BZY (fig. 1.3), the XRD pattern of the EG-derived sample calcined at 800 °C showed the reflection lines related to the cubic BZY perovskite structure together with some barium carbonate peaks. On the other hand, in the XRD pattern of the BZY water-derived sample the predominant phase was that of barium carbonate.

For the BCY samples the results are similar to those described for BZY. The XRD of the EG-derived sample presented all the characteristic peaks of the BCY perovskite structure and several peaks related to barium carbonate. In the XRD pattern related to the W-derived sample larger amount of barium carbonate phase was observed and only the most intense reflection line (020) of the BCY perovskite structure was present.

The TG data and the XRD analysis above reported suggest that the use of EG solvent allows formation of the desired perovskite structure at a lower heating temperature with respect to W solvent. These findings can be explained on the basis of different interactions between CA and the two solvents. It is known that CA undergoes polyesterification reaction in the presence of EG creating a polymeric network where the coordinated metal ions can be homogeneously distributed.[2-4] When water is used as a solvent, the formation of such an extended network does not occur. As a consequence, a rise in the oxide formation temperature was observed. Therefore, EG was chosen as the most appropriate solvent for the synthesis procedure.

To identify the best CA/TMC ratio, the samples derived from batches 01E, 02E and 03E of BZY and BCY oxides were calcined between 900 and 1200 °C (with 100°C steps) for 5 h. The lowest calcination temperatures needed to obtain BZY and BCY single phase formation were 1100 and 1000°C, respectively.

Figure 1.5 shows the XRD patterns of the BZY and BCY powders, deriving from the batches 01EG, 02EG, and 03EG, calcined at 1100 and 1000°C, respectively.

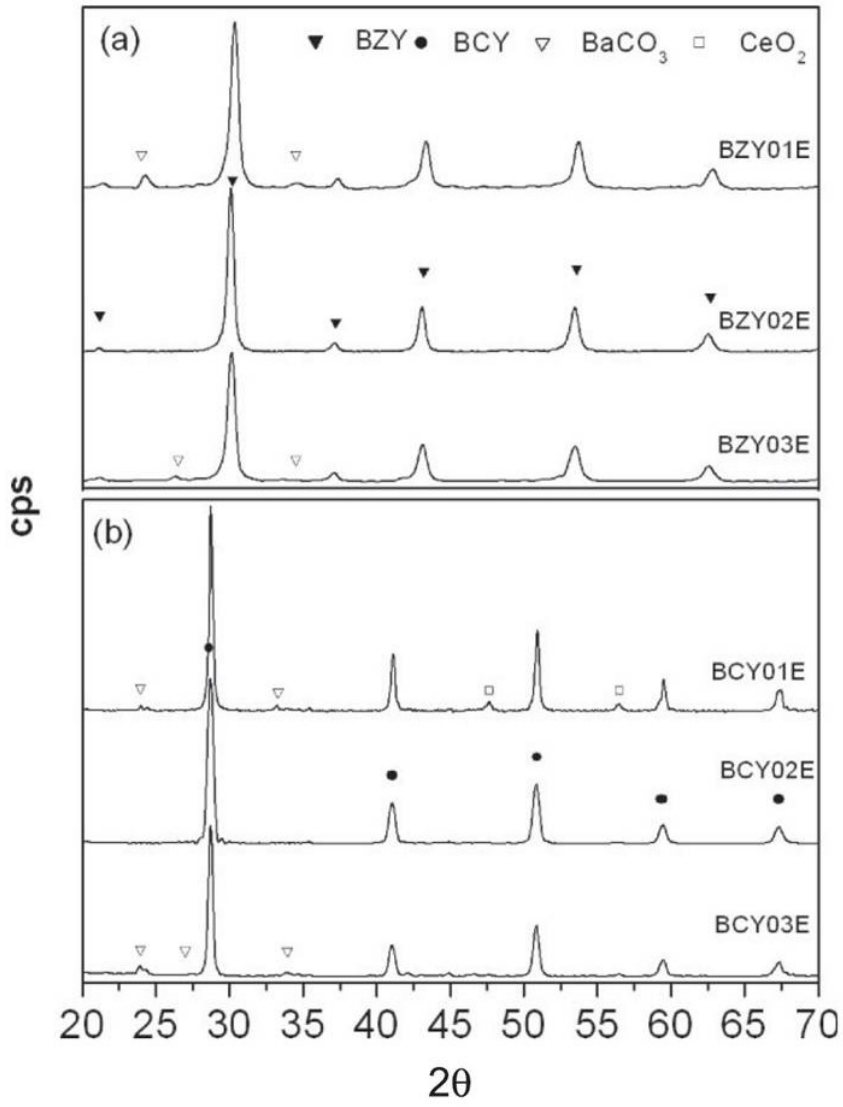

Figure 1.5: XRD patterns of BZY (a) and BCY (b) powders, from batch 01E, 02E and 03E, calcined at 1100 and 1000 °C for 5 h, respectively.

Barium carbonate phase was observed in the XRD patterns of batches BZY-01EG, BZY-03EG (figure 1.5a), BCY-01EG and BCY-03E (figure 1.5b).

Pure phase formation at the lowest calcination temperature was observed both for BZY and BCY oxides derived from the batch 02EG. BZY-02EG sample calcined at 1100°C presented a pure cubic perovskite phase. The BCY-02EG batch calcined at 1000°C showed a pure orthorhombic perovskite phase.

These findings suggest that the BZY and BCY phase formation were significantly influenced by the CA/TMC ratio.[2,4]. With the CA/TMC ratio set at 1:1, each metal ion might be complexed by only one molecule of CA, while when the ratio is set at 2:1, two molecules of CA are available for each metal cation.[3].It is possible that the resin structure with the CA/TMC ratio set at 2:1 has a more uniform spatial distribution of metal ions, preventing clustering or non-homogeneity in the structure. A higher concentration of CA led to the undesired formation of carbonates. Therefore, two opposing factors seem to simultaneously affect the pure phase formation of the BZY and BCY oxide. On one hand, a relatively high CA/TMC ratio is needed to obtain a uniform spatial distribution of metal ions; on the other hand, the CA/TMC ratio should be sufficiently low to avoid the introduction of an excessive amount of organic that is difficult to remove. Thus, the best results were achieved using a ratio of CA to TMC set at 2:1, leading the formation of a pure BZY perovskite phase at 1100 °C and pure BCY phase at 1000°C.

Figure 1.6 shows typical FE-SEM micrographs of BZY and BCY powder synthesized using EG as a solvent and a ratio of CA to TM set at 2:1, calcined at 1100 and 1000°C for 5 h, respectively. The optimized sol gel procedure, requiring low calcination temperature for pure phase formation, actually led to the formation of single phase powders with nanometric particle size, 50nm observed in the SEM micrographs.

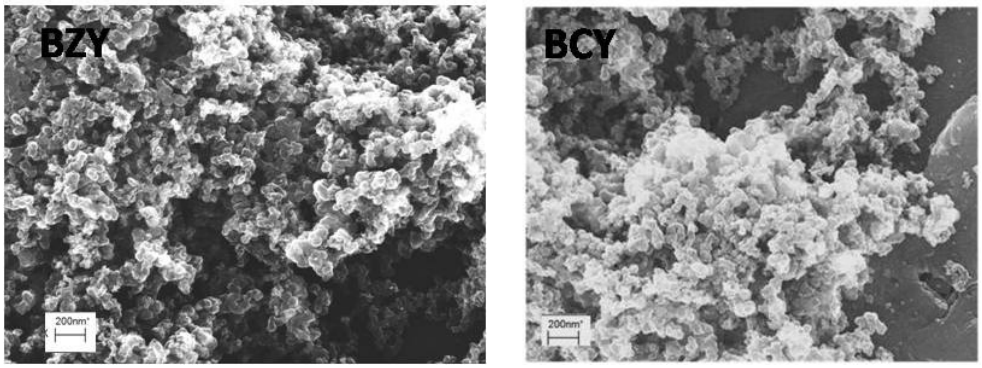

Figure 1.6: SEM micrograph of BZY and BCY powders calcined at 1100 and 1000°C, respectively.

1.3 BCY and BZY Chemical Stability in CO_2

Chemical stability represents an essential requirement for fuel cell electrolyte application.

The production of pure H_2 involves energetically and economically expensive processes. For this reason the research is recently oriented towards the utilization of hydrocarbon fuels. However, the use of hydrocarbon fuels leads to CO_2 generation at the anode side during fuel cell operation. Prolonged exposure to CO_2 can lead to chemical and mechanical degradation of the electrolyte making it unsuitable for commercial applications.

The chemical stability of the calcined BZY and BCY powders was investigated exposing them to CO_2 at 900 °C for 3 h. Figure 1.7 shows the XRD patterns of BZY and BCY powders, both as calcined and after CO_2 thermal treatment.

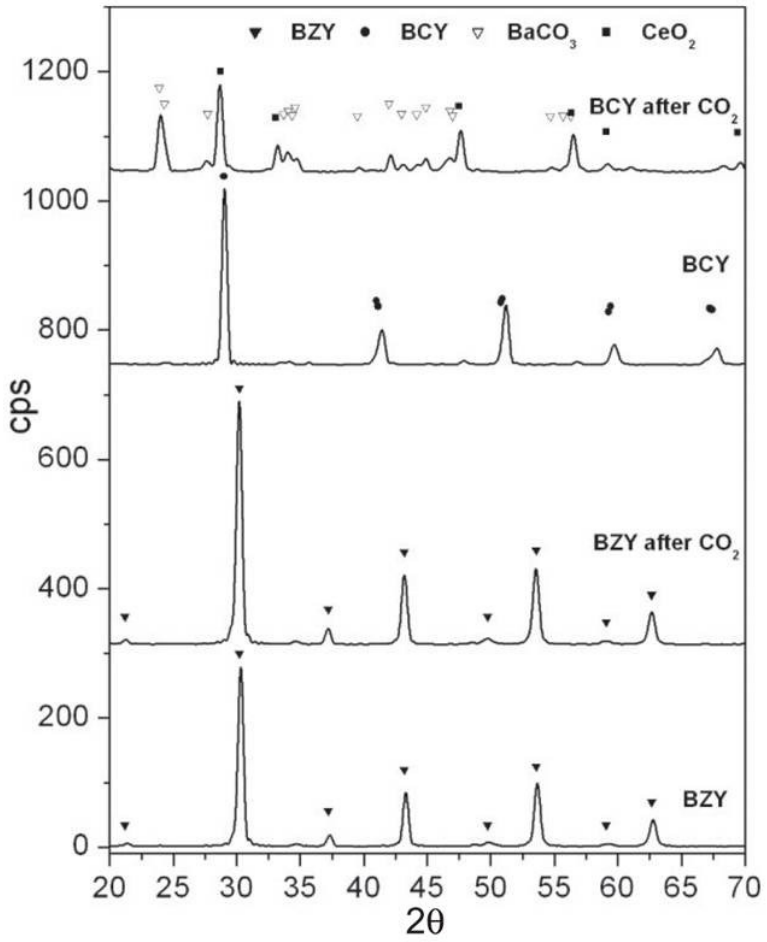

Figure 1.7: XRD patterns of BZY and BCY powders before and after exposure to CO_2.

The XRD pattern of BZY powder did not show secondary phases after exposure to CO_2. In contrast, in the XRD pattern of the CO_2 treated BCY powder the characteristic BCY perovskite peaks completely disappeared and only the reflection lines relative to barium carbonate and cerium oxide were revealed.

This finding indicates that the synthesized BZY powder presents good chemical stability, while BCY undergoes extensive decomposition in CO_2 atmosphere precluding its applicability as a solid electrolyte in an IT-SOFC.

On the basis of this result, only the electrical performance of the BZY electrolyte oxide, which presents suitable chemical stability for fuel cell application, was tested by electrochemical impedance spectroscopy (EIS) and in hydrogen-air breathing fuel cell tests.

1.4 BZY Electrical Conductivity

Conductivity measurements were carried out in wet (3 vol. % H_2O) hydrogen between 350–750°C over the frequency range 1 Hz-1 MHz, using a Frequency Response Analyzer coupled with a dielectric interface. Symmetrical cells were fabricated depositing porous platinum paste as electrodes on both sides of the pellets.

Fig. 1.8 shows the temperature dependence of BZY electrolyte conductivity. Up to 700°C the Arrhenius curve showed linear behavior and the calculated activation energy for proton conduction was Ea = 0.61 eV. This value is consistent with literature data.[5-7] Above 650°C the conductivity decreased approaching an almost constant value. This finding is consistent with thermodynamic studies [1] which showed that at high temperature sample dehydration occurs, so that the concurrent effects of dehydration and enhanced proton mobility result at high temperatures in a weaker conductivity temperature dependence.

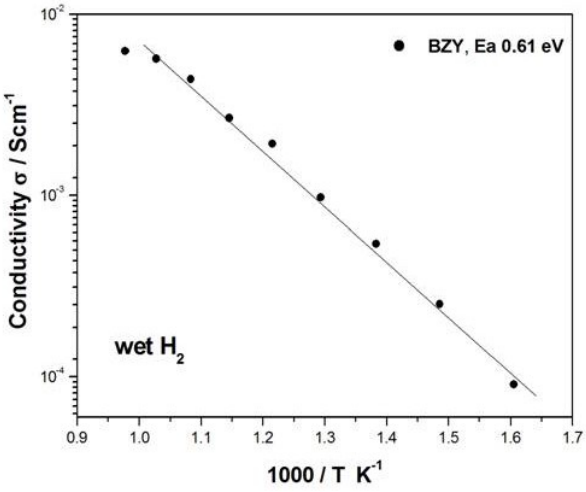

Figure 1.8: BZY electrical conductivity temperature dependence measured in wet hydrogen atmosphere.

The conductivity value of the BZY electrolyte does not reached the target value [8] of 10^{-2} S/cm in the temperature range of 350-750°C, which is of interest for IT-SOFC application.

1.5 BZY Fuel Cell Performance

For fuel cell tests, the BZY sample was mounted at the end of an alumina tube with a gas tight ceramic paste seal. Gold wires were fixed with platinum paste on the anode and cathode electrodes to act as current collectors. During fuel cell operation, the anode surface was exposed to wet hydrogen (3 vol. % H_2O) and the cathode to ambient air. The electrochemical measurements were performed with a Multichannel Potentiostat VMP3. Figure 1.9 shows a schematic view of our home-made experimental set-up for testing fuel cells in operating conditions.

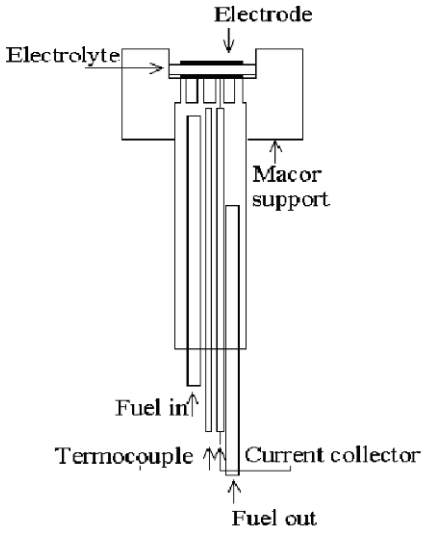

Figure 1.9: Experimental set-up for fuel cell tests.

Figure 1.10 shows the voltage and power density output of a Pt/BZY/Pt single cell (electrolyte thickness of 1.0 mm) as a function of current density at different operating temperatures (500, 600, and 700 °C).

The recorded open circuit voltage (OCV) was almost close to the estimated Nernst voltage (1.09V at 500°C, 1.07 V at 600°C, and 1.04 at 700°C), demonstrating that the density of the electrolyte was sufficient to prevent gas leakage through it. The maximum power density, 3.6 $mWcm^{-2}$, was reached at 700 °C. Slightly lower fuel cell performances were obtained at 600 °C, while a dramatic drop in the current density was observed at 500 °C.

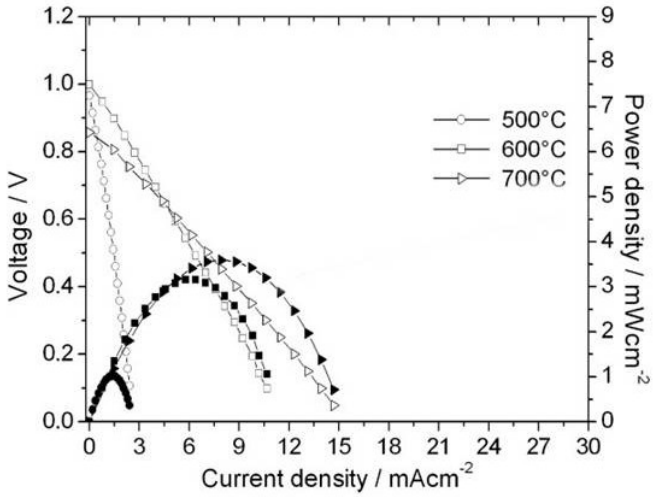

Figure 1.10: Cell voltage and power density vs. current density of Pt/BZY(1 mm)/Pt cell under humidified H_2/air conditions at 500, 600 and 700 °C.

To investigate the effect of the electrolyte thickness on cell performance, a fuel cell with a BZY electrolyte of 0.6 mm in thickness was fabricated. Platinum paste was used for both electrodes. The trend of the I–V curves, reported in figure 1.11, was similar to the one shown in figure 1.10 for a BZY electrolyte of 1.0 mm in thickness. However, larger values of power density were reached for the thinner electrolyte, with a maximum of 7.0 mW cm^{-2} at 700 °C.

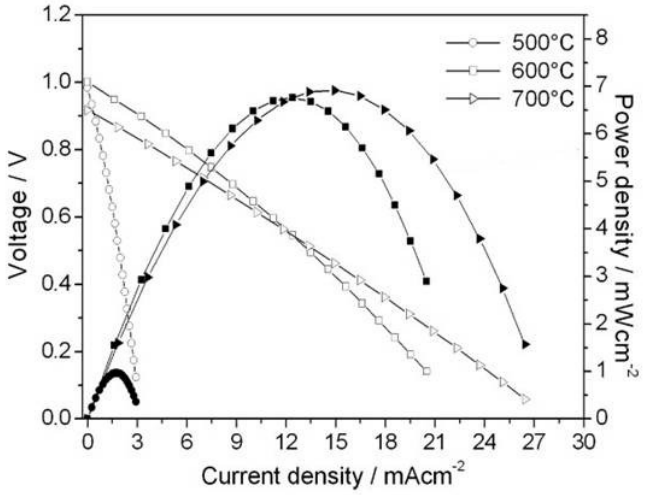

Figure 1.11: Cell voltage and power density vs. current density of Pt/BZY(0.6 mm)/Pt cell under humidified H_2/air conditions at 500, 600 and 700 °C.

These results confirm that the fabrication of dense thin film is mandatory for the development of IT SOFC with suitable performance for practical applications.

1.6 References

1. K.D.Kreuer, *Annu. Rev. Mater. Res.*, 33 (2003) 333.
2. M. Liu, D. Wang, *J. Mater. Res.* 10 (1995) 3210.
3. A. L. Quinelato, E. Longo, E. R. Leite, M. I. B. Bernardi, J. A. Varela, *J. Mater. Sci.*, 36 (2001) 3825.
4. M. Arima, M. Kakihana, Y. Nakamura, M. Yashima, M. Yoshimura, *J. Am. Ceram. Soc.*, 11 (1996) 2487.
5. J. Muller, K.D. Kreuer, J. Maier, S. Matsuo, M. Ishigame, *Solid State Ionics*, 97 (1997) 421.
6. T. Schneller, T. Schober, *Solid State Ionics*, 164 (2003) 131.
7. T. Schober, H.G. Bohn, *Solid State Ionics*, 127 (2000) 351.
8. B.C.H. Steele, A. Heinzel, *Nature*, 414 (2001) 345.

Chapter 2: Zr-Substituted Y-Doped Barium Cerate HTPC Electrolytes

2.1 Introduction

In Chapter 1.3 (Part B)It has been previously verified that BZY is actually a stable proton conductor electrolyte in the presence of CO_2 gas. However, even producing BZY powder with high purity and homogeneity down to the nanometric scale, the observed electrical performance was too poor, precluding its practical application. In fact, in the whole tested IT range, BZY does not reach the minimum target value for a 15 μm thick electrolyte materials fixed at 10^{-2} S/cm.[1]

A solid solution between barium cerate and barium zirconate oxides, properly doped, could comprise the desired characteristic of those two electrolytes, namely the good proton conductivity of the cerate and the chemical stability of the zirconate.

The complete solubility between barium cerate and barium zirconate has been previously demonstrated [2] even though they are not isostructural at room temperature, being orthorhombic [3,4] and cubic,[5] respectively.

Using the optimized sol-gel process, described in detailed in Chapter1 (Part B), Zr-substituted Y-doped barium cerate $BaCe_{0.8-x}Zr_xY_{0.2}O_{3-\delta}$ (BCZ_xY, with $0.0 \leq x \leq 0.8$) compounds were synthesized at relatively low calcination temperatures. Their structure was analyzed by X-ray diffraction (XRD), their chemical stability was investigated exposing sintered pellets to CO_2 atmosphere at 900°C for 3 h, and their electrical performance of BCZ_xY electrolytes was investigated in terms of electrical conductivity, polarization curves and power output density.

2.2 X-Ray Diffraction and Microstructure Analysis

The synthesized BCZ_xY ($0.0 \leq x \leq 0.8$)), powders were calcined for 5 h with a heating rate of 5 °C/min. The lowest calcination temperature needed to achieve a single crystalline phase formation was a function of stoichiometry. In particular the temperature was 1000 °C for x=0.0, 1200 °C for x=0.3 and x=0.5, and 1100 °C for x=0.8.

To obtain dense samples, the calcined powders were uniaxially pressed into cylindrical pellets (13 mm in diameter) at 250 MPa for 10 min and then sintered in air. Also in this case, the sintering temperature was changed depending on x (Zr content), to identify the lowest which allowed a suitable density of the pellets. Sintering was carried out for 8 h with a heating rate of 5 °C/min at temperatures of 1500 °C for x=0.0, 1550 °C for x=0.3 and 0.5 and 1600 °C for x=0.8. The microstructural features of sintered pellets were investigated using a field emission scanning electron microscope (FE-SEM). The density of the ceramic pellets was measured using a pycnometer.

Figure 2.1 shows the X-ray diffraction patterns of the calcined BCZ_xY powders with Zr content set at x=0.0, 0.3, 0.5, and 0.8. The XRD analysis of the calcined powders showed that only the target perovskite peaks were present. Very similar XRD plots were measured for the sintered pellets. The lattice symmetry of BCZ_xY compounds was found to be cubic for the sample with x=0.8, orthorhombic for x=0.3 and 0.5, and mainly monoclinic [6] for x=0.0.

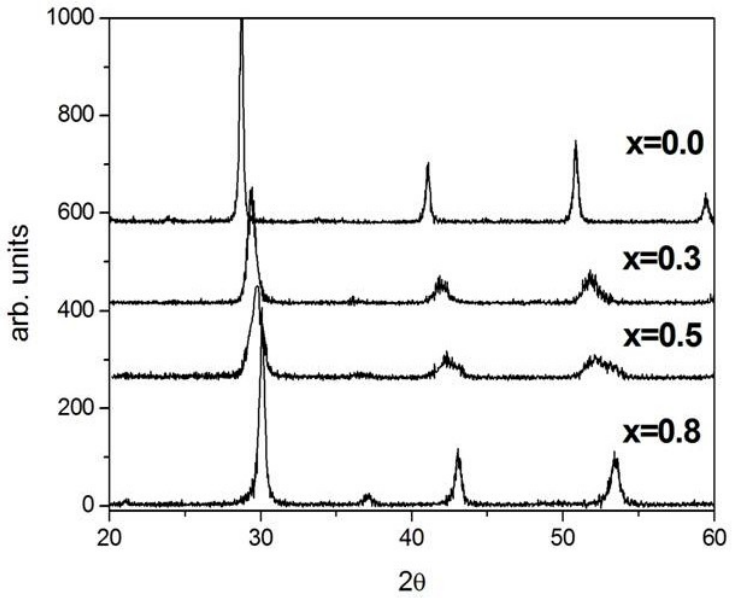

Figure 2.1: XRD patterns of $BaCe_{0.8-x}Zr_xY_{0.2}O_{3-\delta}$ oxides with different Zr content (x).

From the measured XRD plots, the lattice parameters and the unit cell volume of the sintered pellets were estimated. Table 2.1 summarizes the obtained values. The lattice parameters and the unit

cell volume values suggested that the introduction of Zr into Y-doped barium cerate electrolyte effectively changed the cell structure, in particular it decreased the lattice parameters and, therefore, the unit cell volume. This finding was somehow expected since Zr^{4+}presents a smaller ionic radius with respect to Ce^{4+} (0.72 Å and 0.87 Å, respectively).[7].The calculated lattice parameters are consistent with other published data.[6,8–11]

Zr-content	Lattice Parameters [Å]			Unit Cell Volume [Å ^{3}]
X	**A**	**B**	**C**	**V**
0.0	6.248	8.763	6.232	339.75
0.3	6.109	8.602	6.145	305.51
0.5	5.972	8.497	6.005	304.73
0.8	4.217	4.217	4.217	74.42

Table 2.1. Lattice Parameters [Å] and Unit Cell Volume [Å ^{3}] of sintered $BaCe_{0.8-x}Zr_xY_{0.2}O_{3-\delta}$

Figure 2.2 shows the FE-SEM images of the BCZ_xY sintered pellets. After sintering, the samples showed a dense structure, even though different grain sizes were observed. The sintered compound with x=0.0 (Y-doped barium cerate) showed a uniform morphology and the largest granulometry (3-10 µm grain size). The samples with x=0.5 and x=0.3 exhibited grain size of 1-5 and 2-8 µm, respectively. Finally, the pellets with x=0.8 (Y-doped barium zirconate) showed some micron-sized grains together with smaller grains (100-300 nm). The results suggest that the grain growth decreases with increasing Zr content in the BCZ_xY oxides. Also the density resulted affected by Zr content, decreasing from about 93% of the theoretical density for x=0.0, to 80% for x=0.8.

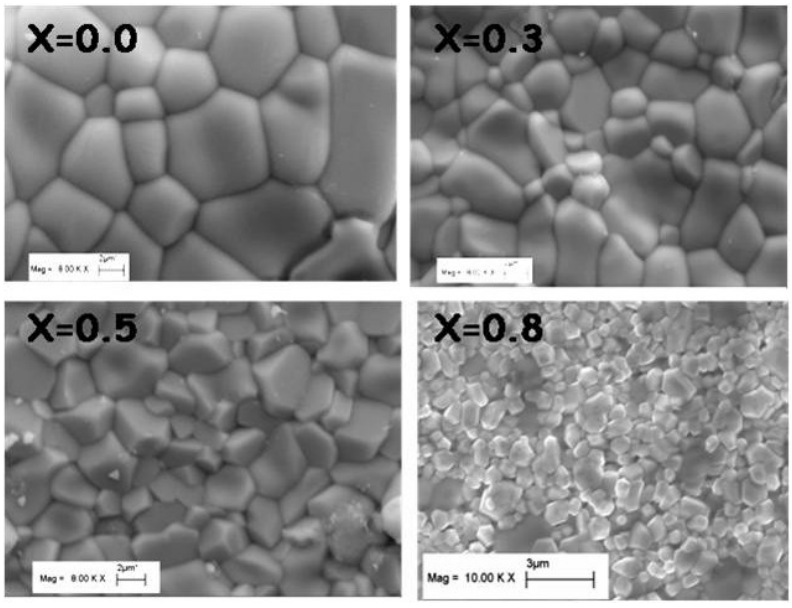

Figure2.2: FE-SEM images of sintered $BaCe_{0.8-x}Zr_xY_{0.2}O_{3-\delta}$ pellets.

2.3 Chemical Stability in CO_2

The chemical stability of the BCZ_xY sintered pellets was tested flowing pure CO_2 at 900 °C for 3 h. The phase composition of the samples after CO_2 exposure was investigated by XRD analysis.

Figure 2.3 shows the XRD patterns of the BCZ_xY pellets after CO_2 thermal treatment. As previously observed for Y-doped barium cerate (x=0.0), an extensive decomposition into $BaCO_3$ and CeO_2 was also observed for the sample with x=0.3. Only a small amount of $BaCO_3$ was observed for the sample with x=0.5 after CO_2 exposure. These results indicate that zirconium addition into barium cerates definitely improves the chemical stability of that compound.

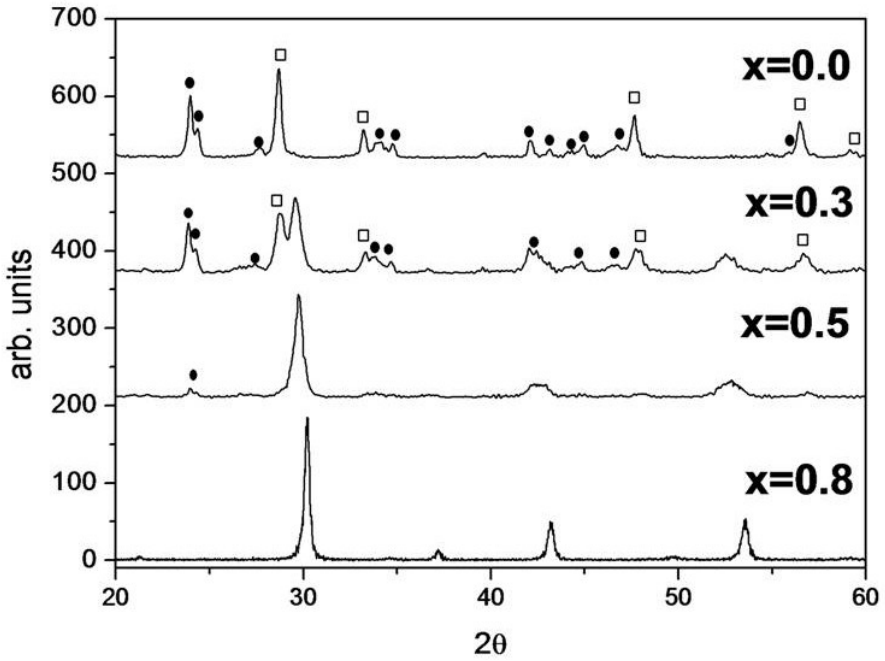

Figure 2.3: XRD patterns of sintered $BaCe_{0.8-x}Zr_xY_{0.2}O_{3-\delta}$ pellets after exposure to CO_2. Circles and squares indicate $BaCO_3$ and CeO_2 peaks, respectively.

2.4 Electrical Conductivity

The electrical conductivity of the BCZ_xY electrolytes was measured using electrochemical impedance spectroscopy (EIS) method, with a Multichannel Potentiostat VMP3, over the 500 kHz-10 mHz frequency range. Symmetrical cells were fabricated depositing porous platinum paste as electrodes on both sides of the pellets, after polishing. Conductivity measurements were performed in wet (0.03 atm p_{H_2O}) hydrogen atmosphere and dry air, between 350 and 750°C.

Figure 2.4 shows the Arrhenius plots of the BCZ_xY proton conductors in wet H_2. The introduction of Zr into barium cerate clearly resulted in a reduction of the conductivity in the whole tested temperature range. At 700°C the highest conductivity value was measured for the compound with x=0.0 at $1.47x10^{-2}$ Scm^{-1}. A very close conductivity value ($1.14x10^{-2}$ Scm^{-1}) at 700°C was recorded for the electrolyte with x=0.3, decreasing down to $7.10x10^{-3}$ Scm^{-1} for x=0.5 and $5.68x10^{-3}$ Scm^{-1} for x=0.8. The trend of conductivity values with respect to Zr content (x) is consistent with the SEM analysis that showed a decreasing grain size with increasing Zr content. A smaller grain size leads in fact to larger grain boundary regions, which are highly resistive for proton migration.

The activation energy (Ea) values were calculated for temperatures below 700°C since above 700°C a weaker conductivity temperature dependence is observed as results of two concomitant events: samples dehydration, which results in a decreased proton concentration, and enhanced proton mobility.[12] It was found that Ea for proton transport increased from 0.39 eV for the sample with x=0.0 to 0.61 eV for the sample with x=0.8. A similar trend of increasing Ea with increasing the Zr content has been already reported in the literature.[13].

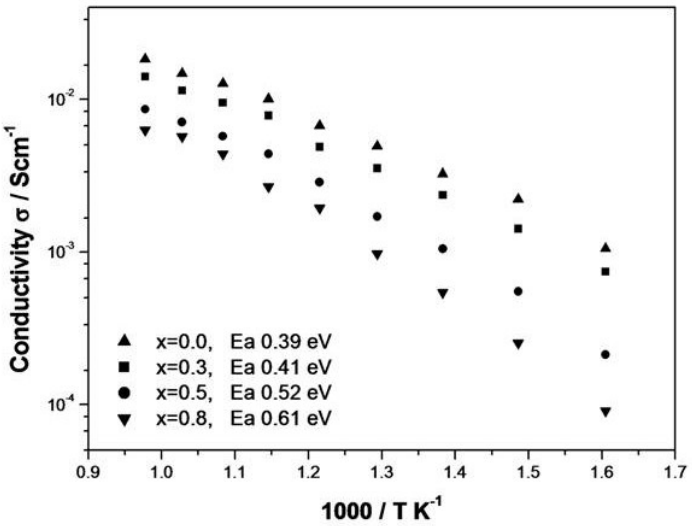

Figure 2.4: $BaCe_{0.8-x}Zr_xY_{0.2}O_{3-\delta}$ total electrical conductivity in wet H_2 as a function of temperature.

Figure 2.5 shows the total electrical conductivity in dry air as a function of temperature. For all the studied oxides, the conductivity values and the activation energies in dry air were larger than the values measured in wet H_2 atmosphere. This result can be explained by the change in the HTCP conduction mechanism in dry conditions with respect to wet conditions. In particular, in dry air a mixed oxygen-ion/electron-hole conductivity is expected. The comparison between the measured Ea values and the literature data [8,12,15,16]. indicates that the conductivity values reported in Fig. 2.5 should be associated to a mixed oxygen-ion/electronic (p-type) conduction mechanism.

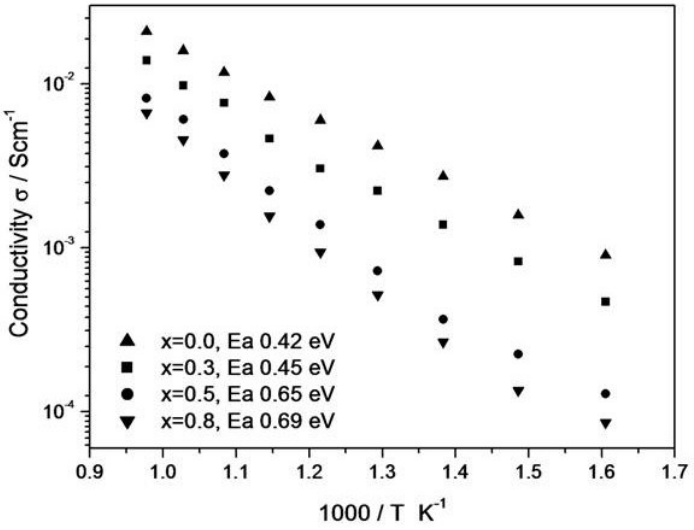

Figure 2.5: $BaCe_{0.8-x}Zr_xY_{0.2}O_{3-\delta}$ total electrical conductivity in dry air as a function of temperature.

2.5 Dual Chamber Fuel Cell Tests

Hydrogen-air fuel cell experiments were carried out at 700°C. Single cells were prepared with 0.6 mm thick BCZ_xY electrolytes. Both anode and cathode were made of Pt using the same preparation described for EIS measurements. During fuel cell operation, the anode surface was exposed to wet hydrogen (3 vol. % H_2O) and the cathode to ambient air. The electrochemical measurements were performed with a Multichannel Potentiostat VMP3.

Figure 2.6 shows the I-V curves of Pt/BCZ_xY /Pt single cells, measured in wet hydrogen-air fuel cell experiments at 700°C.

An open circuit voltage (OCV) above 1.0 V was obtained for the sample with Zr content (x) set at 0.5, 0.3, and 0.0, suggesting that no gas leakages were present in these electrolytes. Differently, the sample with x=0.8 presented a lower OCV, probably due to the lower density obtained with this composition.

Figure 2.6 also shows the power density output obtained from the BCZ_xY electrolytes. The relatively low values for the power density output are the consequence of the use of relatively thick solid electrolyte elements, approximately 0.6 mm. The power output decreased increasing Zr content (x) in the electrolyte composition. In particular, the maximum power density was recorded using the electrolyte with x=0.0 composition, reaching about 58 $mWcm^{-2}$. Close fuel cell performance was observed for the sample with x=0.3, with a peak power density of 46.5 $mWcm^{-2}$. Increasing Zr content the power output decreased to 18 $mWcm^{-2}$ for the sample with x=05, and to only 7 $mWcm^{-2}$ for the x=0.8 electrolyte. However, as shown from the previously described chemical stability tests, only the two latter electrolytes presents suitable chemical stability for use in practical IT-SOFC application.

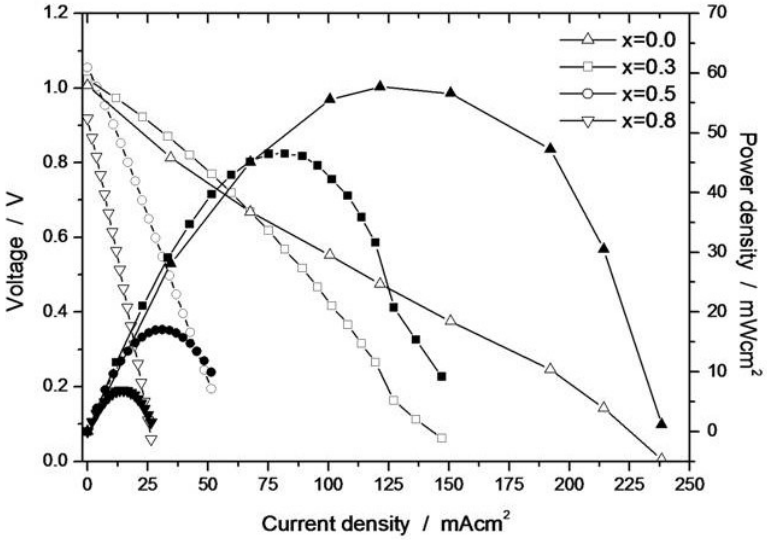

Figure 2.6: I-V curves and power density output of Pt/ $BaCe_{0.8-x}Zr_xY_{0.2}O_{3-\delta}$/Pt single cells measured at 700°C in wet hydrogen-air fuel cell experiments.

2.6 Overpotential Analysis

The difference in conductivity values between samples with different Zr content (fig. 2.4) is not enough to justify the significant decrease in the power density output observed for the electrolytes with the highest Zr content (fig. 2.6). Therefore, the electrode/electrolyte interface resistance should differently contribute to the total cell area specific resistance (ASR) depending on the electrolyte composition.

To investigate the electrode/electrolyte interface resistance, EIS measurements were used to determine the ASR values of the Pt/BCZ_xY interfaces in wet hydrogen (anode condition) and ambient air (cathode condition). A typical complex impedance plane plot in wet H_2 (figure 2.7) showed one depressed semicircle in the low frequency range for the sample without Zr (x=0.0). Differently, in the case of the compositions with x=0.3, 0.5, and 0.8, two depressed semicircles could be observed in the low frequency range. In ambient air atmosphere the complex impedance plane plots presented only one semicircle at low frequency for every electrolyte composition.

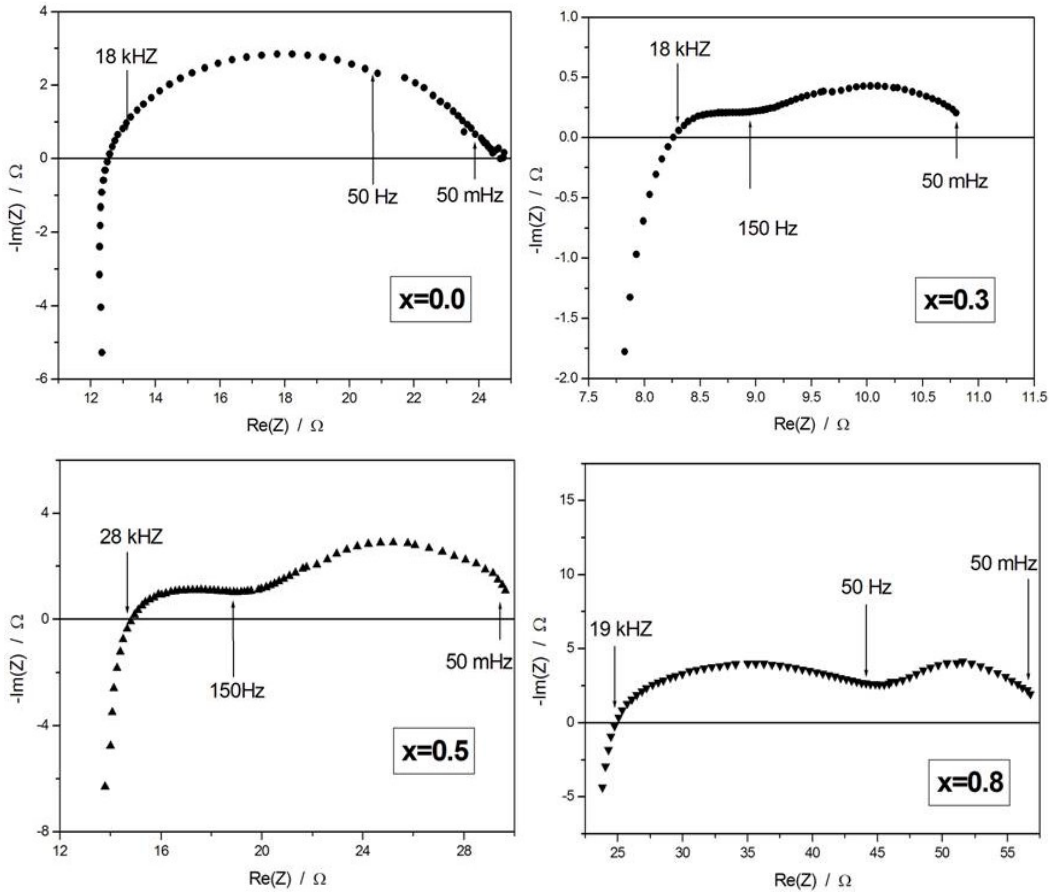

Figure 2.7: EIS plots in the complex impedance plane of Pt/ $BaCe_{0.8-x}Zr_xY_{0.2}O_{3-\delta}$/Pt symmetric cells at 550°C in wet hydrogen.

Interestingly, when two semicircles were present in the low frequency range of the complex impedance plane plots (figure 2.8), the first one (between 18-20 kHz and 150-50 Hz) showed a larger diameter increasing the Zr content in the electrolytes. Therefore, the electrode process associated to the first semicircle at the higher frequencies, which is generally related to the charge transfer process, presented an increasing resistance with increasing Zr content.

Pt/electrolyte interface ASR was calculated as ASR=(Rp*A)/2, where A is the geometrical electrode area divided by two, because of the use of symmetrical cells, and Rp is the electrode resistance calculated as the difference between the high frequency and low frequency intercepts of the impedance plane plot with the real axis. Where two depressed semicircles are present in the impedance plane plot, the electrode resistance (Rp) was calculated as the sum of both low frequency arc resistances Figure 2.8 shows the ASR of the Pt electrodes in wet H_2 (3 vol. % H_2O) and dry air. The Pt electrodes, in both environments, showed an increasing ASR when applied over electrolytes with increasing Zr content. This is something not surprising since problems at the Pt interface with barium zirconate electrolyte (x=0.8) have already been reported in literature due to weak sticking of the Pt layer to the electrolyte and thermal expansion mismatch.[17].

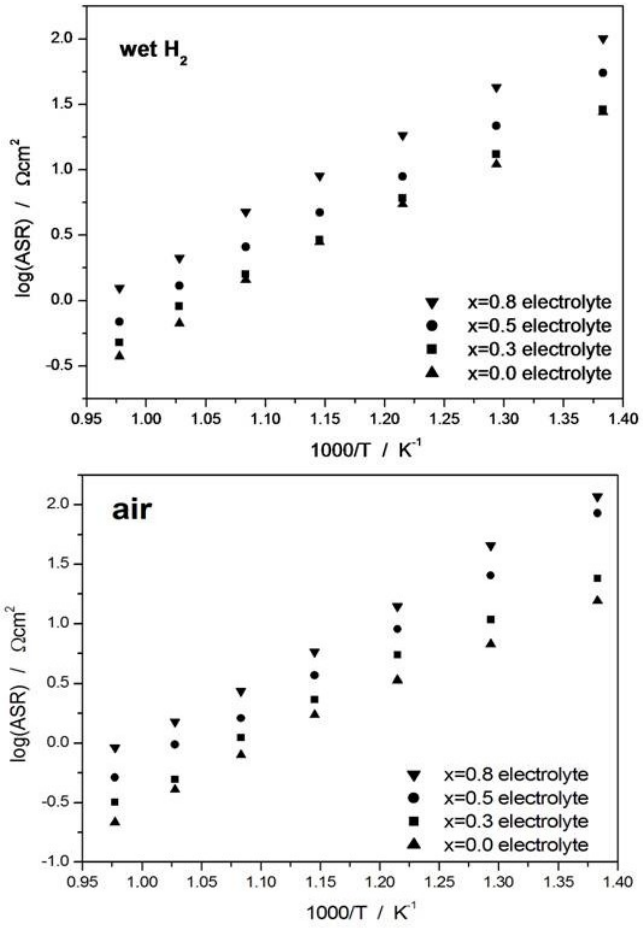

Figure 2.8: Temperature ASR dependence of Pt electrodes applied over electrolytes with different Zr content (x) in wet hydrogen and in dry air.

To evaluate the electrode and electrolyte polarization contributions to the whole cell overpotential during fuel cell operation, EIS measurements were performed in-situ during fuel cell tests. Figure 2.9 shows the complex impedance plane plots of the Pt/BCZ_xY/Pt cells measured at 700°C under open-circuit conditions. The ohmic electrolyte resistances (R_{ohmic}), measured as the high frequency intercept with the real axe in the complex impedance plane plot, increased with increasing the Zr content in the electrolyte composition according with the electrical conductivity measurements (fig. 2.4 and fig. 2.5) A more detailed analysis of the impedance in the Nyquist plot in figure 2.9 indicates that the overall fuel cell performance of the Pt/BCZ_xY/Pt cells was strongly affected by the Pt electrode polarization. In fact, for each composition, the electrolyte resistance was smaller than the electrode reaction resistance, being the difference larger with increasing Zr content.

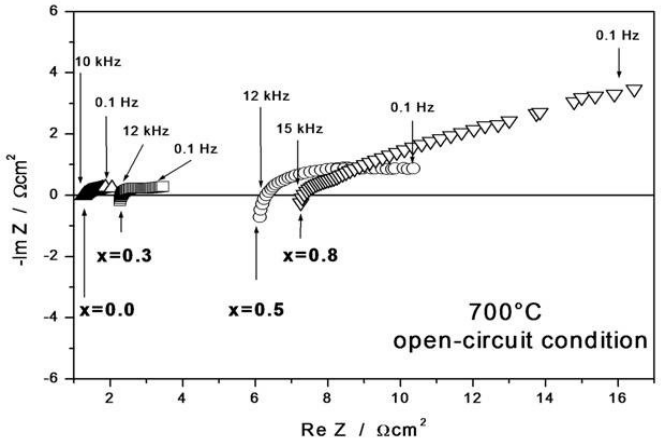

Figure 2.9: Complex impedance plane plot of Pt/BCZ_xY/ cells with different electrolyte composition at 700°C under open circuit conditions.

A comprehensive picture of the electrical characterization of the Pt/BCZ_xY/Pt cells is displayed in figure 2.10, which shows the histogram of the electrolyte resistance and electrode polarization resistance at 700°C.

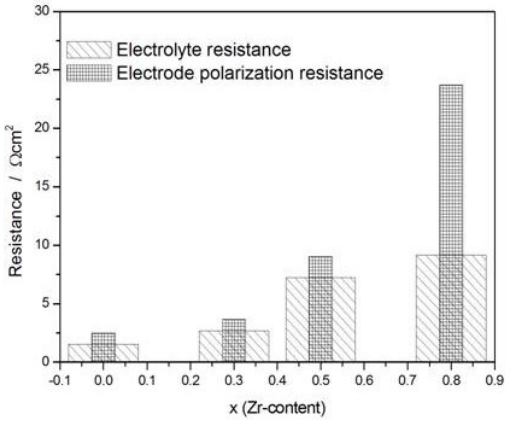

Figure 2.10: Histogram of the electrolyte resistance and electrode polarization resistance for the Pt/BCZ_xY/ cells with different electrolyte composition at 700°C.

The ohmic (iR) losses, mainly due to the electrolyte, were estimated as the product between R_{ohmic} and the current density measured during fuel cell tests. The iR polarizations for the different electrolyte compositions are showed in figure 2.10 (filled symbols). Figure 2.10 shows also the electrode overpotential (η_p) which is given by the modulus of the difference between the total polarization (open symbols) and the iR polarization, taken at the same current density.

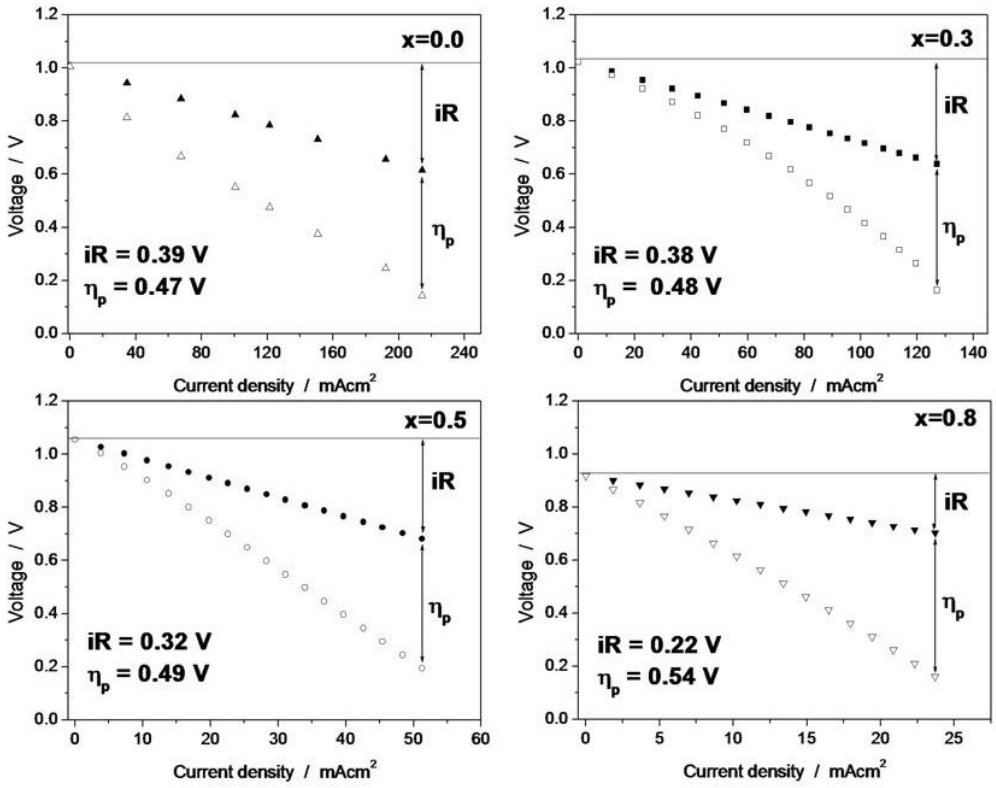

Figure 2.11: I-V curves (open symbols), iR losses (filled symbol), and the electrode polarization (η_p) for the Pt/BCZ$_x$Y/ cells with different electrolyte composition at 700°C.

According to the measured ASR values for the Pt/BCZ$_x$Y electrolyte interfaces (Fig. 2.8), figure 2.11 shows that increasing the Zr contents in the electrolyte composition, the electrode overpotential drop became significantly larger than the ohmic resistance.

Figure 2.12 shows the ratio t=iR/η_p, taken when the cell discharge reaches 0.2 V, which better highlights the ohmic and electrode polarization contribution to the total cell voltage loss. The larger the Zr contents in the electrolyte composition, the larger the contribution of the electrode polarization resistance to the total cell overpotential.

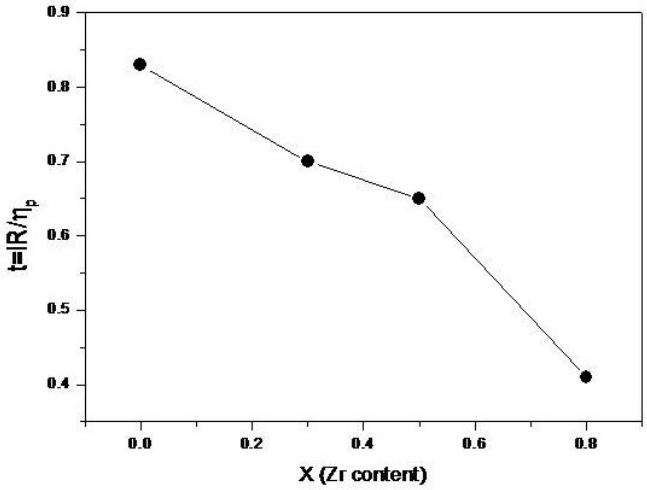

Figure 2.12: Values of the ratio $t=iR/\eta_p$ for different Zr content (x).

2.7 Single Chamber Fuel Cell Tests

The fuel cell performance of the $BaCe_{0.3}Zr_{0.5}Y_{0.2}O_{3-\delta}$ electrolyte was tested in single chamber mode where hydrocarbon fuels are used and thus CO_2 is actually produced.

Single chamber fuel cells are a type of fuel cell wherein both anode and cathode are exposed to the same mixture of fuel and oxidant gas. Generally, hydrocarbons such as methane or propane are used as fuel. The great advantage of these cells is that, since air and fuel can be mixed, sealing in not required. Furthermore, the mechanical and thermal stress resistance of the cell can be enhanced due to the simplified structure. Finally, they allows for a more compact stack design, due to the reduced quantities of stack components.[18,19]

The performance of single chamber SOFCs is mainly influenced by the electrode selectivity towards the gas mixture. The ideal anode should catalyze the partial oxidation of hydrocarbon fuel to syngas (H_2 and CO) as well as catalyze the electro-oxidation of these products. The ideal cathode should be inert towards hydrocarbon fuels and catalyze the electro-reduction of oxygen gases.[19] In many cases, Ni-based and perovskite type oxide electrode are used as anode and cathode, respectively.

$BaCe_{0.3}Zr_{0.5}Y_{0.2}O_{3-\delta}$ electrolyte supported single chamber fuel cells were fabricating using Ni (Aldrich, 99.9%) as anode and $Ba_{0.5}Sr_{0.5}Co_{0.8}Fe_{0.2}O_{3-\delta}$ (BSCF) as cathode. An additional porous layer of Ru (Aldrich, 99.99%) was coated onto the anode surface to enhance the catalysis of fuel partial oxidation at low temperature. The $BaCe_{0.3}Zr_{0.5}Y_{0.2}O_{3-\delta}$ pellet was prepared as previously described. For electrode coating on the $BaCe_{0.3}Zr_{0.5}Y_{0.2}O_{3-\delta}$ electrolyte, different electrode inks were prepared mixing the electrode powders with an organic vehicle (α-terpineol as a solvent, di-n-butyl phthalate as a plasticizer, and polyvinylbutiral as a binder) until an appropriate viscosity for brushing was achieved. The electrode pastes were dried at 150°C for 3 h and then sintered at 800°C for 2h. Pt and Au wires current collectors were used for the anode and cathode, respectively. Two different single chamber fuel cell configurations were tested. The finger configuration (figure 2.13A) was obtained brushing the electrode inks on the same face of the electrolyte. For the sandwich configuration (figure 2.13B) the electrode pastes were applied on the opposite faces of the electrolyte. For both the configurations, a 1 mm thick electrolyte was used. In the finger configuration the electrode distance was 1 mm. The cell was placed in an alumina tube which was heated up to 500°C. A mixture of propane, oxygen, and helium having the composition of 40sccm C_3H_8+90-60sccm O_2+360sccm, was supplied to the cell.

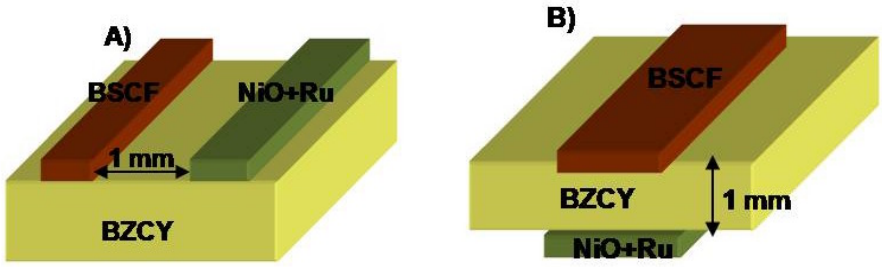

Figure 2.13: single chamber fuel cell configurations: finger (A) and sandwich (B).

The discharge property of the two single chamber configurations was measured under different conditions. The 40sccm C_3H_8+90sccm O_2+360sccm gas mixture composition represents the most fuel lean condition explored, while the 40sccm C_3H_8+60sccm O_2+360sccm the most fuel rich. Figure 2.14 and 2.15 show the variation of the open circuit voltage (OCV) and power density output with the gas flow composition, respectively.

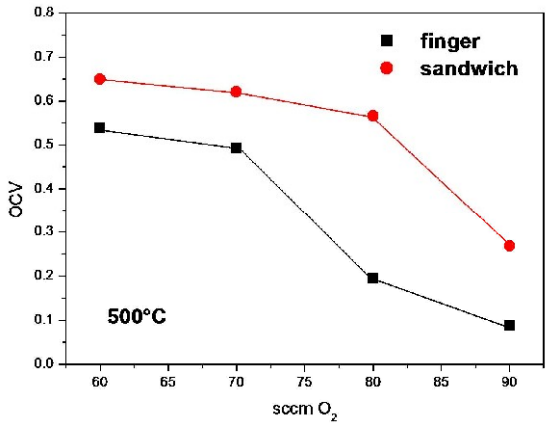

Figure 2.14: OCV dependence on oxygen flow rate for finger and sandwich configuration at 500°C.

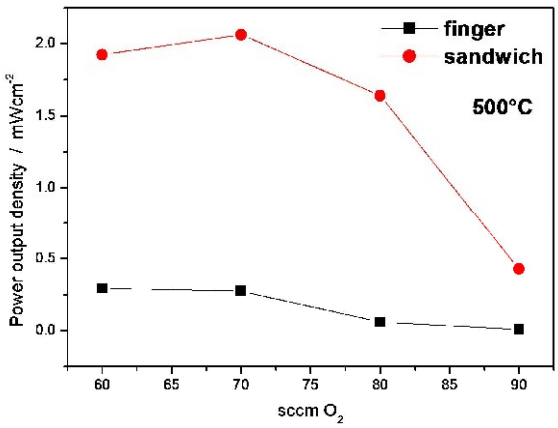

Figure 2.15: Power output density dependence on oxygen flow rate for finger and sandwich configuration at 500°C.

Both finger and sandwich configurations showed a decreasing OCV increasing the oxygen flow rate. The highest OCV of 0.67 mV was observed for the sandwich configuration at the O_2 flow rate of 60sccm. The max power density was observed with 70sccm of O_2 flow rate for sandwich configuration. Increasing oxygen flow rate a sharp drop in power output was observed for such configuration. In the case of finger configuration the power output was less influence by the oxygen flow rate, showing a marked decreasing only when O_2 flow rate increased from 70 to 80sccm.

For a complete oxidation of the fuel (Equ.2) a propane to oxygen ratio of 1:5 is required, whereas the ideal ratio for partial oxidation (Equ.3) is 2:3.

$$C_3H_8 + 5O_2 \leftrightarrow 3CO_2 + 4H_2O \tag{2}$$

$$2C_3H_8 + 3O_2 \leftrightarrow 6CO + 2H_2 \tag{3}$$

The gas mixture of 40sccm C_3H_8+90sccm O_2+360sccm presents the closest fuel/oxygen ratio to that required for complete fuel oxidation. The fuel/oxygen ratio associated to the most fuel rich gas mixture (60sccm O_2) is the same required for partial oxidation. Therefore, from figure 2.14 appears the OCV is maximum when the propane/oxygen ratio coincides with the reactant gas composition that yields to partial oxidation, that is the highest concentration of partial oxidation products (H_2 and CO_2). The power output density presented a different fuel/oxygen ratio dependence. In particular it reached the higher values in between the most fuel lean and fuel rich gas composition. This finding is consistent with other literature data. [19,20]

Figure 2.16 compare the discharge properties of the finger and sandwich configuration cell at 500°C, flowing a gas mixture of 40sccm C_3H_8+60sccm O_2+360sccm.

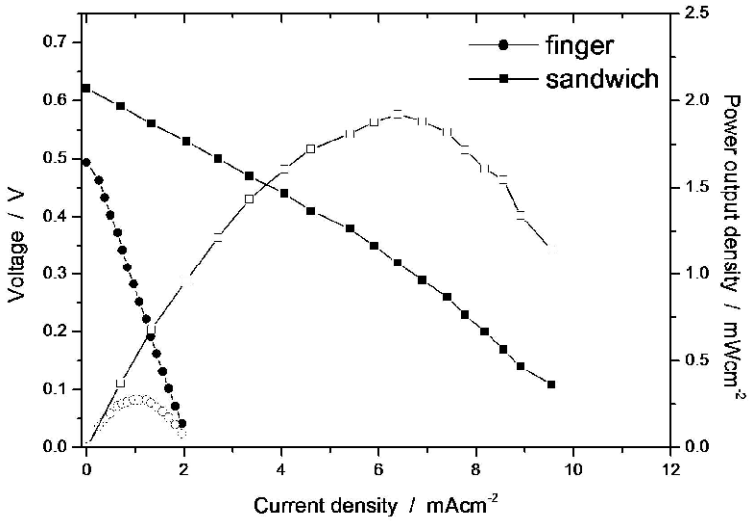

Figure 2.16: I-V curve dependence on oxygen flow rate for finger and sandwich configuration at 500°C.

The sandwich cell showed higher OCV, short circuit current density and power density output than the finger configuration cell. In particular, the most marked difference in the discharge properties of the two cell configurations is related to the short circuit current density and power density. As shown in figure 2.13A, in finger configuration the gap between the two electrodes means the shortest conduction path for proton ion between them (1 mm). Each electrode was about 1 mm wide, and thus the longest conduction path of protons between the two electrode was 3 (=1+1+1) mm. This fact can explain the lower short circuit current density of the cell with finger configuration with respect to the one with sandwich configuration.

2.8 Conclusions

Using a sol-gel synthesis route, single-phase powders of $BaCe_{0.8-x}Zr_xY_{0.2}O_{3-\delta}$ (BCZ_xY) proton conductors over the $0.0 \leq x \leq 0.8$ composition range were obtained at low processing temperatures for the preparation of solid electrolytes.

The chemical stability of the electrolyte under fuel cell operating conditions is an essential requirement for practical applications, and thus the chemical stability of BCZ_xY electrolytes under CO_2 atmosphere has been tested. The strong degradation of Y-doped barium cerate electrolyte and also of the electrolyte with 0.3 content of Zr in CO_2 environment makes them unsuitable for application in fuel cell. Differently, Y-doped barium zirconate and $BaCe_{0.3}Zr_{0.5}Y_{0.2}O_{3-\delta}$ electrolytes present a good chemical stability.

Hydrogen-air fuel cell tests showed that the power output obtained from the $BaCe_{0.3}Zr_{0.5}Y_{0.2}O_{3-\delta}$ based cell was more than twice higher with respect to Y-doped barium zirconate, without impairing the chemical stability. The improvement in fuel cell performance was obtained both by increasing the proton conductivity and reducing the electrode polarization. Thus, the $BaCe_{0.3}Zr_{0.5}Y_{0.2}O_{3-\delta}$ electrolyte seems to be a good compromise between fuel cell performance and chemical stability for IT-SOFCs applications. However, the current densities achieved so far are too small for practical applications. On one hand, this is due to the fact that we used electrolyte pellets as supporting structure. The current densities could be increased by fabricating dense electrolyte films on supporting anodes. On the other hand, the selection of suitable electrode materials is paramount for increasing fuel cell power output. Pt severely affected the fuel cell performance, showing high electrode polarization especially increasing the Zr content in the electrolyte composition.

$BaCe_{0.3}Zr_{0.5}Y_{0.2}O_{3-\delta}$ electrolyte was also tested in single chamber fuel cell tests with a feed gas mixture of propane, oxygen and helium.

2.9 References

1. D.J.L. Brett, A. Atkinson, N.P. Brandon, S.J. Skinner, *Chem. Soc. Rev*., 37 (2008) 1568.
2. I. Charrier-Cougoulic, T. Pagnier and G. Lucazeau, *Solid State Chem.* 142 (1999) 220.
3. K.S . Knight, *Solid State Ionics*, 74 (1994) 109.
4. F. Genet, S. Loridant, C. Ritter, G. Lucazeau, *J. Phys. Chem. Sol,*. 60 (1999) 2009.
5. M.D. Mathews, E.B. Mizra, A.C. Momin, *J. Mater. Sci. Lett,*. 10 (1991) 305.
6. Takeuchi, C.K. Loong, J.W. Richardson Jr., J. Guan, S.E. Dorris, U. Balachandran, *Solid State Ionics*, 138 (2000) 63.
7. R.D. Shannon, *Acta Cryst*., A32 (1976) 751.
8. K. Katahira, Y. Kohchi, T. Shimura, H. Iwahara, *Solid State Ionics*, 138 (2000) 91.
9. X. Ma, J. Dai, H. Zhang, D.E. Reisner, *Surface and Coatings Technology*, 200 (2005) 1252.
10. T. Schober, H.G. Bohn, *Solid State Ionics*, 127 (2000) 351.
11. A. Magrez, T. Schober, *Solid State Ionics*, 175 (2004) 585.
12. H.G. Bohn, T. Schober, J. Am. Ceram. Soc. 83 (2000) 768-772.
13. K.H. Ryu, S.M. Haile, *Solid State Ionics*, 125 (1999) 355.
14. A. Mitsui, M. Miyayama, H. Yanagida, *Solid State Ionics*, 22 (1987) 213.
15. W. Wang, A.V. Virkar, *J. Power Sources*, 142 (2005) 1.
16. K. Nomura, H. Kageyama, *Solid State Ionics*, 178 (2007) 661.
17. J.M. Serra, W.A. Meulenberg, *J. of Am. Ceram. Soc*., 90 [7] (2007) 2082.
18. M. Yano, A. Tomita, M. Sano, T. Hibino, *Solid State Ionics*, 177 (2007) 3351.
19. Z. Shao, J. Mederos, W. C. Cheueh, S.M. Haile, *J. Power Sources*, 162 (2006) 589.
20. T. Hibino, H. Hashimoto, M. Yano, M. Suzuki, S. Yoshida, M. Sano, J. of Electroch. Soc., 149 (2002) A133.

Chapter 3: Development of a HTPC Bilayer Electrolyte

3.1 Introduction

In the previous chapter Zr substituted Y-doped barium cerate electrolytes were developed to comprise the high proton conductivity of $BaCeO_3$ based oxides and the good chemical stability of $BaZrO_3$ based oxides. The electrolyte with composition $BaCe_{0.3}Zr_{0.5}Y_{0.2}O_{3-\delta}$ presents a significantly higher chemical stability in CO_2 atmosphere than Y-doped barium cerate electrolyte, generating a power output density more than twice with respect to the chemically stable Y-doped barium zirconate electrolyte.

In the attempt of facing in a different way the challenge of the development of a highly protonic conductive and stable electrolyte, a bilayer electrolyte was realized coupling two proton conductor oxides. By means of pulsed laser deposition (PLD) a thin protecting layer of 20%Y-doped $BaZrO_3$ (BZY) was grown on one side of a thick 20%Y-doped $BaCeO_3$ (BCY) pellet. This is a simple but not yet investigated approach in the field of HTPC electrolyte.

The measured promising performance comes from the very good crystallographic matching at the interface between the two materials, as well as the microstructure properties of the protecting layer in terms of uniformity, density and filling factor.

The chemical stability of the bilayer electrolyte was tested firstly checking for a possible interdiffusion between the BCY pellet and the BZY thin layer, since in Chapter 2 (Part B) a solid solution between these two electrolytes has been produced. Then the chemical stability required for fuel cell applications was tested exposing the BZY face to CO_2 atmosphere at 900°C for 3 hours (as in the case of the Zr-substituted 20%Y-doped $BaCeO_3$ electrolytes).

The electrical conductivity of the bilayer electrolyte was investigated using electrochemical impedance spectroscopy (EIS), and hydrogen-air fuel cell tests were performed using Pt electrodes. The objective was to test its structure, chemical stability and then the electrical performance.

3.2 X-Ray Diffraction and Microstructure Analysis

PLD system was the technique chosen for the deposition of the BZY layer on the BCY substrate. PLD is a thin film deposition method where a high power pulsed laser beam is focused inside a vacuum chamber toward a target of the desired composition. The chosen material is then vaporized and deposited on an appropriate substrate in front of the target. Commonly, a background gas such as oxygen is used when depositing oxides, while the deposition substrate is kept at the suitable temperature for the film growth. In our case the deposition substrate was a 1 mm thick pellet of BCY, while the ablation target consisted on a BZY pellet. Before deposition, the face of the BCY pellet used as substrate was polished with standard size P1000 and P2500 silicon carbide grinding paper, using ethanol as lubricant. A laser fluency of about 5 Jcm^{-2}, with a repetition rate of 10 Hz, was used. The substrate temperature was 650°C, the target to substrate distance was 25 mm, while the oxygen partial pressure was set at about 10 Pa. With the described set of deposition parameters, an ablation rate of about 3 $Ås^{-1}$ was achieved and a 1 μm thick BZY coating was deposited in about 60 min.

For the preparation of the BZY target and BCY substrate pellets, the oxide powders were synthesized using the sol-gel process described in Chapter 1 (Part B). The calcined powders were pressed and then sintered at high temperature (1600 and 1500 °C, respectively) to obtain dense pellets.

Figure 3.1 shows the X-ray diffraction (XRD) patterns of the BCY and BZY target, and of the BZY-BCY bilayer electrolyte. Both the reflection lines of the BCY and BZY perovskite structures can be identified in the XRD pattern of the bilayer electrolyte.

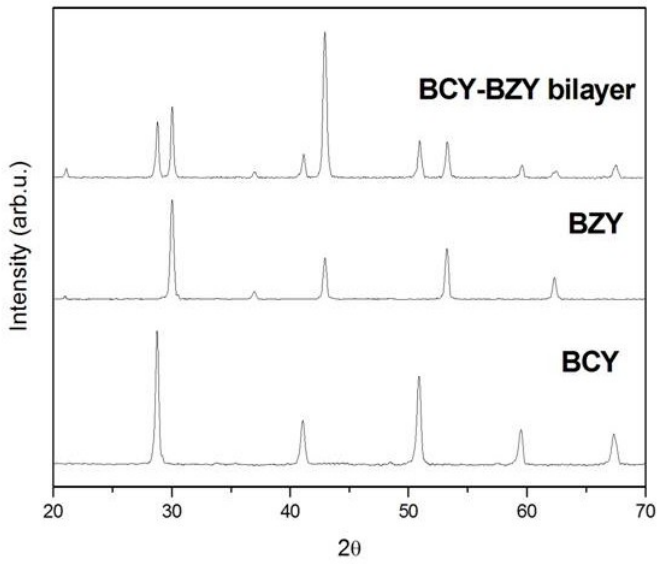

Figure 3.1: XRD patterns of the BCY and BZY targets for the fabrication of the bilayer electrolyte, and the XRD patter of the BCY-BZY bilayer electrolyte.

Figure 3.2 shows the XRD plot of the bilayer electrolyte with the indication of the Miller indices for each BZY and BCY reflection lines. The BZY reflections correspond to a cubic cell with crystal lattice parameter of about 4.21 Å, consistent with literature data.[1,2] For the identification of the crystalline reflections of the BCY substrate, the pseudo-cubic lattice of its orthorhombic perovskite structure was used, obtaining a crystal lattice constant of about 4.38 Å. The cubic lattice parameter of BZY is then very close to the BCY pseudo cubic cell parameter. Furthermore, using the BCY pseudo-cubic cell, the reflection lines of the two crystalline structures could be grouped in couples, each of them referring to the same string of Miller indices.

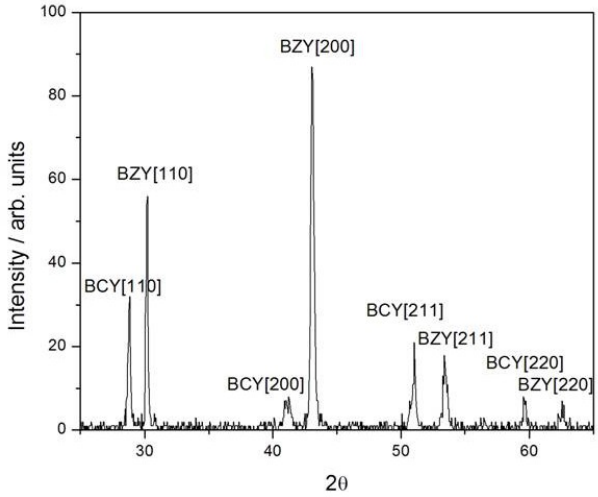

Figure 3.2: XRD patterns of the BCY-BZY bilayer electrolyte.

Figure 3.3 shows the cross-section FE-SEM micrograph of the bilayer electrolyte. The BZY thin layer was fully dense and homogeneously deposited on the BCY pellet substrate. The bilayer interface was very well defined and sharp.

Comprehensively, the SEM analysis and the interpretation XRD pattern of the bilayer give a strong indication of an epitaxial grain by grain growth of the BZY thin layer on the BCY substrate.

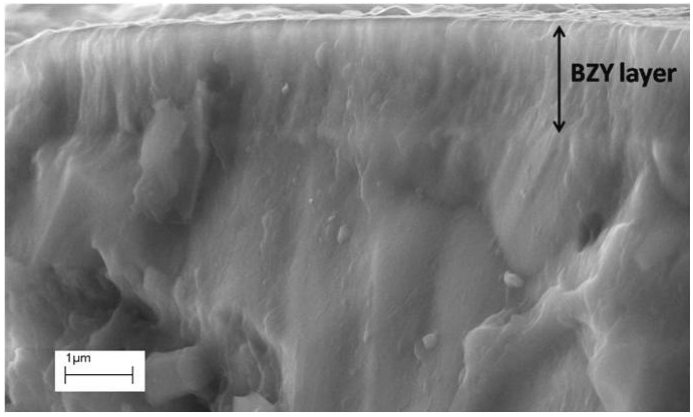

Figure 3.3: FE-SEM images of the BCY-BZY bilayer electrolyte

3.3 Chemical Stability

The chemical stability of the BCY-BZY bilayer electrolyte was tested from two different points of view. Firstly a possible interdiffusion between the BZY and BCY electrolyte was investigated since the work presented in Chapter 2 (Part B) demonstrated that these two electrolytes can form solid solutions. Then, it was verified whether the BZY layer was actually able to protect the BCY pellet against decomposition in presence of CO_2.

3.3.1 BCY and BZY Interdiffusion

To check a possible thermal interdiffusion between the BZY layer and the BCY supporting pellet, XRD analysis was used.

In the previous chapter it was demonstrated that in the XRD patterns of the BCY-BZY solid solutions the 2θ angular position of the (110) reflection line falls in the angular gap between the (110) reflection lines of BCY and BZY oxides. Referring to the XRD pattern in figure 3.4, the (110) reflections from the BZY cubic cell and the BCY pseudo-cubic cell can be identified around 2θ= 30.10° and 28.85°, respectively. The (110) reflection line of BCY-BZY solid solution compounds would fall between the above reflections, being the precise 2θ value determined by the relative content between Ce and Zr.

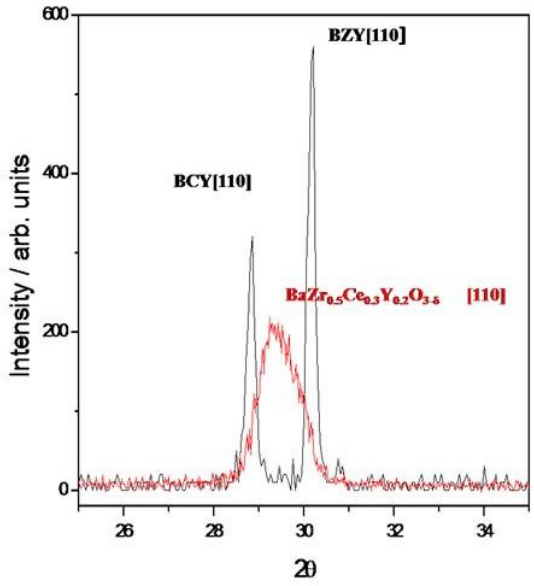

Figure 3.4: XRD patterns of BCY, BZY, and their solid solution oxides focused on the (110) reflection.

Therefore, in case of thermally-activated interdiffusion between BZY and BCY oxides, a progressive reduction in the BZY (110) reflection intensity and eventually the presence of the characteristic peaks of the solid-solution compounds would be expected in the XRD plot of the bilayer electrolyte.

To explore the possible thermally-activated interdiffusion, the bilayer was thermally treated in air and XRD analysis was performed after each thermal treatment. During the first thermal treatment the sample was kept for 3 days at 700°C. Subsequently the same bilayer sample was heated at 800, 900, 1000, and 1100°C, each temperature held for 24 hours. Figure 3.5 shows the XRD plots of the bilayer electrolyte as fabricated and after the thermal treatments. The XRD plots before and after the described severe thermal treatments show basically the same polycrystalline heterostructure, without any evident peak which could be related to the interdiffusion process. Therefore, within the limits of XRD analysis, the formation of a solid solution can be discarded even after thermal treatments up to 1100°C.

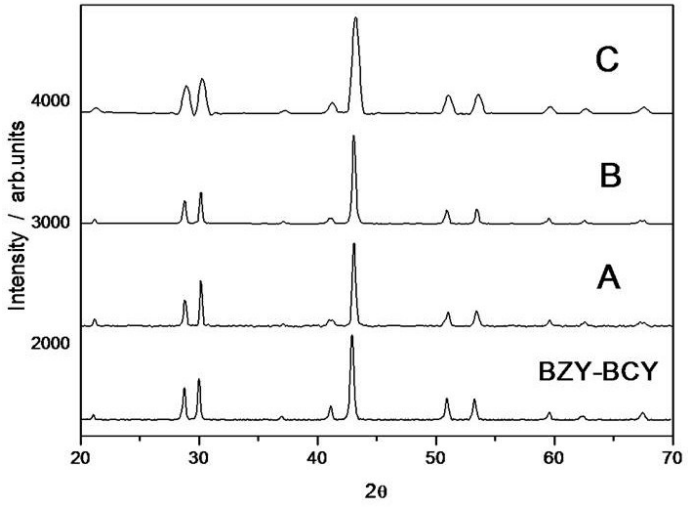

Figure 3.5: XRD plots of the BZY-BCY bilayer as fabricated, heated at 700°C for 72h (A), step A + 800°C for 24h +900°C for 24h (B), step B+ 1000°C for 24h +1100°C for 24h(C).

3.3.2 Chemical Stability in CO_2

The chemical stability in the presence of CO_2 was tested exposing the BZY-protecting layer to 100% CO_2 atmosphere at 900°C for 3 hours and investigating the treated sample by XRD analysis.

Figure 3.6 shows the XRD patterns of the bilayer electrolyte before and after the CO_2 thermal treatment. For comparison, the XRD plots of an unprotected BCY pellet, after and before the same CO_2 thermal treatment, are reported.

The BCY pellet without the thin BZY protecting layer strongly decomposed into $BaCO_3$ and CeO_2, whereas the BZY-BCY bilayer XRD pattern remained unchanged after CO_2 exposure. This result demonstrated that the BZY layer is actually able to protect the BCY electrolyte against decomposition in CO_2 atmosphere.

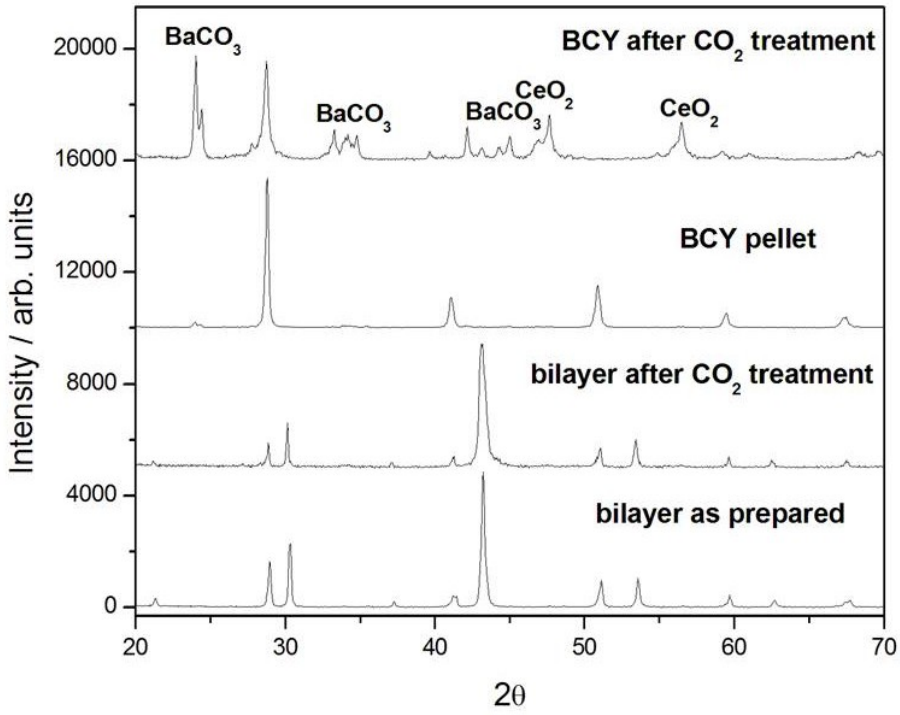

Figure 3.6: XDR patterns of BCY pellet after CO_2 treatment, BCY pellet as prepared, BZY-BCY bilayer after CO_2 treatment, and BZY-BCY bilayer as prepared.

3.4 Bilayer Electrical Conductivity

The electrical conductivity measurements of the bilayer electrolyte were performed in humidified hydrogen (~3% vol. H_2O) using electrochemical impedance spectroscopy (EIS) with a multichannel potentiostat VMP3, in the frequency range between 500 kHz and 0.1 Hz. Two symmetric Pt electrodes were deposited by applying porous platinum paste onto both sides of the samples.

Figure 3.7 shows the measured electrical conductivity of the bilayer electrolyte, together with the conductivities of BCY, BZY, and Ba $Zr_{0.5}Ce_{0.3}Y_{0.2}O_{3-\delta}$ (BZCY) pellets reported for comparison. At temperatures above 650°C the bilayer conductivity approached the values of BCY conductivity. At 700°C, for example, the electrical conductivity of the BZY-BCY bilayer was 1.25 x 10^{-2} Scm^{-1} and for the BCY was 1.47 x 10^{-2} Scm^{-1}, higher than that of the BZY pellet (5.68 x 10^{-3} Scm^{-1}) and also of the BCZY electrolyte (7.10x10^{-3} Scm^{-1}).

The activation energy for proton transport, calculated for temperatures below 700°C was larger for the BZY-BCY bilayer with respect to the BCY pellet (0.43 eV against 0.35 eV, respectively). However, the bilayer electrolyte activation energy was significantly different, being lower, in comparison with that of BZCY and BZY samples (0.52 and 0.61 eV, respectively).

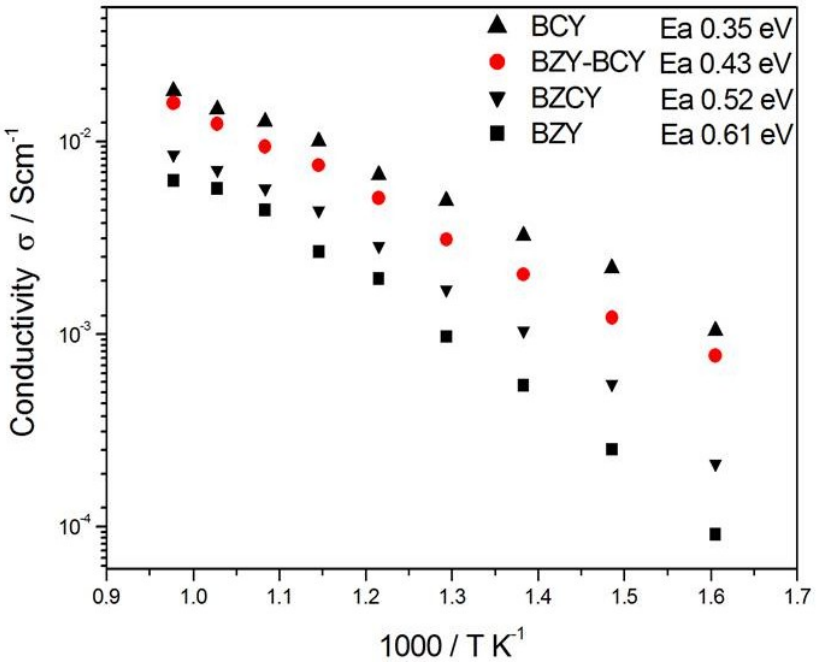

Figure 3.7: $BaCe_{0.8}Y_{0.2}O_{3-\delta}$ (BCY), bilayer electrolyte, $BaZr_{0.5}Ce_{0.3}Y_{0.2}O_{3-\delta}$ (BZCY), $BaZr_{0.8}Y_{0.2}O_{3-\delta}$ (BZY) total electrical conductivity in wet H_2 as a function of temperature.

3.5 Bilayer Fuel Cell Tests

Fuel cell tests were carried out at 700°C exposing the anode surface (BCY pellet) to wet (~3% vol. H_2O) hydrogen and the cathode (BZY protecting layer) to ambient air. Pt electrodes were used for both anode and cathode.

Figure 3.8 shows the I-V curve and the power density output from the BZY-BCY bilayer electrolyte. The fuel cell performance of single cells using BCY and BZY electrolytes of the same thickness (1 mm) and in the same condition (700°C, wet H_2/air, Pt electrodes) are reported for comparison. The open circuit voltage (OCV) was very close to 1 V for the BCY and the BZY-BCY bilayer electrolytes. This fact is in agreement with the SEM analysis that clearly showed the high density for the BCY pellets. On the other hand, as reported in Chapter 2 (Part B), the BZY pellet was more difficult to sinter and its density was slightly smaller, this resulting in a lower OCV.

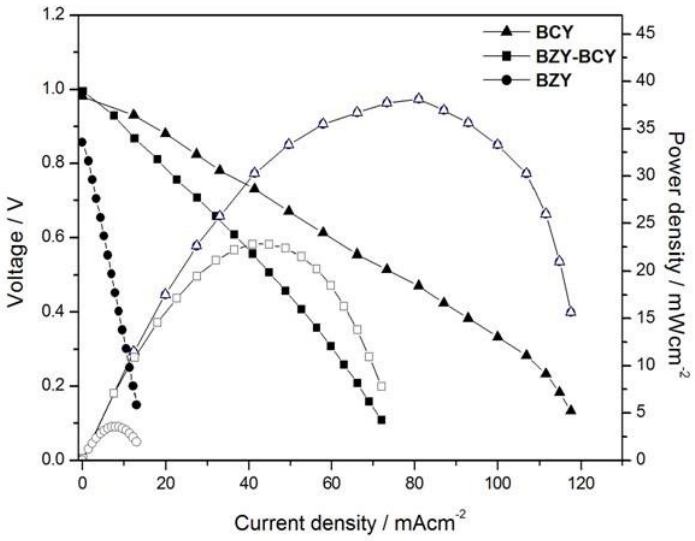

Figure 3.8: I-V curves and power density output from humidified H2-ambient air fuel cell tests at 700°C of the BZY-BCY bilayer, $BaCe_{0.8}Y_{0.2}O_{3-\delta}$ (BCY), and $BaZr_{0.8}Y_{0.2}O_{3-\delta}$ (BZY) electrolytes (1 mm thick)

The slightly lower conductivity value of the bilayer with respect to that of the BCY electrolyte at 700°C cannot explain the significantly lower maximum power output obtained from BZY-BCY bilayer based cell (23 $mWcm^{-2}$) in comparison to the value recorded for the BCY-based cell (38 $mWcm^{-2}$). Therefore, the Pt electrodes must contribute differently to the total cell polarization in the case of the bilayer and BCY electrolyte. This could be, however, not surprising since in Chapter 2 (Part B) it was found the ASR of Pt electrode, both in hydrogen and air condition, increased significantly when applied over BZY electrolyte rather than BCY. In the case of the bilayer electrolyte, Pt paste was applied to the BCY electrolyte on one side and on the BZY electrolyte to the other side.

3.6 Overpotential Analysis

To analyze the resistance of the Pt/bilayer interface, ASR measurements were performed using a Pt/bilayer/Pt symmetrical cell in ambient air and wet hydrogen, and the values as a function of temperature are shown in figure 3.9. For comparison, figure 3.9 reports also the ASR values of Pt/BCY and Pt/BZY symmetric cells in the same experimental conditions. As expected, the ASR of the Pt/bilayer interface was intermediate between those of the Pt/BZY and Pt/BCY interfaces, both in air and in hydrogen atmosphere.

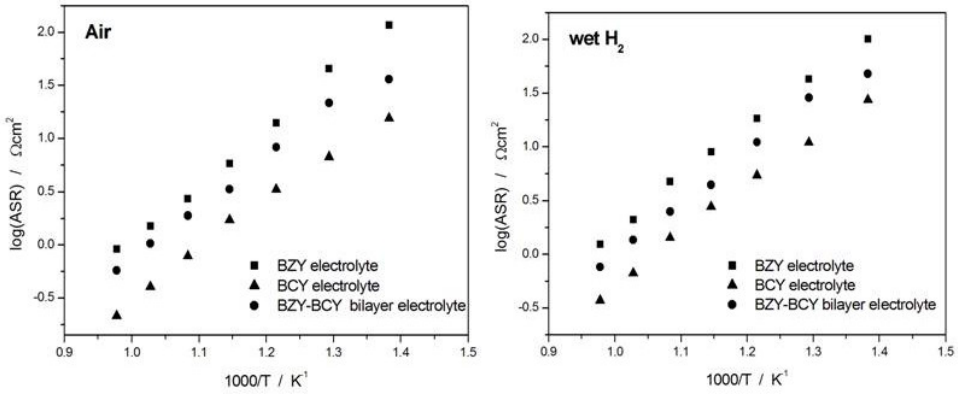

Figure 3.9: Temperature ASR dependence of Pt electrodes applied over BZY-BCY bilayer, $BaCe_{0.8}Y_{0.2}O_{3-\delta}$ (BCY), and $BaZr_{0.8}Y_{0.2}O_{3-\delta}$ (BZY) electrolytes in wet hydrogen and ambient air.

EIS measurements were performed during the fuel cell tests to investigate the contribution of the ohmic electrolyte resistance and of the electrode polarization resistance to the total voltage loss. Figure 3.10 shows the typical EIS plots for BZY-BCY bilayer based fuel cells measured at 700°C under open-circuit voltage conditions. For comparison, also the BCY complex impedance plane plot is reported.

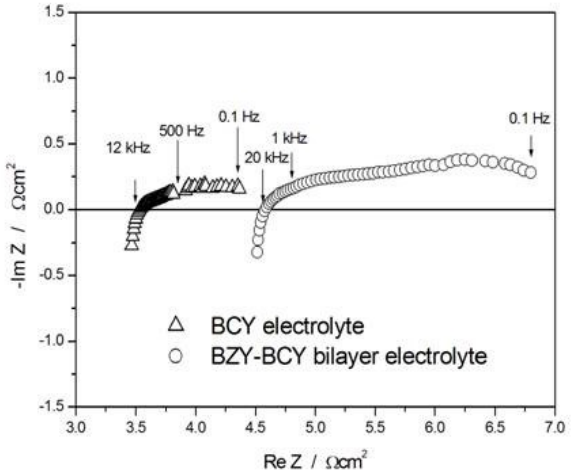

Figure 3.10: EIS plots of the $BaCe_{0.8}Y_{0.2}O_{3-\delta}$ (BCY) and BZY-BCY bilayer based fuel cells measured at 700°C under open circuit conditions.

The close values of the ohmic resistance of the two electrolytes were consistent with the small difference in their electrical conductivity values measured at 700°C (fig. 3.7), but the electrode polarization resistance was larger in the case of the bilayer electrolyte.

Figure 3.11 compares the polarization curves (open symbols) with the ohmic (iR) losses (filled symbols), which were estimated from the BCY and the BZY-BCY bilayer electrolyte resistance measured by EIS. The modulus of the difference between the values of the two curves taken at the same current density gives a measure of the electrode overpotential (η_p).

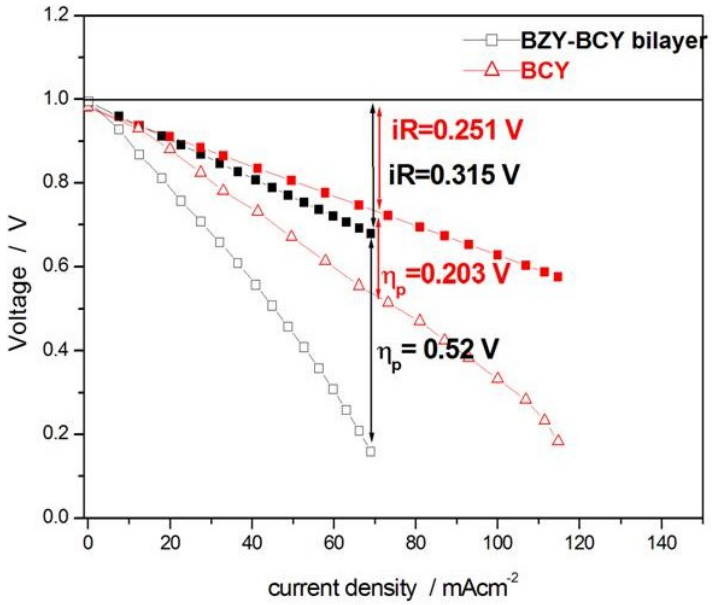

Figure 3.11: I-V curves (open symbols), iR loss curves (filled symbols) and electrode polarization (ηp) of the BCY and BZY-BCY bilayer electrolyte based fuel cells with Pt electrodes at 700°C.

The iR losses of the two electrolytes, taken at the same current density, were very close (0.315 and 0.251 V for the bilayer and BCY, respectively). On the other hand, the polarization drop at the Pt electrodes (η_p) was significantly larger for the bilayer electrolyte than for BCY (0.52 and 0.203V, respectively). This finding, together with the ASR measurements of the Pt/bilayer interface, clearly shows that significant problems arose from the Pt-BZY interface.

3.7 Comparison

Figure 3.12 summarizes the power density output obtained from Pt/electrolyte/Pt fuel cells based on chemically stable proton conductor electrolytes.

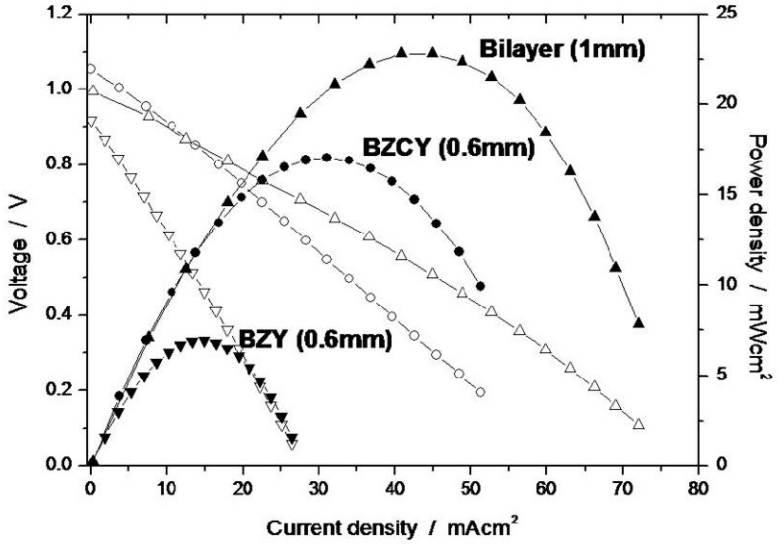

Figure 3.12: I-V curves and power density output of Pt/$BaZr_{0.}$ $Y_{0.2}O_{3-\delta}$ (BZY)/Pt, Pt/$BaZr_{0.5}Ce_{0.3}Y_{0.2}O_{3-\delta}$ (BZCY)/Pt, and Pt/ bilayer/Pt single cells measured at 700°C in wet hydrogen-air fuel cell experiments.

$BaZr_{0.5}Ce_{0.3}Y_{0.2}O_{3-\delta}$ (BZCY) was able to produce power output 2.8 times higher than the BZY electrolyte. Better results have been obtained with the bilayer electrolyte which was able to generate power density 5.6 times higher than the BZY electrolyte (considering both electrolyte 1 mm thick). Therefore, the BZY-BCY bilayer turned out to be a promising solution to obtain a stable proton conductor electrolyte without compromising too much the electrical conductivity with respect to the better performing BCY electrolyte. Using a thinner BCY substrate reduces ohmic resistance and thus leads to higher power density. Furthermore, a more accurate control on the interface microstructure may allow the reduction of the BZY film thickness. However, it seems that the main challenge will be the selection of a more suitable cathode material at the interface with BZY.

3.8 References

1. K. Katahira, Y. Kohchi, T. Shimura, H. Iwahara, *Solid State Ionics*, 138 (2000) 91.
2. K. Namura, H. Kageyama, *Solid State Ionics*, 178 (2007) 661

Chapter 4: Development of Cathode Materials for Application in IT-SOFCs based on Proton Conductor Electrolytes

4.1 Introduction

The significant advantages coming for the reduction of SOFC operating temperature have been widely explained in Chapter 1 (Part A). However, the reduction of SOFC operating temperature causes large overpotential at the electrode–electrolyte interface. In particular, the cathode plays a critical role in establishing intermediate operating temperature because of the oxygen reduction kinetics, which are several orders of magnitude slower than the kinetics related to the fuel oxidation.

Despite the growing attention received by high temperature proton conductors (HTPC) in the last decade, scarce fundamental studies have been performed on cathodes for application in fuel cells based on these electrolytes. Noble metals, like Pt, have been widely used as cathode materials because of their good catalytic activity. However, in addition to the elevated cost of platinum, several authors [1] have pointed out that the overpotential of Pt cathode in a proton conductor fuel cell could not be negligible below 900°C. In agreement with these literature data, the studies presented in Chapter 2 and 3 (Part B) have shown that Pt electrode polarization can largely contribute to the total cell overpotential. Mixed electronic-oxygen ion conductors (MIECs), such as cobalto-ferrite perovskites, which are the state-of-the-art cathode materials for IT-SOFCs based on oxygen ion conductor electrolytes,[2,3] have been also reported in literature as cathode materials for proton conductor based fuel cells.[4-10] However, also using a MIEC cathode, the overall fuel cell performance was mainly limited by the cathode overpotential.

A good candidate cathode material for a proton conducting electrolyte should exhibit high electrical conductivity, large electrode-electrolyte-air triple phase boundary (TPB) length, adequate porosity for gas transport, good compatibility with the electrolyte, and good catalytic activity for the following electrode reaction.[11,12]

$$2H^{+} + \frac{1}{2}O_2 + 2e^{-} \rightarrow H_2O \qquad (1)$$

Therefore, according to Equ.1, a mixed protonic/electronic conducting cathode materials should be desirable for application with a proton conductor electrolyte. Several advantages may come from the

use of mixed H^+/e^- conductor cathode instead of a pure electronic or a mixed O^{2-}/e^- conductor. Firstly, protons can diffuse within the cathode bulk and this enhances the electrochemical reaction active area from the TPB to the whole cathode specific surface. Furthermore, water generation is not limited at the electrode/electrolyte interface, but it can be produced from the whole cathode surface facilitating evaporation.[12] Thus, in principle, in a proton conductor based fuel cell faster electrode processes, and thus superior cell performance, could be achieved using H^+/e^- mixed conductor cathode. However, reports on materials for this application are surprisingly limited.

Therefore, the challenge of this work was to investigate the mixed protonic-electronic conduction properties of doped $SrCeO_3$ and $BaCeO_3$ oxides in oxidizing atmosphere (cathodic environment). To achieve high electronic conductivity, different dopants were tested. Rare earth elements, such as Yb, Eu, and Sm, were chosen because of their multivalent oxidation states (+3/+2), which can promote electronic conduction,[13] and low third ionization potential. Total electrical conductivity was investigated in dry and wet oxidizing conditions as a function of temperature and oxygen partial pressure. Partial conductivities and ionic/electron-hole transport numbers were estimated from conductivity measurements at different oxygen partial pressures according to the defect model established by Song et al.[14] The conductivity-p_{O_2} technique adopted in this work, even though it is not such a direct method as the concentration cell technique, does not pose stringent requirements on gas sealing. $SrCe_{0.9}Yb_{0.1}O_{3-\delta}$ (10YbSC) and $BaCe_{0.9}Yb_{0.1}O_{3-\delta}$ (10YbBC) perovskite oxides were identified as promising mixed H^+/e^- conductors under high p_{O_2} atmosphere. However, the area specific resistance (ASR) of the interface of these cathode materials with Y-doped barium cerate proton conductor electrolyte was extremely large, probably because of their too low partial electronic conductivity.

For SOFC based on oxygen-ion electrolytes, a successful approach to reduce cathode overpotential has been the development of composite electrodes, which allow the extension of the TPB from the electrolyte/cathode interface to the whole cathode bulk. High TPB density results in a large number of reaction sites and so improves cathode performance.[15] Generally, a highly electron-conducting phase, such as $La_{1-x}Sr_xMnO_3$ (LSM), and a highly oxygen-ion conducting phase, such as doped CeO_2, are combined together to form composite cathodes.[16-18] Good cathode performance has been reported also using MIEC cathode, such as $La_{1-x}Sr_xCo_{1-y}Fe_yO_3$ (LSCF), which presents a good electronic conductivity and also a relatively high ion conductivity. However, at reduced operating temperature, the LSCF ionic conductivity decreases. Thus, a second phase is usually added also to the LSCF to obtain a composite cathode with high electronic and ionic conductivity at intermediate temperature.[9,10]

Considering the above strategies for cathodes working with oxygen-ion electrolytes, composite cathodes were developed for IT-SOFC based on proton conducting electrolyte, using LSCF combined with 10YbSC or 10YbBC. LSCF was chosen not only because of its electronic conductivity, but also because it allows faster oxygen surface exchange being a mixed O^{2-}/e^- conductor.

The knowledge of the electrode behavior in terms of microstructural and electrochemical parameters is important to optimize the composite cathode performance. Hence, the ASR of the composite cathodes was studied as a function of cathode composition, sintering temperature, particle size, and oxygen partial pressure.

4.2 Study of Mixed Protonic-Electronic Conduction

4.2.1 Total Conductivity vs. Temperature

Polycrystalline $SrCe_{0.9}M_{0.1}O_{3-\delta}$ and $BaCe_{0.9}M_{0.1}O_{3-\delta}$ (M = Yb, Eu, and Sm) samples were prepared by conventional solid-state reaction. Starting materials were high-purity powders of $BaCO_3$ (99.95%, Alfa Aesar), $SrCO_3$ (99.9%, Alfa Aesar), CeO_2 (99.9%, Alfa Aesar), Yb_2O_3 (99.99%, Alfa Aesar), Eu_2O_3 (99.99%, Alfa Aesar), and Sm_2O_3 (99.99%, Alfa Aesar). Appropriate amounts of powders were mixed, ground in a ball mill with stabilized zirconia spheres for 48 h, and calcined at 1300°C for 10 h in air. XRD analysis showed the formation of pure phases for all the $SrCe_{0.9}M_{0.1}O_{3-\delta}$ and $BaCe_{0.9}M_{0.1}O_{3-\delta}$ (M = Yb, Eu, and Sm) oxides calcined at 1300°C, with particle size, measured by field emission scanning electron microscopy (FE-SEM), around 0.5 μm. Dense pellets were obtained after sintering at 1500°C. Figure 4.1 shows typical SEM micrographs of the $SrCe_{0.9}Yb_{0.1}O_{3-\delta}$ (10YbSC) and $BaCe_{0.9}Yb_{0.1}O_{3-\delta}$ (10YbBC) surface. Irrespective of the dopant, all the strontium and barium cerate pellets presented similar microstructures. Slightly smaller grain size was observed for the barium cerate pellets (2-7 μm) with respect to the strontium cerate pellets (4-10 μm).

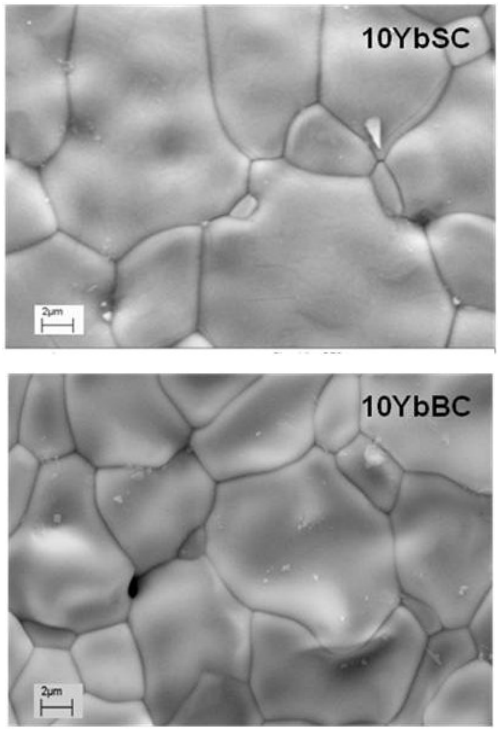

Figure 4.1: SEM micrographs of the surface of $SrCe_{0.9}Yb_{0.1}O_{3-\delta}$ (10YbSC) and $BaCe_{0.9}Yb_{0.1}O_{3-\delta}$ (10YbBC) pellets after sintering at 1500°C.

Figures 4.2 and 4.3 show the electrical conductivity of $SrCe_{0.9}M_{0.1}O_{3-\delta}$ and $BaCe_{0.9}M_{0.1}O_{3-\delta}$ (M = Yb, Eu, and Sm) in dry and wet oxygen atmospheres, respectively.

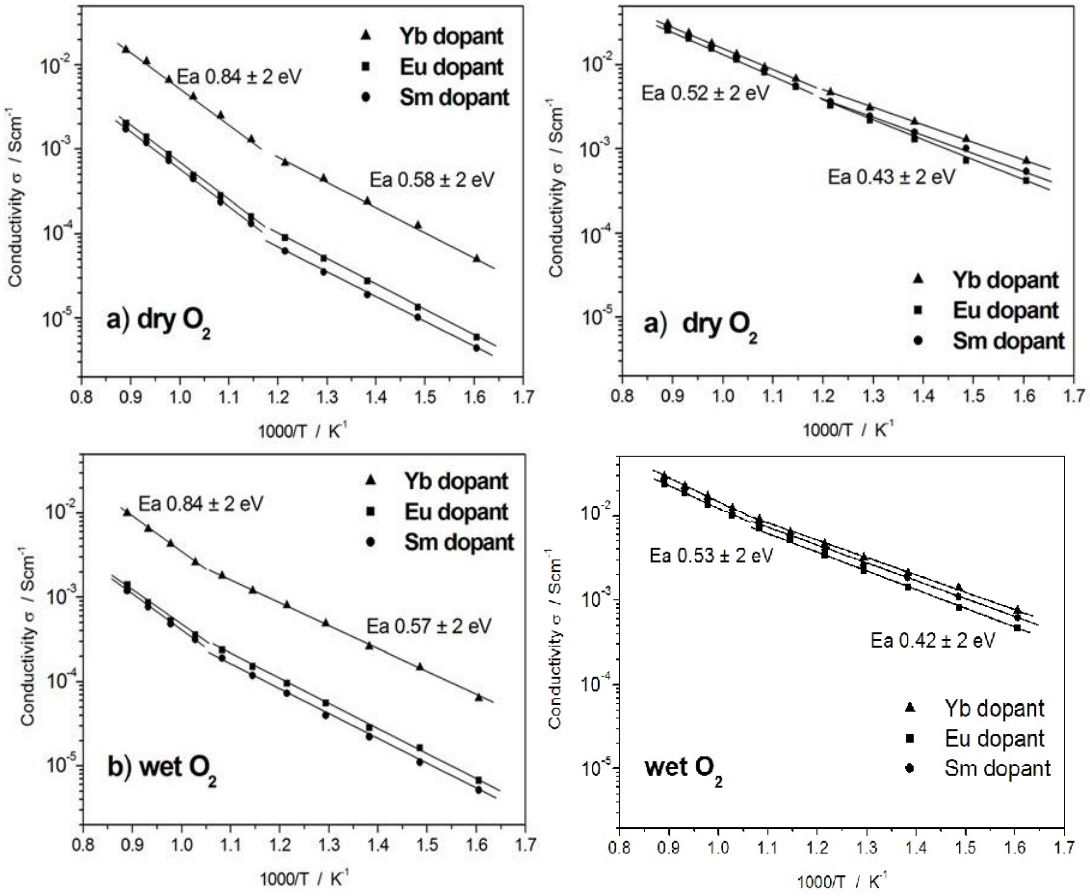

Figure 4.2: $SrCe_{0.9}M_{0.1}O_{3-\delta}$ (M=Yb, Eu, Sm) total electrical conductivity in dry (a) and wet (b) oxygen atmosphere.

Figure 4.3: $BaCe_{0.9}M_{0.1}O_{3-\delta}$ (M=Yb, Eu, Sm) total electrical conductivity in dry (a) and wet (b) oxygen atmosphere.

$SrCeO_3$ and $BaCeO_3$ based oxides presented the highest conductivity values, both in dry and wet conditions, when doped with Yb rather than Eu or Sm. This is particularly evident in the case of strontium cerates.

In mixed conductor oxides the electronic conduction involves a hopping mechanism where charge transfer occurs between two neighboring ions of different oxidation states.[19] Therefore, electron-hole conduction in $SrCe_{0.9}M_{0.1}O_{3-\delta}$ and $BaCe_{0.9}M_{0.1}O_{3-\delta}$ (M = Yb, Eu, and Sm) oxides can occur by mean of the dopant redox couple M^{3+}/M^{2+}. The dopant concentration in different oxidation states depends on its ionization potential. Therefore, the electronic conductivity should increase with decreasing the dopant third ionization potential.[14,20] The third ionization potential of Yb, Eu, and Sm

presents almost the same values (24.8, 25, and 23.4 eV), thus it was not this parameter which determined the observed difference in conductivity. Also the dopant ionic radius and the dopant polarizability can influence electronic conduction in oxides. Electronic conduction, occurring by hopping mechanism, benefits from small hopping distance. Generally, the hopping distance decreases with increasing dopant ionic radius.[14] The ionic radius of Sm(III) is 109.8 pm, while for Eu(III) is 108.9 pm, and for Yb(III) is 116 pm.[14,21] The hopping distance of Yb(III) is the smallest. This could explain why Yb-doped $SrCeO_3$ and $BaCeO_3$ oxides showed the largest conductivity among the tested samples. Moreover, as previously said, the dopant polarizability can also affect electronic conduction. The larger the difference in electronegativity between dopant cation and oxygen anion, the more polarizable the dopant. Since the electronegativity of Yb is higher than Eu and Sm, there is larger probability to find a hopping electron polarized on the oxygen sites of the Eu and Sm doped oxides. Therefore, the frequency of successful electron jumps between neighboring multivalent dopant ions decreases with increasing the difference in electronegativity with respect to oxygen.[22]

As previously mentioned, it is interesting to note that a much larger dopant effect was observed for $SrCeO_3$ compared to $BaCeO_3$. The reason could arise from their different crystalline structure. Undoped barium cerate was found to be orthorhombic, space group Pnma, evolving toward cubic ideal perovskite structure upon heating.[23] At low temperature, $BaCeO_3$ perovskite structure presents two crystallographically non-equivalent oxygen sites. When the $BaCeO_3$ perovskite structure is doped on the B site, the resulting oxide ion vacancies do not equally occupy these sites, indicating that they are also energetically non-equivalent. Increasing the temperature, the oxygen sites of doped-$BaCeO_3$ become crystallographically and energetically equivalent,[24] favouring oxide ion transport.[25] Neutron diffraction and single crystal XRD investigation have found $SrCeO_3$ and its doped derivates isostructural to $BaCeO_3$, but displaying a larger distortion from cubic symmetry than $BaCeO_3$.[26,27] This comes from the smaller ionic radius of Sr^{2+} (0.144 nm) with respect to Ba^{2+} (0.161 nm).[28] Moreover $SrCeO_3$ based oxides do not show temperature induced polymorphism, retaining the orthorhombic structure up to a temperature of at least 1000° with two distinct O^{2-} anion sites with different symmetries.[25] This is probably the reason why $SrCeO_3$ based oxides present lower oxygen-ion conductivity with respect to $BaCeO_3$ based compounds.[24] However, the oxygen ion conduction of these perovskites can benefit by the use of dopants with large ionic radius. In particular, Iwahara et al. [29] found that the contribution of oxide ion to the total conduction grows with increasing the dopant ionic radius, which is consistent with the fact that large ions enlarge the free volume and favour oxide-ion conduction. Therefore, since Yb presents a large ionic radius, the marked increase in Yb-doped $SrCeO_3$ conductivity can be explained by an increasing oxygen ion conductivity. For $BaCeO_3$-based compounds, oxygen-ion conduction is easily activated at high temperatures, and thus the oxygen ion conductivity is probably less influenced by the kind of dopant than in the case of strontium cerates.

For all the samples, the activation energy (E_a) increased both in dry and wet conditions from the low to the high temperature ranges, indicating a change in conduction mechanism. The transition in

activation energies can be associated with a change from a prevalent ionic conduction in the low temperature range to a regime, at higher temperatures, in which electron hole conduction mechanism became dominant. High temperatures favor water desorption from these perovskites structure, resulting in a decrease in proton concentration, therefore, hole conduction can appear not only in dry but also in wet condition.[30,31] However, common to the all samples, the change in activation energy was recorded at a higher temperature in wet condition with respect to dry condition (700°C instead of 600°C), suggesting that in wet condition the decrease in proton concentration, and thus the increase in electronic conductivity, started at higher temperatures.

Comparing the Arrhenius plots of doped $SrCeO_3$ and $BaCeO_3$ (Figs. 4.2 and 4.3), barium cerates showed higher conductivity and lower activation energy than strontium cerates both in dry and wet conditions. These findings are consistent with the literature, which reported higher conductivity values and lower activation energies for $BaCeO_3$ than $SrCeO_3$ based proton conductors.[30,32-34]

4.2.2 Partial Ionic and Electronic Conductivity

In oxygen atmosphere the total electrical conductivity (σ_{tot}) is the sum of ionic (σ_i) and electron-hole (σ_h) partial conductivities. To separate the two contributions, conductivity measurements were performed as a function of p_{O_2} and the observed experimental data were analyzed according to the defect-reaction model established by Song et al.,[14] which states that only the partial electronic conductivity shows a direct dependency on p_{O_2}, according to:

$$\sigma_{tot} = \sigma_i + \sigma_h = a + bp_{O_2}^{1/4} \quad (2)$$

Therefore, according to Eq. (2), fitting the linear experimental data of σ_{tot} vs $p_{O_2}^{1/4}$, the partial ionic (σ_i) and electronic (σ_h) conductivities can be determined as intercepts and slopes, respectively.[14] Conductivity measurements were performed over a p_{O_2} range between $5x10^{-5}$ and 1 atm in dry condition, at 500, 600, 700, and 800°C. Figures 4.4 and 4.5 show the electrical conductivity as a function of $p_{O_2}^{1/4}$ for doped $SrCeO_3$ and $BaCeO_3$ oxides, respectively.

The good linear relationship between σ_{tot} and $p_{O_2}^{1/4}$ observed for all the tested samples validates the use of the proposed defect model.

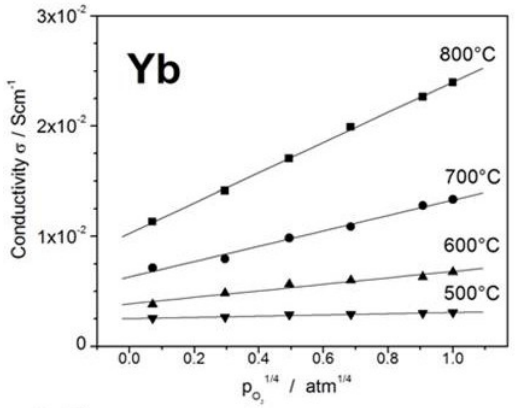

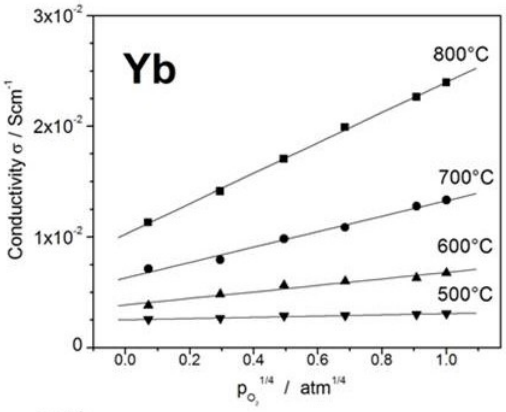

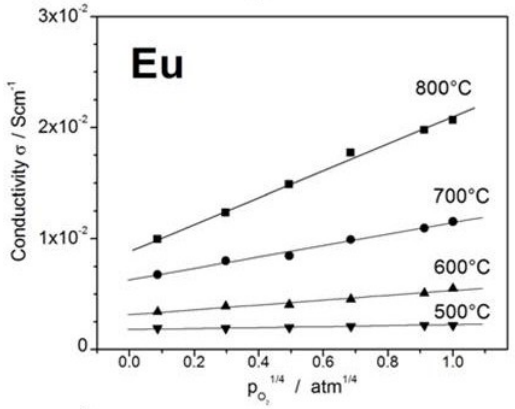

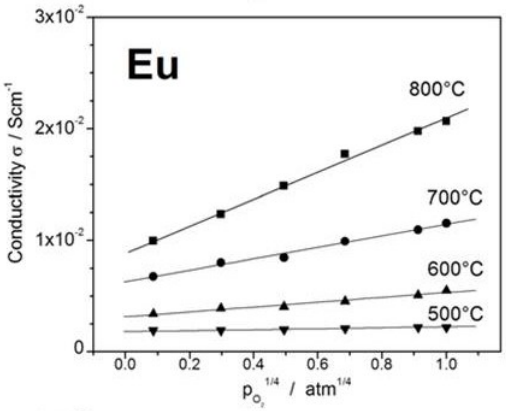

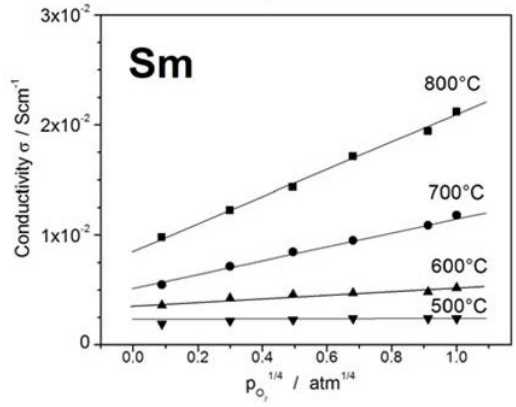

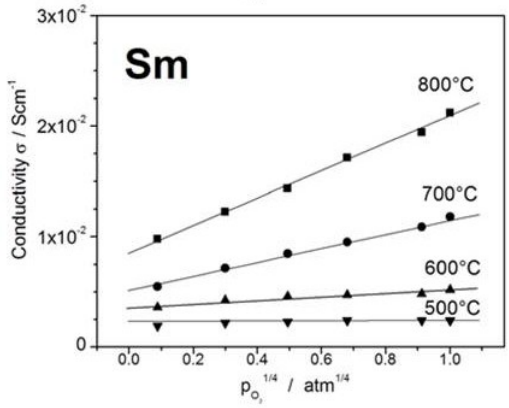

Figure 4.4: $SrCe_{0.9}M_{0.1}O_{3-\delta}$ (M=Yb, Eu, Sm) electrical conductivity as a function of $p_{O_2}^{1/4}$ in dry O_2.

Figure 4.5: $BaCe_{0.9}M_{0.1}O_{3-\delta}$ (M=Yb, Eu, Sm) electrical conductivity as a function of $p_{O_2}^{1/4}$ in dry O_2.

Table 4.1 shows the numerical values of σ_i and σ_h obtained fitting the experimental data of σ_{tot} vs. $p_{O_2}^{1/4}$, and the total electrical conductivity values obtained as the sum of the partial conductivities and from direct measurements in dry O_2. It is important to underline that partial ionic conductivity σ_i is considered arising from both proton and oxygen ion conductivity. In fact, as reported in literature, these oxides can show pure oxygen ion conduction in a completely dry atmosphere or at temperatures higher

than 800 °C. [14,34,35] Therefore, since the data here reported were measured at T ≤ 800°C and some traces of water vapour could be present even in a carefully dried gas, it is believed that σ_i represents the sum of oxygen-ion and proton conduction.

	M	T	σ_i[Scm^{-1}]	σ_h[Scm^{-1}]	$\sigma_{tot,}$[Scm^{-1}]	
					Model	Exp.
$SrCe_{0.9}M_{0.1}O_{3-\delta}$	Yb	800°C	$3.7x10^{-3}$	$7.5x10^{-3}$	$1.1x10^{-2}$	$1.1x10^{-2}$
		700°C	$2.0\ x10^{-3}$	$2.2x10^{-3}$	$4.2x10^{-3}$	$4.2x10^{-3}$
		600°C	$1.0x10^{-3}$	$4.5x10^{-4}$	$1.5x10^{-3}$	$1.3x10^{-3}$
		500°C	$4.0x10^{-4}$	$6.5x10^{-5}$	$4.6x10^{-4}$	$4.5x10^{-4}$
	Eu	800°C	$3.5x10^{-4}$	$9.6x10^{-4}$	$1.3x10^{-3}$	$1.4x10^{-3}$
		700°C	$2.3x10^{-4}$	$2.5x10^{-4}$	$4.8x10^{-4}$	$4.9x10^{-4}$
		600°C	$1.1x10^{-4}$	$4.7x10^{-5}$	$1.6x10^{-4}$	$1.6x10^{-4}$
		500°C	$4.2x10^{-5}$	$8.1x10^{-6}$	$5.0x10^{-5}$	$5.1x10^{-5}$
	Sm	800°C	$2.9x10^{-4}$	$8.6x10^{-4}$	$1.2x10^{-3}$	$1.2x10^{-3}$
		700°C	$1.7x10^{-4}$	$2.3x10^{-4}$	$4.0x10^{-4}$	$4.5x10^{-4}$
		600°C	$7.7x10^{-5}$	$4.0x10^{-5}$	$1.2x10^{-4}$	$1.3x10^{-4}$
		500°C	$2.8x10^{-5}$	$7.8x10^{-6}$	$3.6x10^{-5}$	$3.5x10^{-5}$
$BaCe_{0.9}M_{0.1}O_{3-\delta}$	Yb	800°C	$1.0x10^{-2}$	$1.5x10^{-2}$	$2.5x10^{-2}$	$2.4x10^{-2}$
		700°C	$6.3x10^{-3}$	$7.0x10^{-3}$	$1.3x10^{-2}$	$1.3x10^{-2}$
		600°C	$3.8x10^{-3}$	$2.7x10^{-3}$	$6.5x10^{-3}$	$6.8x10^{-3}$
		500°C	$2.0x10^{-3}$	$7.0x10^{-4}$	$2.7x10^{-3}$	$3.1x10^{-3}$
	Eu	800°C	$8.3x10^{-3}$	$1.1x10^{-2}$	$1.9x\ 10^{-2}$	$2.0x10^{-2}$
		700°C	$5.1x10^{-3}$	$5.0x10^{-3}$	$1.0x\ 10^{-2}$	$1.2x10^{-2}$
		600°C	$3.0x10^{-3}$	$1.9x10^{-3}$	$4.9x\ 10^{-3}$	$5.5x10^{-3}$
		500°C	$1.6x10^{-3}$	$5.0x10^{-4}$	$2.1x\ 10^{-3}$	$2.2x10^{-3}$
	Sm	800°C	$8.1x10^{-3}$	$1.2x10^{-2}$	$2.0x\ 10^{-2}$	$2.1x10^{-2}$
		700°C	$5.2x10^{-3}$	$5.2x10^{-3}$	$1.0x10^{-2}$	$1.2x10^{-2}$
		600°C	$2.7x10^{-3}$	$1.6x10^{-3}$	$4.3x\ 10^{-3}$	$5.6x10^{-3}$
		500°C	$1.6x10^{-3}$	$5.0x10^{-4}$	$2.1x10^{-3}$	$2.4x10^{-3}$

Table 4.I: Numerical values of partial ionic (σ_i) and electronic (σ_h) conductivity from fitting experimental data of σ vs. $p_{O_2}^{1/4}$ and total conductivity (σ_{tot}) as the sum of partial conductivities (Model) and as measured in dry oxygen (Exp.) for $SrCe_{0.9}M_{0.1}O_{3-\delta}$ and $BaCe_{0.9}M_{0.1}O_{3-\delta}$ (M = Yb, Eu, and Sm).

From Table I, comparing the values of the total conductivity calculated as the sum of partial conductivities and the experimental one, the good agreement between these values confirms again the validity of the considered defect model.

Figures 4.6 and 4.7 show the temperature dependence of partial conductivities of $SrCe_{0.9}M_{0.1}O_{3-\delta}$ and $BaCe_{0.9}M_{0.1}O_{3-\delta}$ (M = Yb, Eu, and Sm), respectively.

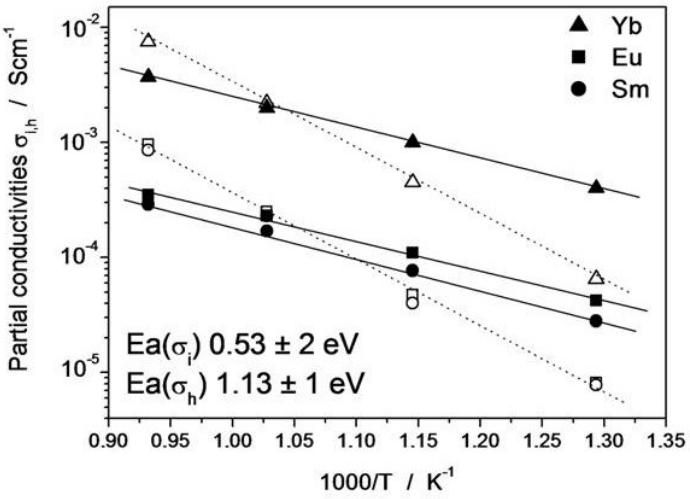

Figure 4.6: $SrCe_{0.9}M_{0.1}O_{3-\delta}$ (M=Yb, Eu, Sm) partial ionic (σ_i, filled symbol) and electronic (σ_h, open symbol) conductivities as calculated from Equ.2.

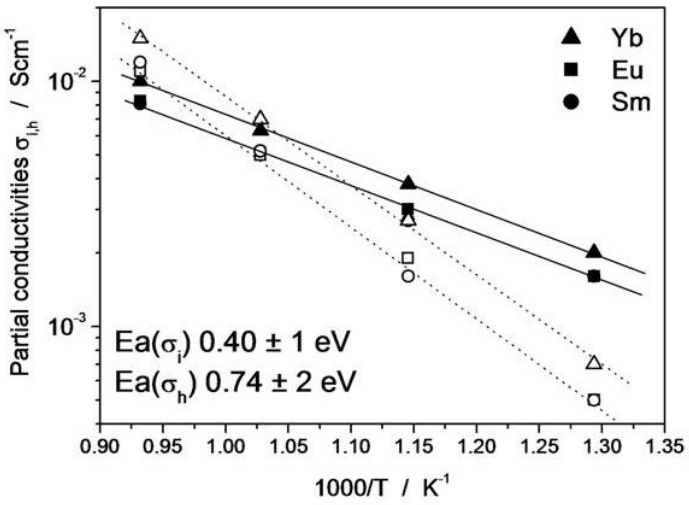

Figure 4.7: $BaCe_{0.9}M_{0.1}O_{3-\delta}$ (M=Yb, Eu, Sm) partial ionic (σ_i, filled symbol) and electronic (σ_h, open symbol) conductivities as calculated from Equ.2.

For all samples, the electron-hole conductivity was larger than the ionic conductivity above 700°C. At lower temperatures, because of the lower activation energy for ion conduction, the ionic conductivity presented larger values than the electron-hole conductivity.

The activation energy for ionic transport was determined to be around 0.53 for strontium cerates and 0.40 eV for barium cerates, irrespectively of the dopant. For electron hole conduction, the activation energies were larger, reaching about 1.13 and 0.74 eV for the doped $SrCeO_3$ and $BaCeO_3$

oxides, respectively. The obtained E_a values are well in line with literature data about strontium and barium cerates.[30,36,37] The activation energies related to the ionic conductivity presented almost the same values calculated in the low temperature range of the Arrhenius plots showed in figs. 4.2 and 4.3, both for doped $SrCeO_3$ and $BaCeO_3$. This result strongly supports the predominance of ionic conduction as the major transport mechanism in the lower temperature range. The E_a values calculated in the high temperature range of the Arrhenius plots showed in figs. 4.2 and 4.3 result intermediate between the activation energy values calculated for the ion and electron hole conduction, suggesting a mixed ionic-electron hole conduction mechanism.

To better understand the contribution of ionic and electron-hole conductivity at different temperatures, ionic (t_i) and electron-hole (t_h) transport numbers were calculated from the partial conductivity values. The result is displayed in figure 4.8.

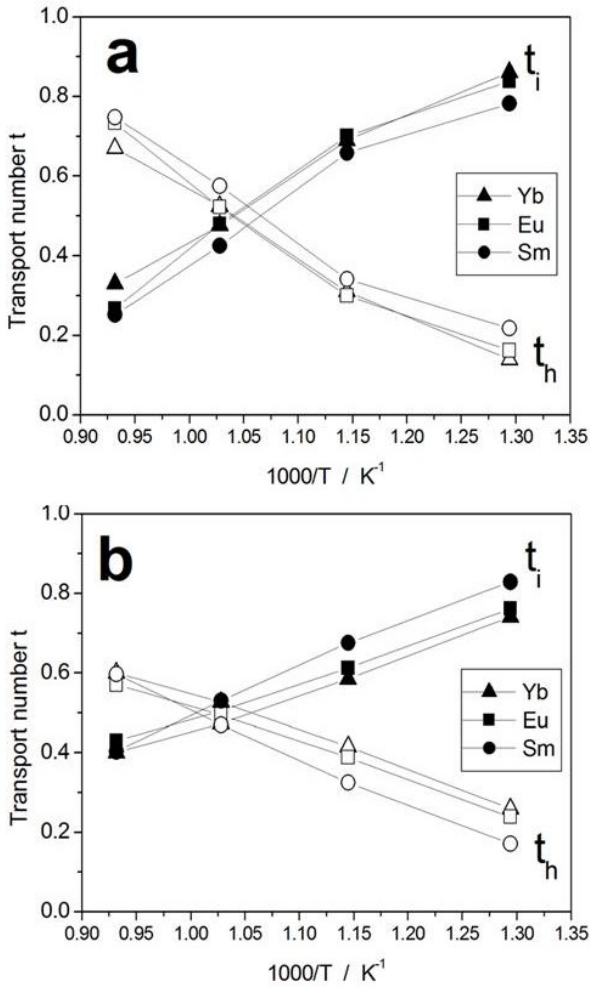

Figure 4.8: Ionic transport number (t_i, filled symbol) and electronic transport number (t_h, open symbol) of $SrCe_{0.9}M_{0.1}O_{3-\delta}$ (a) and $BaCe_{0.9}M_{0.1}O_{3-\delta}$ (b) where M=Yb, Eu, Sm.

No significant influence of dopants on the ionic and electron-hole transport numbers can be observed from fig. 4.8, both for doped $SrCeO_3$ and $BaCeO_3$ oxides. For all the tested samples, and especially for the strontium cerates, the electron-hole transport number was larger than the ionic transport number at temperatures above 700°C. The ionic conduction appeared predominant below 600°C.

4.2.3 Partial Conductivities of $SrCe_{0.9}Yb_{0.1}O_{3-\delta}$ and $BaCe_{0.9}Yb_{0.1}O_{3-\delta}$ at Different p_{H_2O}

Among the different materials investigated, $SrCe_{0.9}Yb_{0.1}O_{3-\delta}$ and $BaCe_{0.9}Yb_{0.1}O_{3-\delta}$ oxides showed the highest conductivity values.

In a fuel cell based on a proton conductor electrolyte water is generated at the cathode side, thus conductivity measurements of the above oxides were performed at different water partial pressures to investigate the difference in their conduction mechanism between dry (very low p_{H_2O}) and wet (p_{H_2O} about 0.03 atm) oxygen atmosphere.

Figure 4.9 shows that the electrical conductivity of $SrCe_{0.9}Yb_{0.1}O_{3-\delta}$ and $BaCe_{0.9}Yb_{0.1}O_{3-\delta}$ as a function of $p_{O_2}^{1/4}$. The observed good linear relationship validates the use of the proposed defect model also in wet condition.

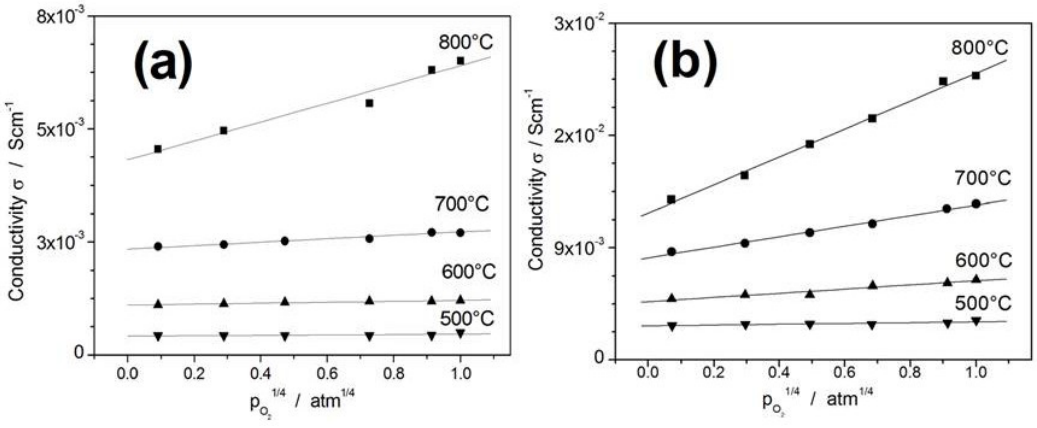

Figure 4.9: Electrical conductivity of $SrCe_{0.9}Yb_{0.1}O_{3-\delta}$ (a) and $BaCe_{0.9}Yb_{0.1}O_{3-\delta}$ (b) as a function of $p_{O_2}^{1/4}$ in wet condition.

The data fit reported in fig. 4.9 allowed the calculation the partial ion conductivity (σ_i) and electron-hole conductivity (σ_h) in wet oxidizing atmosphere. The numerical values are reported in table 4.2, together with the total conductivity values as calculated by the sum of partial conductivities and as obtained from direct measurements in wet O_2 (figs. 4.2 and 4.3). Comparing the conductivity values reported in Table 4.2, model predictions match experimental data also in wet conduction.

	T	σ_i[Scm^{-1}]	σ_h[Scm^{-1}]	σ_{tot} [Scm^{-1}]	
				Model	Exp.
$SrCe_{0.9}Yb_{0.1}O_{3-\delta}$	800°C	$4.5x10^{-3}$	$2.0x10^{-3}$	$6.5x10^{-3}$	$6.5x10^{-3}$
	700°C	$2.5x10^{-3}$	$3.8x10^{-4}$	$2.9x10^{-3}$	$2.6x10^{-3}$
	600°C	$1.2x10^{-3}$	$1.0x10^{-4}$	$1.3x10^{-3}$	$1.2x10^{-3}$
	500°C	$4.8x10^{-4}$	$1.1x10^{-5}$	$4.9x10^{-4}$	$4.9x10^{-4}$
$BaCe_{0.9}Yb_{0.1}O_{3-\delta}$	800°C	$1.2x10^{-2}$	$1.0x10^{-2}$	$2.2x10^{-2}$	$2.3x10^{-2}$
	700°C	$8.2x10^{-3}$	$4.2x10^{-3}$	$1.2x10^{-2}$	$1.2x10^{-2}$
	600°C	$4.7x10^{-3}$	$1.7x10^{-3}$	$6.4x10^{-3}$	$6.4x10^{-3}$
	500°C	$2.7x10^{-3}$	$4x10^{-4}$	$3.1x10^{-3}$	$3.2x10^{-3}$

Table 4.2: Numerical values of partial ionic (σ_i) and electronic (σ_h) from fitting the experimental data of data of σ vs. $p_{O_2}^{1/4}$ and total conductivity (σ_{tot}) as the sum of partial conductivities (Model) and as measured in wet oxygen (Exp.) for $SrCe_{0.9}Yb_{0.1}O_{3-\delta}$ and $BaCe_{0.9}Yb_{0.1}O_{3-\delta}$ at different temperatures.

Figures 4.10 and 4.11 show the partial conductivities in dry and wet conditions of $SrCe_{0.9}Yb_{0.1}O_{3-\delta}$ and $BaCe_{0.9}Yb_{0.1}O_{3-\delta}$, respectively.

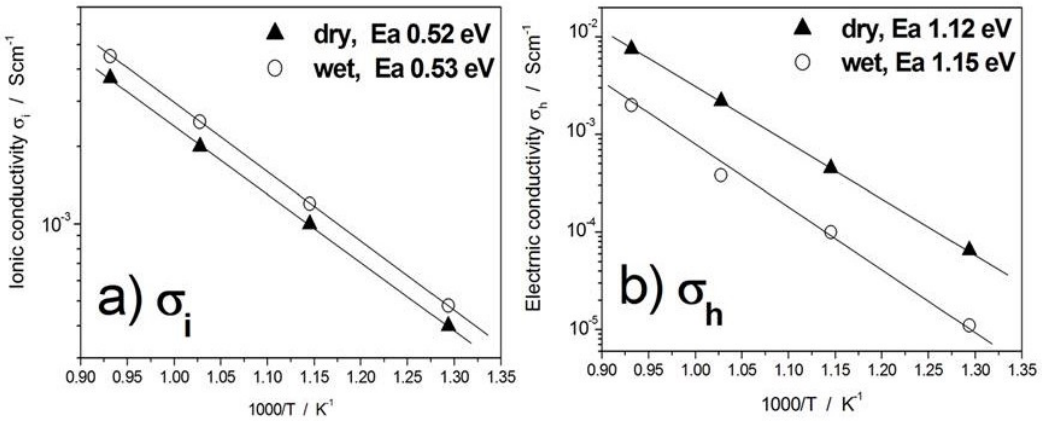

Figure 4.10: Partial ionic σ_i (a) and electronic σ_h (b) conductivity of $SrCe_{0.9}Yb_{0.1}O_{3-\delta}$ in dry and wet condition.

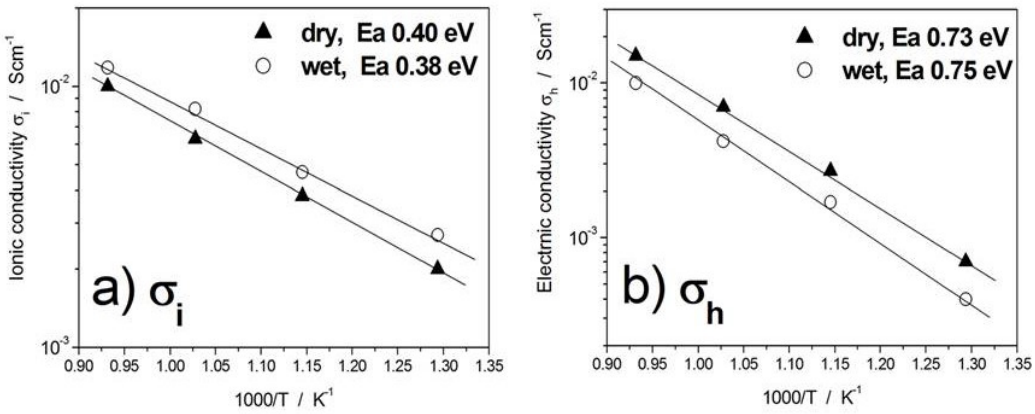

Figure 4.11: Partial ionic σ_i (a) and electronic σ_h (b) conductivity of $BaCe_{0.9}Yb_{0.1}O_{3-\delta}$ in dry and wet condition.

Increasing p_{H_2O} the ionic conductivity increased while the electronic conductivity decreased for both the oxides. This result is consistent with the proton incorporation mechanism that assumes that protons are generated at the expense of electron-holes, consuming oxygen vacancies.[14]

Figure 4.12 shows the ionic (t_i) and electron-hole (t_h) transport numbers in dry and wet conditions for $SrCe_{0.9}Yb_{0.1}O_{3-\delta}$ and $BaCe_{0.9}Yb_{0.1}O_{3-\delta}$, respectively.

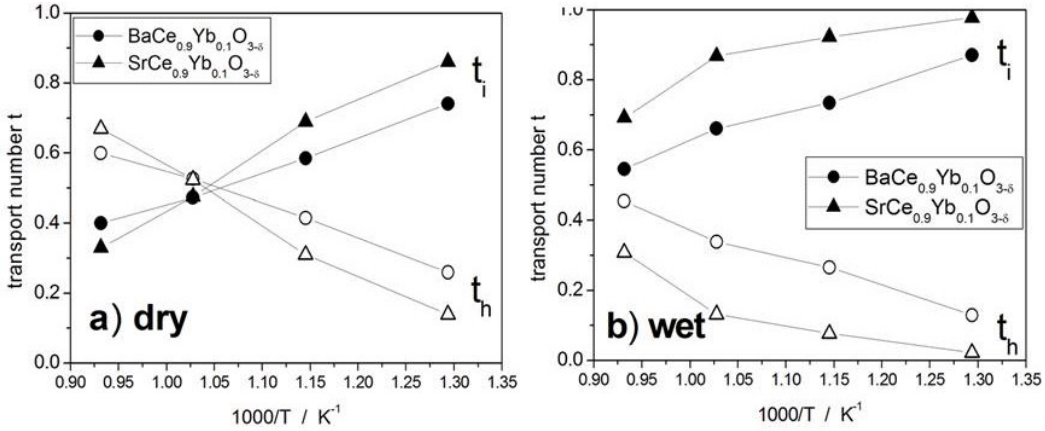

Figure 4.12: Ionic transport number (t_i, filled symbol) and electronic transport number (t_h, open symbol) of $SrCe_{0.9}Yb_{0.1}O_{3-\delta}$ and $BaCe_{0.9}Yb_{0.1}O_{3-\delta}$ in dry (a) and wet (b) oxygen atmosphere.

In dry condition, the two perovskite-type oxides presented almost the same values of ionic and electron hole transport numbers, with t_h larger than t_i for temperatures above 700°C. In wet condition, for both the oxides, t_i was larger than t_h in all the measured temperature range. It reached almost unity for $SrCe_{0.9}Yb_{0.1}O_{3-\delta}$ and 0.9 for $BaCe_{0.9}Yb_{0.1}O_{3-\delta}$ at 500°C. However, differently from dry condition, $BaCe_{0.9}Yb_{0.1}O_{3-\delta}$ showed larger electron transport number than $SrCe_{0.9}Yb_{0.1}O_{3-\delta}$.

4.3 Cathode Development

$SrCe_{0.9}Yb_{0.1}O_{3-\delta}$ (10YbSC) and $BaCe_{0.9}Yb_{0.1}O_{3-\delta}$ (10YbBC) were tested as cathode materials on a $BaCe_{0.8}Y_{0.2}O_{3-\delta}$ pellet. Cathode inks were prepared mixing 10YbSC or 10YbBC powders with an organic vehicle (α-terpineol as a solvent, di-n-butyl phthalate as a plasticizer, and polyvinylbutiral as a binder) until an appropriate viscosity for brushing was achieved. Symmetric cells were prepared by paint brushing the cathode slurry to each side of the $BaCe_{0.8}Y_{0.2}O_{3-\delta}$ (20BCY) pellet, drying at 150 °C for 3 h, and firing at 1100°C for 2 h. Silver mesh current collectors and platinum lead wires were pressed against the samples in a quartz reactor by the use of a ceramic screw-and-bolt assembly. The area specific resistance (ASR) of single-phase 10YbSC and 10YbBC porous cathodes was measured in wet air (about 3% vol. H_2O) by electrochemical impedance spectroscopy (EIS) using a Solartron 1260 impedance analyzer between 50 mHz and 500 kHz, with an AC voltage amplitude of 100 mV. From the complex impedance plane plot, the intercept with the real axis at high frequencies was considered as the ohmic resistance (R_{ohmic}) composed of the electrolyte resistance, possible electrode-sheet resistance and lead-contact resistance. The difference between the high frequency and low frequency intercepts with the real axis, composed by the sum of two contributions, was considered as the electrode reaction resistance (R_p). The area specific resistance (ASR) of the electrode reactions was calculated from the electrode resistance (R_p) by $ASR=(R_p*A)/2$, where A is the geometrical electrode area and the factor ½ takes into account the use of symmetrical cells.

For both 10YbSC and 10YbBC, the ASR measured values were extremely large, in the order of 10 kΩ cm^2 at 600°C, probably because of inadequate electronic conductivity and catalytic activity towards cathode reaction. In fact, the operating condition of practical interest in a FC based on a proton conductor electrolyte is wet oxygen atmosphere because water is generated at the cathode side. Data in fig. 4.12 show that a significant electronic conduction could be obtained in dry condition at a temperature as low as 600°C, but only at 700°C in wet condition, which is however the upper limit of the desired operating temperature range. Therefore, that Yb-doped barium and strontium cerates cannot be suitable cathode materials because of their poor electronic conduction

With the intent of increasing electronic conductivity, composite cathodes made of $La_{0.6}Sr_{0.4}Co_{0.2}Fe_{0.8}O_3$ (LSCF) combined with 10YbSC or 10YbBC were then investigated. LSCF was chosen not only because of its electronic conductivity, but also because it allows faster oxygen surface exchange being a mixed O^{2-}/e^- conductor. For comparison, also a single-phase LSCF cathode was tested. All the studied cathode compositions, with the relative label, are listed in Table 4.3.

Cathode composition	Label
$La_{0.6}Sr_{0.4}Co_{0.2}Fe_{0.8}O_3$	LSCF
$La_{0.6}Sr_{0.4}Co_{0.2}Fe_{0.8}O_3$ (50 wt%)+$SrCe_{0.9}Yb_{0.1}O_{3-\delta}$ (50 wt%)	LSCF/10YbSC(1:1)
$La_{0.6}Sr_{0.4}Co_{0.2}Fe_{0.8}O_3$ (50 wt%)+$BaCe_{0.9}Yb_{0.1}O_{3-\delta}$ (50 wt%)	LSCF/10YbBC(1:1)
$La_{0.6}Sr_{0.4}Co_{0.2}Fe_{0.8}O_3$ (70 wt%)+$BaCe_{0.9}Yb_{0.1}O_{3-\delta}$ (30 wt%)	LSCF/10YbBC(7:3)
$La_{0.6}Sr_{0.4}Co_{0.2}Fe_{0.8}O_3$ (30 wt%)+$BaCe_{0.9}Yb_{0.1}O_{3-\delta}$ (70 wt%)	LSCF/10YbBC(3:7)

Table 4.3: Summary of the tested cathode compositions

4.3.1 Optimization of Cathode Composition and Microstructure

Composite cathode inks were prepared mixing LSCF and 10YbSC or 10YbBC powders as previously described. LSCF powder, with particle size in the 0.3-0.5 μm range, was supplied by Praxair, while 10YbSC and 10YbBC powders were prepared with a solid state reaction as described in Chapter 4.2.1 (Part B). Symmetric cells were prepared by paint brushing the cathode slurry to each side of a 20BCY pellet, drying at 150 °C for 3 h, and firing between 900 and 1100°C. The ASR was measured as previously illustrated for single phase 10YbSC and 10YbBC cathodes.

Figures 4.13a and 4.13b show the ASR vs. reciprocal temperature of single phase LSCF and composite cathodes prepared with a 1:1 weight ratio between the two phases, after sintering at 900 and 1100°C, respectively.

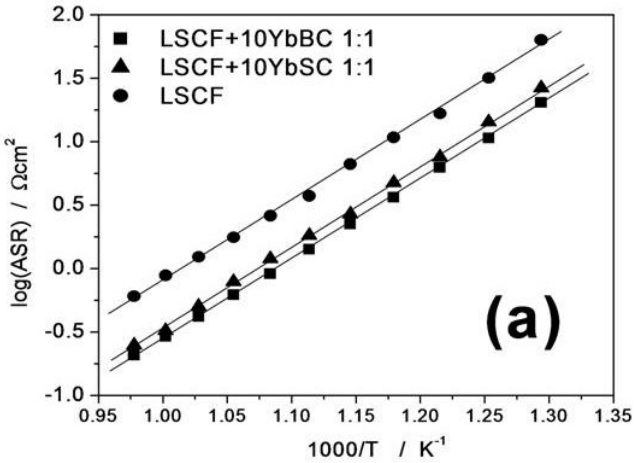

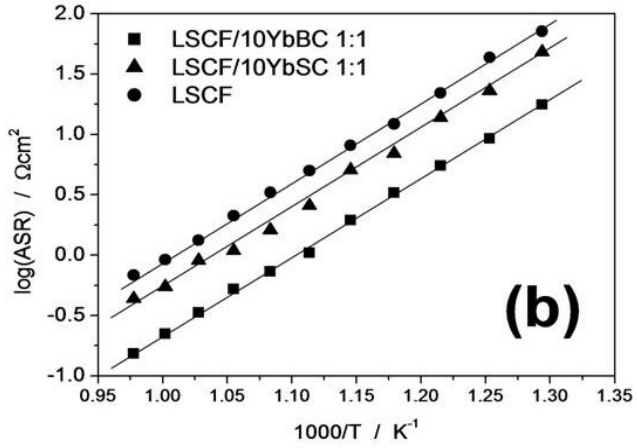

Figure 4.13: ASR vs reciprocal temperature in wet air: comparison between different electrodes, after sintering procedure at 900 °C for 6 h (a) and 1100 °C for 2 h (b).

The single-phase LSCF cathode showed larger ASR values than the composite cathodes, at both sintering temperatures of 900 and 1100°C. The improvement in the cathode performance upon addition of a proton conductor phase to the LSCF can be attributed to the extension of the TPB from a narrow region at the electrode/electrolyte interface up to a three dimensional volume that includes the whole cathode bulk, as illustrated in figure 4.14.[11] Furthermore, the use of a composite cathode reduces the thermal expansion mismatch between the electrode and the electrolyte [38] (the thermal expansion coefficient being 11.2 10^{-6} K^{-1} for $BaCeO_3$[10] and 14-15.2 10^{-6} K^{-1} for LSCF [2]), thereby resulting in a better adhesion between the electrode and the electrolyte.

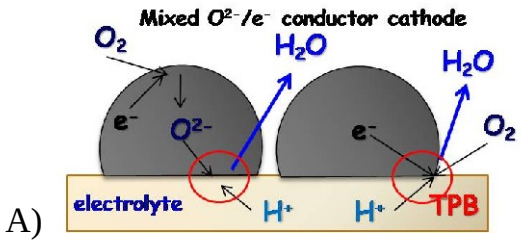

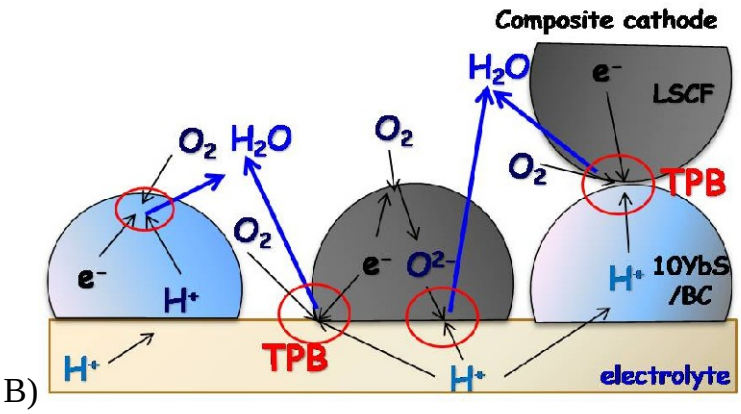

Figure 4.14: Scheme of the electrode reaction for a single phase (A) and composite cathode (B).

Interestingly, the two composite cathodes showed a different trend when the sintering temperature was increased from 900°C to 1100°C (figures 4.13a and 4.13b). LSCF/10YbBC(1:1) sintered at 1100°C showed better performance than the sample with same composition sintered at 900°C, achieving the lowest ASR values among the tested cathodes (0.33 Ωcm^2 at 700 °C). On the other hand, the ASR of the LSCF/10YbSC(1:1) cathode increased with increasing the sintering temperature. Tests of chemical reactivity between the different phases constituting the two composite cathodes were performed to understand the last finding. XRD analysis of LSCF/10YbSC(1:1) and LSCF/10YbBC(1:1) composite cathode powders was performed on samples as prepared and after the same thermal treatments performed for the sintering. Figure 4.15 shows that LSCF reacted with 10YbSC already at 900°C producing undesirable phases, and the reaction increased further after the thermal treatment at 1100°C. Differently, figure 4.16 shows that no chemical reaction occurred between LSCF and 10YbBC after heating to 1100°C. The formation of additional phases due to chemical reactions can limit the ionic migration through the cathode/electrolyte interface increasing cathode polarization.[39] Therefore, the increasing LSCF/10YbSC(1:1) resistance with increasing sintering temperature can be explained by the chemical reactivity between LSCF and 10YbSC.

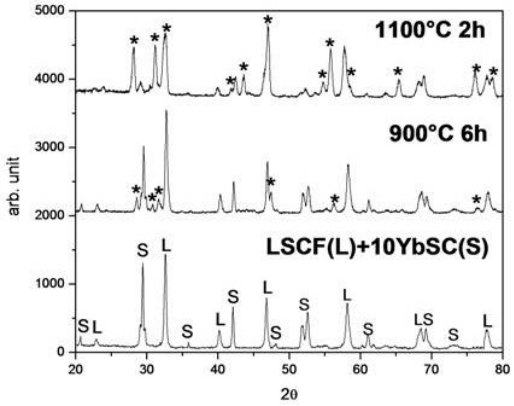

Figure 4.15: XRD patterns of LSCF/10YbSC(1:1) composite cathode powder as prepared and after thermal treatments at 900°C and 1100°C for 2 h.

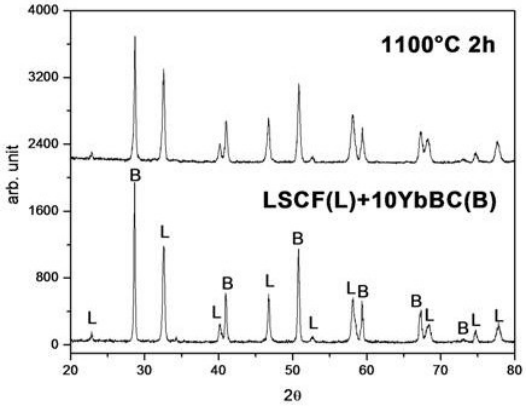

Figure 4.16: XRD patterns of LSCF/10YbBC(1:1) composite cathode powder as prepared and after thermal treatments at 1100°C for 2 h.

On the basis if the chemical reactivity results, only the LSCF/10YbBC composite cathode was further optimized.

The chemical reactivity between LSCF, LSFC/10YbBC and BCY20 electrolyte was further investigated by mixing the cathode and the electrolyte powders in a 1:1 weight ratio and then heating the mixture to 1100°C for 2 h. After the thermal treatment, no changes in the diffraction plot were recorded, suggesting that these materials are chemically compatible at 1100°C.

To investigate the cathode microstructure, cross section SEM micrographs of the LSCF and LSCF/10YbBC(1:1) cathodes at the electrolyte interface were acquired (figure 4.17), for samples sintered at 900°C and 1100°C. The thickness of the electrode layers was found to be in the range of 15-20 μm for all the samples.

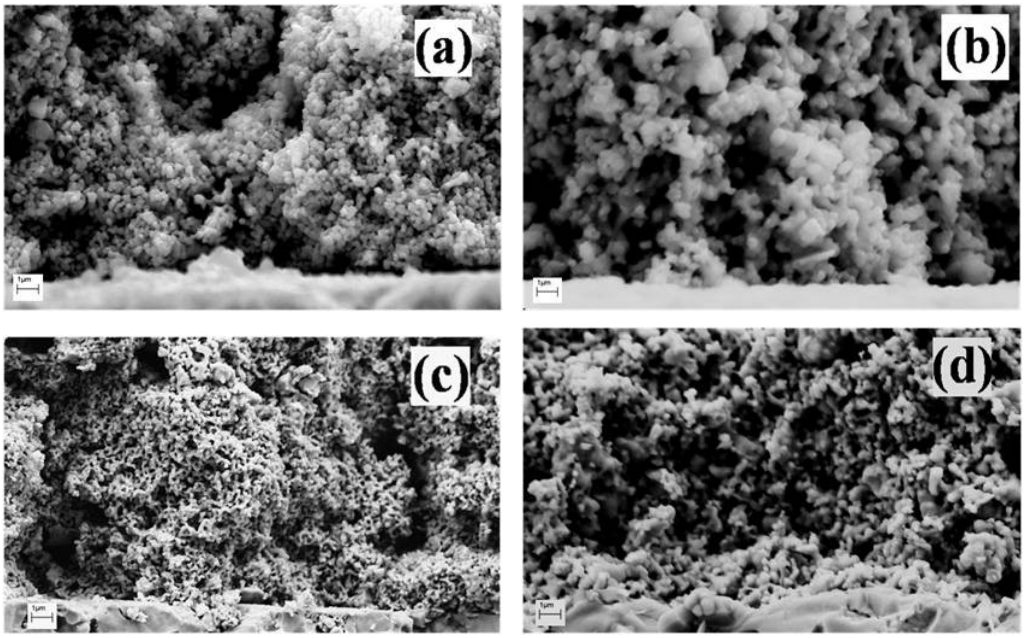

Figure 4.17: SEM micrographs showing cross section of LSCF cathode sintered at 900°C for 6 h (a) and at 1100°C for 2 h (b) and of LSCF/10YbBC(1:1) composite cathode sintered at 900°C for 6 h (c) and at 1100°C for 2 h (d).

Considering figure 4.17a, it is evident that the contact of the LSCF cathode sintered at 900°C with the electrolyte was very poor. The adhesion of the LSCF cathode with the electrolyte slightly improved after firing at 1100°C (figure 4.17b), but with the concomitant formation of a coarsened microstructure which reduces the porosity for gas diffusion and the surface area of the gas-solid interface (TPB). The occurrence of both effects could account for the weak dependence of the LSCF resistance with sintering temperature, as shown in Figs. 4.13a and 4.13b. Furthermore, according to the microstructure analysis, the larger LSCF resistance with respect to the composite cathode (fig. 4.13) can be explained by several factors, such as the formation of coarser microstructure which limits the

gas diffusion and decreases TPB surface, and thermal mismatch between the LSCF and the electrolyte which reduces the contact between them. The adhesion of LSCF/10YbBC(1:1) composite cathodes with the substrate was much better than that of the LSCF cathodes fired at the same temperature. Furthermore, the introduction of the 10YbBC phase allowed hindering the grain growth of LSCF, maintaining a porous cathode microstructure also after sintering at the higher temperature. Such microstructure improved the electrode/electrolyte adhesion. In fact, the composite cathode sintered at 1100°C (figure 4.17d) presented only slightly larger particle size than the relative sample sintered at 900°C (figure 4.17c), but with improved adhesion with the electrolyte pellet. This accounts for its lower ASR with respect to the same cathode composition sintered at 900°C (figure 4.13).

Different cathode compositions were tested by changing the weight ratio between LSCF and 10YbBC. Figures 4.18a and 4.18b show the effect of the 10YbBC weight fraction on the ASR for the LSCF/10YbBC cathodes over the 550-750 °C temperature range.

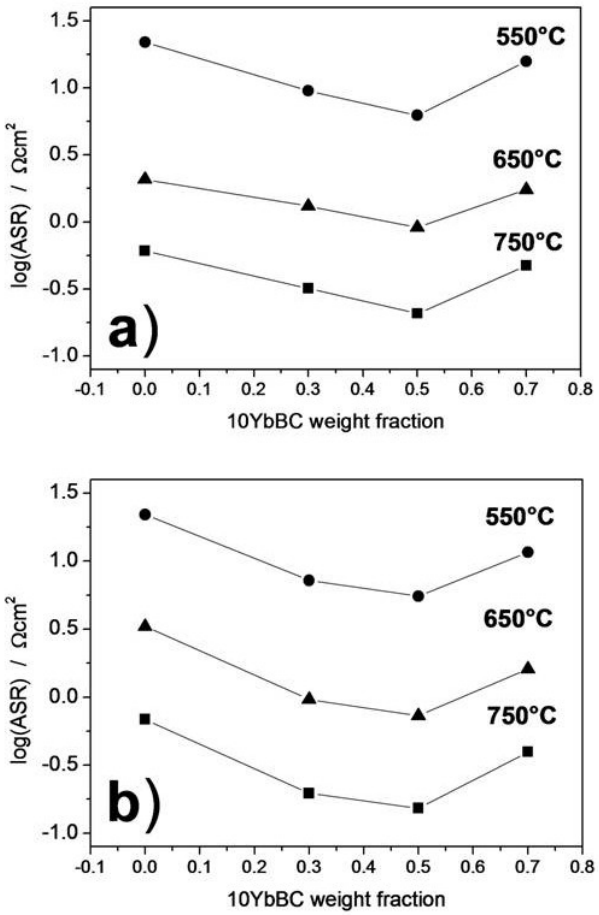

Figure 4.18: Effect of the electrode composition (10YbBC wt%) on the ASR of LSCF/10YbBC composite cathodes, sintered at 900°C for 6 h (a) and at 1100°C for 2 h (b).

For both sintering temperatures, the lowest ASR was achieved with the composite cathode containing 50 wt% 10YbBC. Slightly larger ASR values were observed for the composite cathode containing 30 wt% 10YbBC, while the ASR increased significantly with 70 wt% of 10YbBC. The latter results can be explained considering that large amount of 10YbBC phase could strongly reduce the cathode catalytic activity and electronic conduction, which are mainly related to the LSCF phase. However, single phase LSCF showed larger ASR even when compared with the poorer performing composite cathode (10YbBC 70 wt%), confirming the essential role of the mixed H^+/e^- conductive phase. The activation energy values for all the tested cathode compositions were very similar (1.26-1.30 eV) suggesting the same reaction mechanisms.

Figures 4.19a, b, c, and d show the typical EIS plots in the complex impedance plane acquired in wet air at 600°C for the composite and single-phase LSCF cathodes.

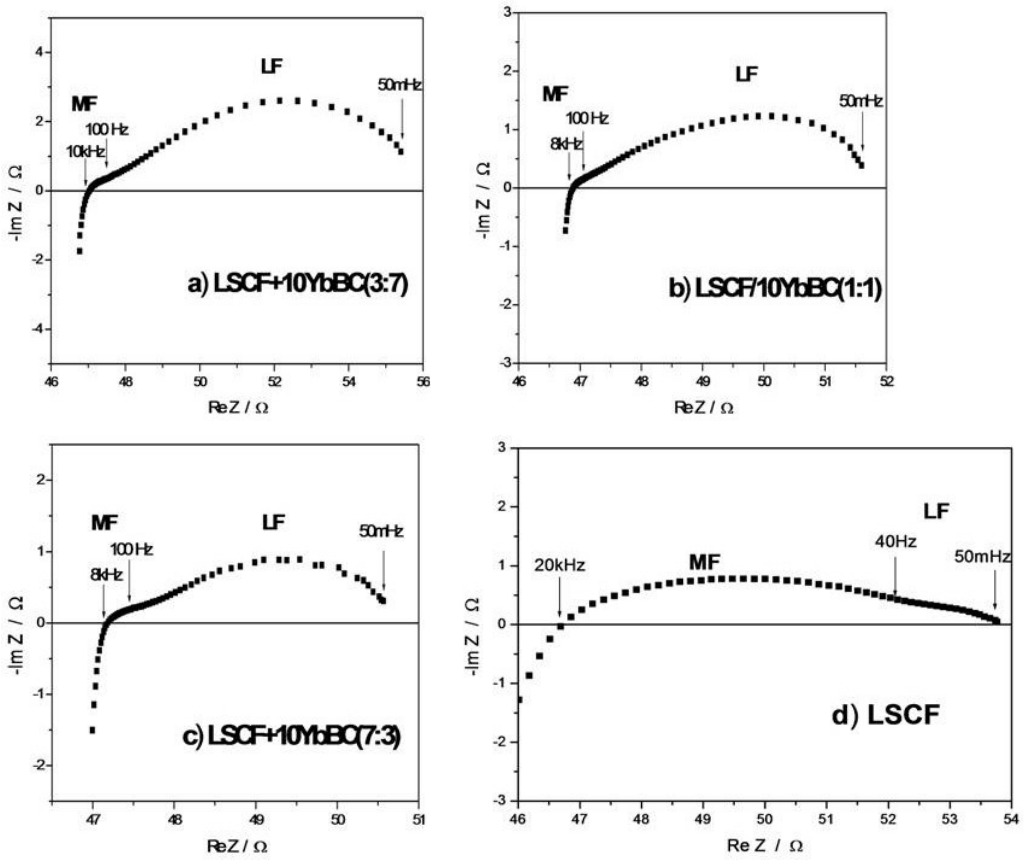

Figure 4.19: Typical complex impedance plane plots acquired in wet air at 600°C for the composite and single-phase LSCF cathodes, labeled in the figure.

At very low temperature (around 200°C), two semicircles were present in the high frequency range of cathode impedance plane plots, attributed to the contribution of bulk and grain boundary electrolyte resistances. Increasing the temperature, the two arcs merged into a depressed semicircle and

finally led to a high frequency resistance in series with an inductive contribution, coming from the measuring device and the electrical connections. In the low frequency range of the EIS plots two depressed semicircles were observed between 300 and 750°C. As shown in figures 4.19a, b, and c, a small semicircle appeared in the middle frequency (MF) range together with a larger semicircle at lower frequencies (LF). The EIS complex impedance plane plot of LSCF (Fig. 4.19d) also presented two semicircles, but in this case the first semicircle at middle frequencies was larger than the second one at lower frequencies.

Oxygen reduction reaction mechanism on mixed ionic-electronic electrode involves several processes, such as oxygen dissociative adsorption at the electrode surface, bulk and surface diffusion of oxygen species, gas diffusion, and charge transfer at the electrode/electrolyte interface.[40] These different reaction processes can produce different semicircles in the low frequency range of the complex impedance plane plot.

Figure 4.20 shows the ASR1 and ASR2 temperature dependence for composite cathodes with different amounts of 10YbBC wt% and for single-phase LSCF, sintered at 1100°C. ASR1 was associated to R_{MF}, while ASR2 to R_{LF}.

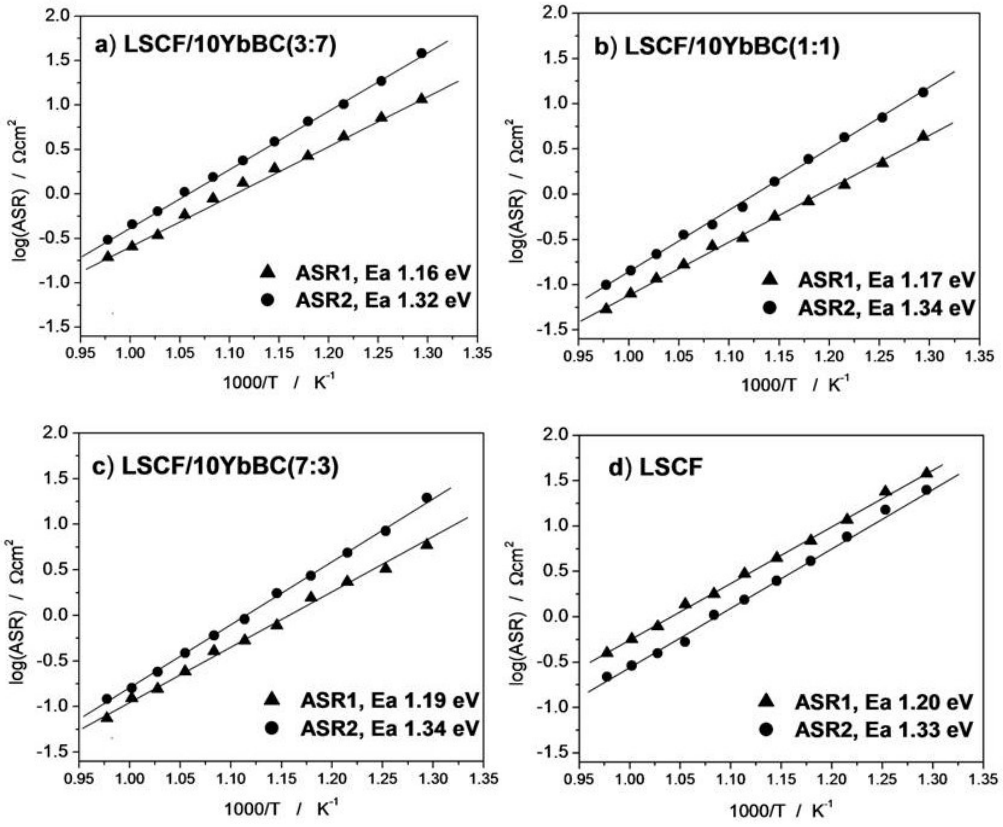

Figure 4.20:ASR1 and ASR2 temperature dependence in wet air for composite cathodes with different 10YbBC wt% and for single-phase LSCF, sintered at 1100°C for 2 h.

All the samples showed very close activation energy values, both for the ASR1 and the ASR2, suggesting that all the cathode compositions presented the same reaction mechanisms. ASR1 showed an activation energy between 1.16-1.20 eV, while ASR2 between 1.32-1.34 eV. Although for all the tested cathodes ASR1 and ASR2 did not differ significantly in the activation energy, they contributed differently to the total cathode resistance upon changes in the cathode composition. While ASR2 was larger than ASR1 in the case of the composite cathodes, the opposite was found for the single-phase LSCF cathode. These findings suggested that the rate-determining process was different for the composite and single-phase LSCF cathodes.

ASR measurements performed at different oxygen partial pressures allow the correlation of each semicircle in the complex impedance plane plot to a specific electrode process.[4,18,40] ASR is proportional to $p_{O_2}^{-n}$, where the n-value gives information about the species involved in the electrode reaction.

When an oxygen-ion conducting electrolyte is used, a $(p_{O2})^{¼}$ dependence is usually referred to the charge transfer process between the electrode and the electrolyte, while a linear relationship between the ASR and $(p_{O_2})^{½}$ is considered as the contribution of the adsorption/diffusion process. [40] In a fuel cell based on a proton conducting electrolyte, the overall cathode reaction is different from the one occurring in a fuel cell using an oxygen-ion electrolyte. Furthermore, models about ASR dependence on p_{O_2} are scarce for these materials. However, the processes involving oxygen adsorption and diffusion take place also in a mixed ionic/electronic conductor cathode working on a proton conductor electrolyte. In fact, as in the case of a cathode working on an oxygen-ion electrolyte, oxygen atoms must diffuse into the electrochemically active sites, where they can react with protons and electrons to generate water. Therefore, it seems reasonable to assume that for a proton conductor based SOFC the ASR dependence on $(p_{O2})^{½}$ comes from the same adsorption/diffusion process on the electrode surface, as it is for an oxygen-ion fuel cell. Moreover, Uchida et al. have reported that charge transfer processes at a proton conducting electrolyte might show a p_{O_2} dependence in the $0 \leq n \leq 0.5$ range.[1]

Figure 4.21 shows the ASR1 and ASR2 p_{O_2} dependence in wet air and at 700°C for LSCF/10YbBC(1:1), sintered at 1100°C. The slope of the log(ASR2) as a function of $\log(p_{O_2})$ was very close to 0.5, suggesting a correlation with the oxygen adsorption/desorption processes on the LSCF surface. This arc at lower frequency (R_{LF}) was not likely due to gas diffusion resistance because its amplitude decreased with increasing temperature.[18] The charge transfer reaction is a process occurring at higher frequency with respect to the oxygen dissociative adsorption,[15] hence the higher frequency of the semicircle related to ASR1 and the lower ASR1 dependence on p_{O_2} (n = 0.21), suggest that ASR1 can be related to the charge transfer reaction between the electrode and the electrolyte. Furthermore, the two depressed semicircles presented different capacitance, confirming that they are associated to different electrochemical processes at the cathode.[18] In particular, the first semicircle related to ASR1

presented smaller capacitance than the second one (10^{-5}-10^{-6} F instead of 10^{-1}-10^{-2} F) and a small electrode capacitance is usually associated to the electrode/electrolyte charge transfer process, while larger capacitance to surface reactions.[11] In addition, the above interpretation is consistent with the results showed in figure 4.20. For all the composite cathodes ASR2 was larger than the ASR1 (figure 4.20a, b, c), whereas for single-phase LSCF (figure 4.20d) the opposite trend was observed. Assuming that the first semicircle is associated with the charge transfer process and the second one to the oxygen adsorption, the ASR1 larger than ASR2 observed only for the single-phase LSCF cathode can be explained by the reduced TPB length, which generally results in an increased charge transfer resistance.

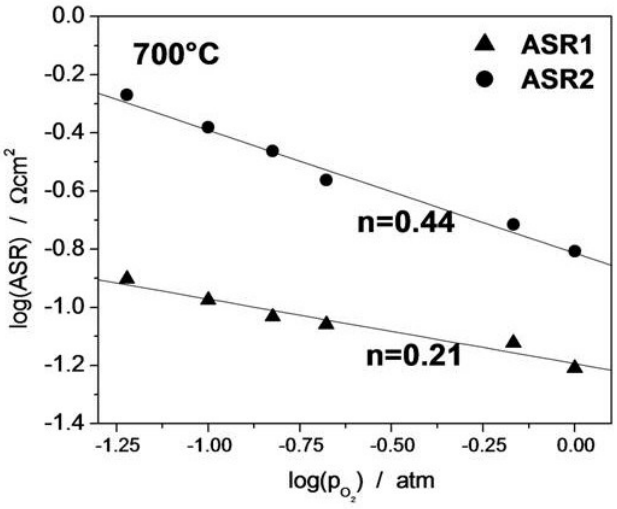

Figure 4.21: ASR1 and the ASR2 p_{O_2} dependence in wet air and at 700°C for the LSCF/10YbBC(1:1) composite cathode, sintered at 1100°C for 2 h

The larger ASR1 values for LSCF cathode indicates that for single phase cathode charge transfer reaction was the rate limiting process. In the case of the composite cathodes, the larger values of ASR2 suggest that the dissociative oxygen adsorption became the rate limiting step. Previously, Yamaura et al [4] have found that the charge transfer process was the rate limiting step for single phase LSCF cathode applied on a proton conductor electrolyte.

4.3.2 Optimization of LSCF/10YbBC(1:1) Cathode Microstructure

Besides the optimization of the material composition, an important strategy to improve the electrochemical performance of a cathode is the control of its microstructural properties. From this point of view, to obtain homogeneous and porous electrodes, the nature of the starting powders can play a very important role. An electrode microstructure with elevated porosity can lead to significant

improvements on the oxygen conducting properties. Optimizing the connectivity and size distribution between particles of each solid phase can produce larger TPB available for oxygen reduction, which leads to a decrease in polarization drop and in an improved cathode performance.[3,15] An increase in the TPB length might be achieved using nanometric grain size. The sol-gel procedure described in Chapter 1 (Part B) was used thus to synthesize LSCF and 10YbBC powders at low calcination temperature (800°C 5 h for LSCF and 1000°C 6 h for 10YbBC). FE-SEM observations confirmed that the obtained powders were about 10-50 nm in size.

Fixing the LSCF/10YbBC composition at 50-50 wt%, ASR measurements of that composite cathode, prepared from nano-sized powders, were performed in wet air. The results are shown in figure 4.22. Lower ASR values were achieved sintering the electrode at 900°C, while, in the case of cathode with larger particle size, better results were achieved at 1100°C.

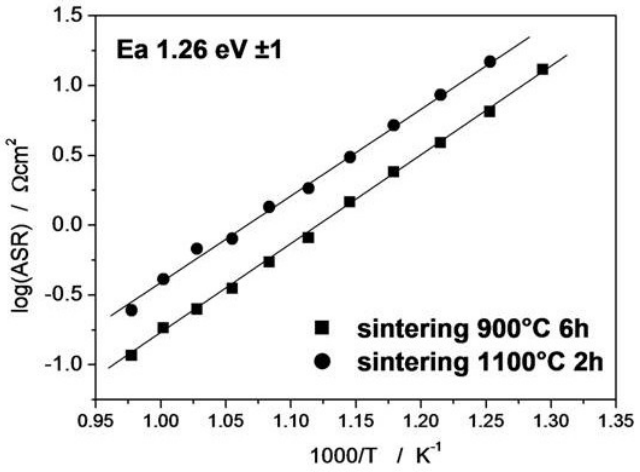

Figure 4.22: ASR vs reciprocal temperature of LSCF/10YbBC(1:1) composite cathode, prepared from nano-size powders and sintered at 900°C for 6 h and at 1100°C for 2 h.

A further attempt to improve the microstructure properties was the use of particles with different size, in particular coupling nanometric 10YbBC particles with larger LSCF particles. Also in this case the LSCF/10YbBC (1:1) composition was used and the samples were sintered at 900°C for 6 h and at 1100°C for 2 h, obtaining better result upon sintering at the higher temperature. For comparison, figure 4.23 shows the ASR of the cathodes with the same composition but prepared using powders of LSCF and 10YbBC with particle size in the range of 0.3-0.5 μm (sample A), with nanometric particle powders of both LSCF and 10YbBC (sample B), and with sub-micrometer LSCF particles and nanometer 10YbBC particles (sample C).

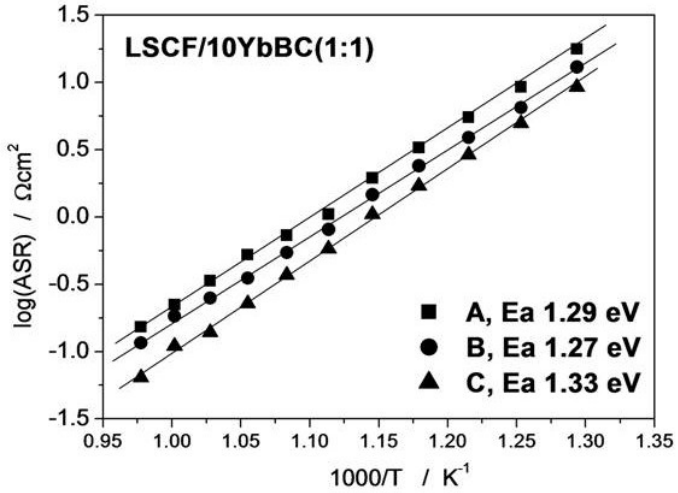

Figure 4.23: ASR vs reciprocal temperature of LSCF/10YbBC(1:1) composite cathode prepared from both LSCF and 10YbBC sub-micrometer particle powders (sample A), LSCF and 10YbBC nanometric particle powders (sample B), and sub-micrometer LSCF particles and nanometer 10YbBC particles (sample C).

As shown in figure 4.23, the composite cathodes containing at least one nano-sized particle phase (samples B and C) showed lower ASR than the one composed entirely of large particles (sample A). This result was attributed to the increased TPB length.[15]

The lowest resistance was obtained when different particle sizes were used, sintering at 1100°C for 2 h. This composite cathode showed an ASR of 0.14 Ωcm^2 at 700°C and 1 Ωcm^2 at 600°C.

Changing the ratio between the particle size, LSCF/10YbBC(1:1) composite cathode presented similar activation energies (1.30 ±3 eV) as well as similar complex impedance spectra (figure 4.24), suggesting that the reaction mechanisms did not change.

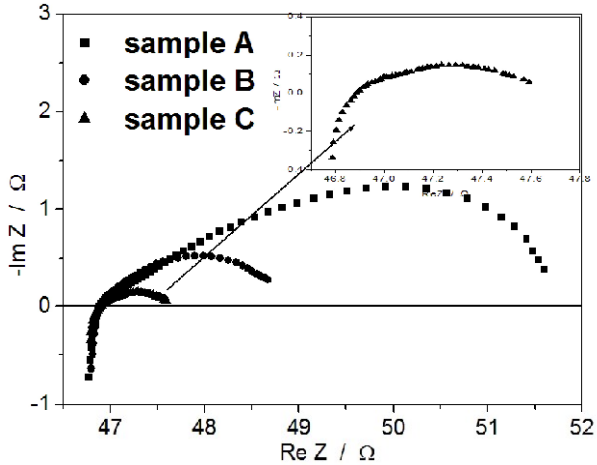

Figure 4.24: Complex impedance plane plots of composite cathode prepared from both LSCF and 10YbBC sub-micrometer particle powders (sample A), LSCF and 10YbBC nanometric particle powders (sample B), and sub-micrometer LSCF particles and nanometer 10YbBC particles (sample C) at 600°C.

Figure 4.25 shows a comparison of the ASR in wet air of the optimized LSCF/10YbBC(1:1) composite cathode (sample C), single-phase LSCF, and Pt cathode applied on 20YBC electrolyte. The composite cathode showed the lowest ASR, providing thus better performance reducing material cost if compared with Pt.

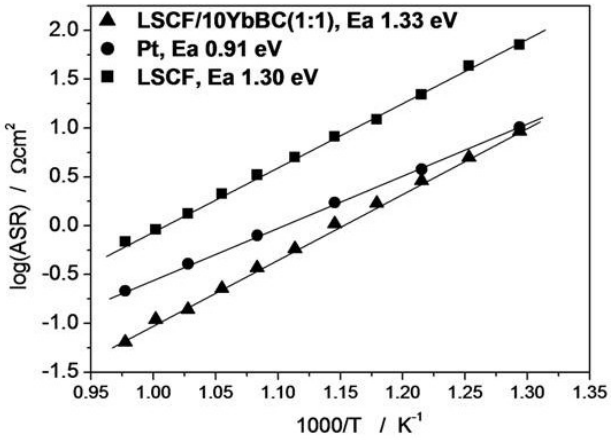

Figure 4.25: ASR vs reciprocal temperature of LSCF/10YbBC(1:1) composite cathode with different particle size, single-phase LSCF, and Pt cathode on 20YBC electrolyte

The ASR in wet oxygen of LSCF/10YbBC(1:1) composite cathode (sample C) was also measured using $BaZr_{0.8}Y_{0.2}O_{3-\delta}$ (20BZY) electrolyte. The 20YBZ pellet was prepared as described in Chapter 1 (Part 2).

The chemical reactivity between LSCF and 20YBZ was tested mixing the powders in 1:1 ratio and heating up to 1100°C. The XRD patterns of LSCF/20YBZ powder before and after the thermal treatment is shown in figure 4.26. No other peaks, except those of LSCF and 20YBZ could be observed after the treatment indicating that no chemical reactivity occurred up to 1100°C.

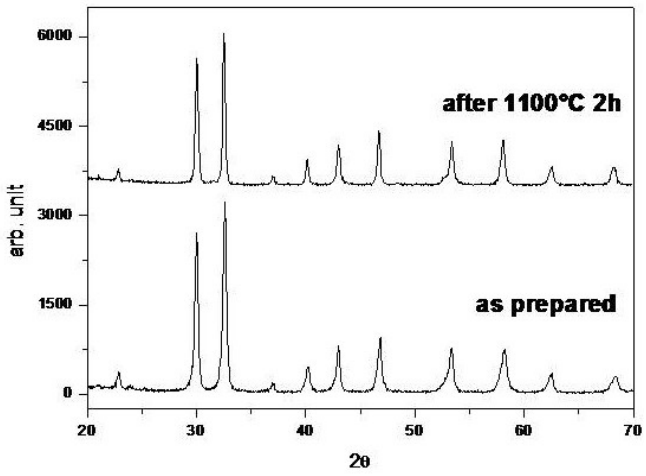

Figure 4.26: XRD patterns of LSCF and 20YBZ powders, as mixed and after heated at 1100°C for 2 h.

Figure 4.27 shows the ASR measured in wet oxygen of LSCF/10YbBC(1:1) composite cathode with different particle size (sample C) applied on 20BZYelectrolyte. For comparison, also the ASR of Pt/20YBZ interface in the same experimental conditions is reported.

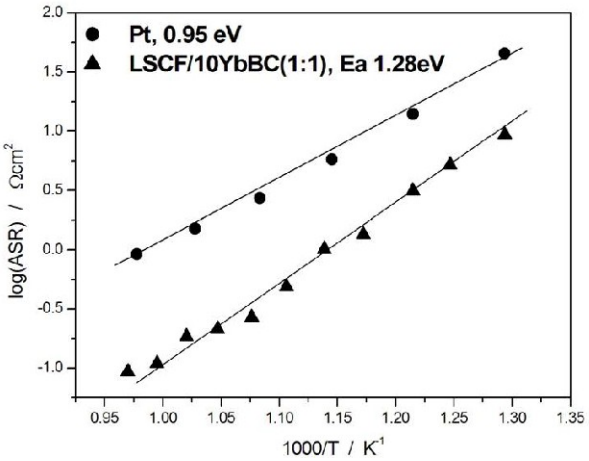

Figure 4.27: ASR vs reciprocal temperature of LSCF/10YbBC(1:1) composite cathode with different particle size, and Pt cathode on 20YBZ electrolyte

The composite cathode showed a significant lower ASR compared to Pt. The use of a composite cathode, besides increasing the reaction sites, can provide a close thermal expansion coefficient with the electrolyte with respect to Pt. The cross section analysis (figure 4.28) confirmed a good adhesion between the electrode and the electrolyte.

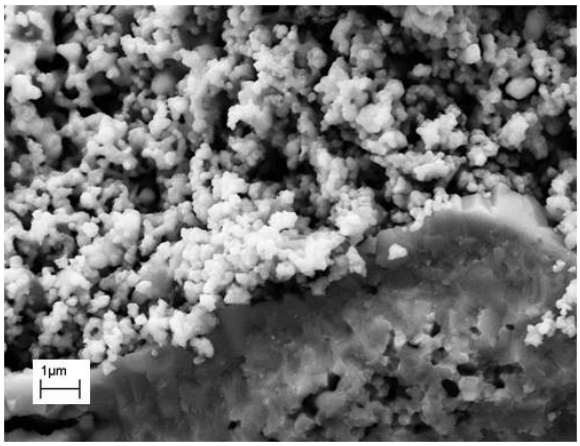

Figure 4.28: SEM micrograph of LSCF/10YbBC(1:1) composite cathode made of different particle size (sample C) on 20YBZ electrolyte, after sintering at 1100°C.

Figure 4.29 shows the ASR of LSCF/10YbBC(1:1) composite cathode (sample C) applied on 20YBC and 20YBZelectrolytes. The composite cathode did not show significant differences in the ASR values when applied on different proton conductor electrolytes. This finding makes LSCF/10YbBC(1:1) a cheaper and more efficient alternative to the Pt cathode that can actually improve the performance of IT-SOFCs based on proton conductor electrolyte.

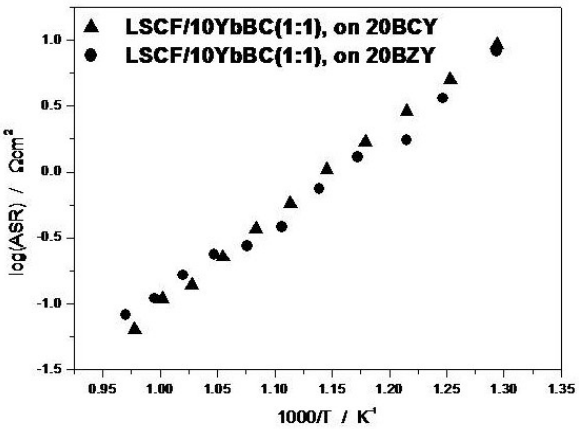

Figure 4.29: ASR of LSCF/10YbBC(1:1) composite cathode on 20YBCand 20YBZ electrolyte.

4.4 Fuel Cell Tests

To verify the superior performance of the LSCF/10YbBC(1:1) cathode with different particle sizes with respect to Pt, fuel cell tests were performed using a 20BCY electrolyte pellet (1 mm thick) with Pt electrodes, and replacing the Pt cathode with the optimized LSCF/10YbBC(1:1) cathode. Figure 4.30 shows the I-V curves of the Pt/BCY/Pt and Pt/BCY/LSCF-10YbBC cell configurations.

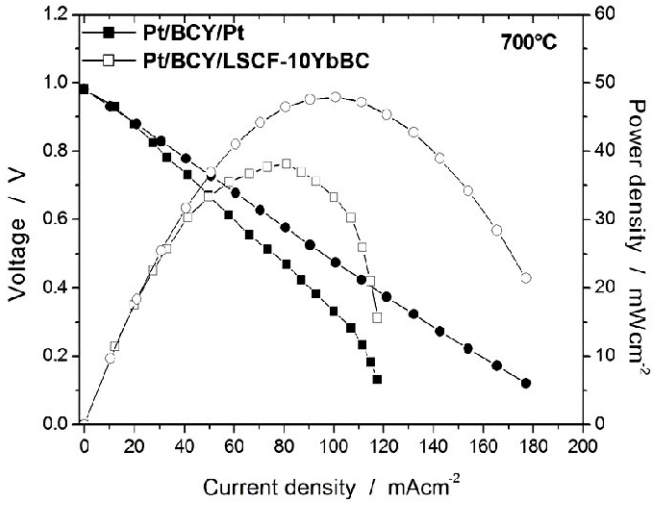

Figure 4.30: I-V curves and power density output from humidified H_2-ambient air fuel cell tests at 700°C of the Pt/BCY/Pt and Pt/BCY/LSCF-10YbBC cell configurations

The two cells showed very close open circuit voltage and activation polarization, as it was expected since the same anode and electrolyte were used. Interestingly, the two polarization curves differed both in ohmic and concentration overpotential, which are mainly caused by the ohmic electrolyte resistance and the cathode reactions, respectively. Larger ohmic overpotentials were observed for the cell with both Pt electrodes, suggesting that the choice of the electrodes affects the electrode/electrolyte interface resistivity.[41] The larger ohmic polarization observed for the Pt/BCY/Pt cell could be due to high resistivity of certain areas, such as current constriction at the electrode/electrolyte interface. Boehm and McEvoy have already observed differences in the electrical conductivity for the same proton conductor electrolyte (Yb doped strontium cerate) depending on the electrode used.[5] They suggested that some electrode may inhibit H^+ ion transfer, inducing a depletion of carriers. Regarding concentration overpotential, the smaller voltage drop at the highest current density for the cell with the LSCF/10YbBC(1:1) cathode is consistent with ASR measurements (fig. 4.25) and can be explained in terms of enhanced TPB of the composite cathode. Increasing the TPB not only the charge transfer is facilitated, but also water can be generated from the whole cathode surface so that it can more easily evaporate.

EIS measurements were performed in-situ during the fuel cell tests to further clarify this point. Figure 4.30 shows the typical EIS complex impedance plane plots for the Pt/BCY/Pt and Pt/BCY/LSCF-10YbBC cells at 700°C under open-circuit voltage conditions. The intercept with the real axis at high frequencies represents the ohmic electrolyte resistance, whereas the difference between the high frequency and low frequency intercepts with the real axis represents the sum of the electrode (anode and cathode) reaction resistances. Pt/BCY/Pt and Pt/BCY/LSCF-10YbBC cell configurations showed a similar ohmic resistance, but a significantly large difference in the electrode-reaction resistance. Since the overpotential at the anode/electrolyte interface should be the same for the two systems, the lower electrode-reaction resistance of the fuel cell using the composite cathode resulted from the better performance of the LSCF/10YbBC(1:1) cathode on the BCY electrolyte, consistent with the previous ASR measurements.

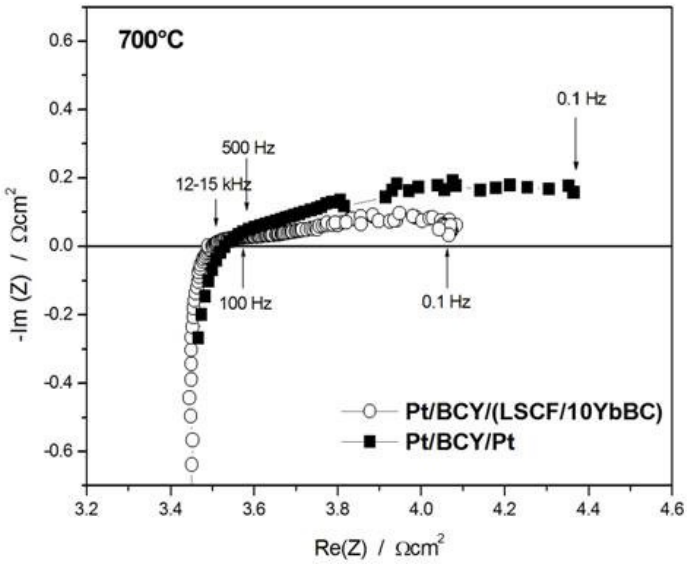

Figure 4.31: EIS plots of the Pt/BCY/Pt and Pt/BCY/LSCF-10YbBC cell configurations measured at 700°C under open circuit conditions

4.5 References

1. H. Uchida, S. Tanaka, H. Iwahara, *J. Appl. Electrochem*., 5 (1985) 93.
2. A. Esquirol, N. P. Brandon, J. A. Kilner, M. Mogensen, *J. Electrochem. Soc.*, 151 (11) (2004) A1847.
3. D.Z. De Florio, R. Muccillo, V. Esposito, E. Di Bartolomeo, E. Traversa, *J. Electrochem. Soc*, 152 (1) (2005) A88.
4. H. Yamaura, T. Ikuta, H. Yahiro, G. Okada, *Solid State Ionics*, 176 (2005) 269.
5. E. Boehm, A.J. McEvoy, *Fuel Cells*, 1 (2006) 54.
6. H. Iwahara, T. Yajima, T. Hibino, H. Ushida, *J. Electrochem. Soc.*, 140 (6) (1993) 1687.
7. T. Hibino, A. Hashimoto, M. Suzuki, M. Sano, *J. Electrochem. Soc*., 149 (11) (2002) A1503.
8. N. Maffei, L. Pelletier, A. McFarlan, *J. Power Sources*, 136 (2004) 24.
9. P. Ranran, W. Yan, Y. Lizhai, M. Zongqiang, *Solid State Ionics*, 177 (2006) 389.
10. J.R. Tolchard, T. Grande, *Solid State Ionics*, 178 (2007) 593.
11. V. Dusastre, J.A. Kilner, *Solid State Ionics*, 126 (1999) 163.
12. S.W. Tao, Q.Y. Wu, D.K. Peng, G.Y. Meng, *J. Appl. Electrochem*,. 30 (2000) 153.
13. H.L. Tuller, *Solid State Ionics*, 52 (1992) 135.
14. S. J. Song, E. D. Wachsman, S. E. Dorris, U. Balachandran, *J. Electrochem. Soc*., 150 (6), (2003) A790–A795.
15. M. Camaratta, E.D. Wachsman, *J. Electrochem. Soc.*, 155 (2) (2008) B135.
16. V.V. Kharton, A.V. Kovalevsky, A.P. Viskup, F.M. Figueiredo, A.A. Yaremchenko, E.N. Naumovich, F.M.B. Marques, *J. Eur. Ceram. Soc*., 21 (2001) 1763.
17. T. Hibino, K. Suzuki, K. Ushiki, Y. Kuwahara, M. Mizuno, Appl. Catal. 1996, 145, 297.
18. H. Zhao, L. Huo, S. Gao, *J. Power Sources*, 243 (2005) 125.
19. W. D. Kingery, H. K. Bowen, and D. R. Uhlmann, Introduction to Ceramics, p. 866, Wiley, New York (1976).
20. X. Qi, Y.S. Lin, *Solid State Ionics*, 130 (2000) 149.
21. S. Roy, I. S. Dubenko, M. Khan, E. M. Condon, J. Craig, N. Ali, *Phys. Rev*, 024419 (2005) B 71.
22. S.J. Song, H.-S. Park, *J. Mater. Sci*., 42 (2007) 6177.
23. F. Genet, S. Loridant, C. Ritter, G. Lucazeau, *J. Phys. Chem. Sol*. 60 (1999) 2009.
24. N. Bonanos, KS. Knight, B. Ellis, Solid State Ionics, 79 (1995) 161.
25. P.J. Shlichta, Solid State Ionics, 28-30 (1988) 480.
26. J. Ranlov, B. Lebech, K. Nielsen, J. Mater. Chem., 5 (1995) 743.
27. J. Ranlov, K. Nielsen, J. Mater. Chem, 4 (1994) 867.
28. J.X. Wang, L.P. Li, B.J. Campbell, Z. Lv, Y. Ji, Y.F. Xue, W.H. Su, *Materials Chemistry and Physics*, 86 (2004) 150.

29. H. Iwahara, T. Yajima, H. Ushida, *Solid State Ionics*, 70/71 (1994) 267.
30. V.V. Kharton, I.P. Marozau, G.C. Mather, E.N. Naumovich, J.R. Frade, *Electrochim. Acta*, 51 (2006) 6389.
31. P. Pasierb, M. Wierzbicka, S. Komornicki, M. Rekas, *J. Power Sources*, 173 (2007) 681.
32. . Iwahara, T. Yajima, T. Hibino, H. Ushida, *J. Electrochem. Soc*, 140 (6) (1993) 1687.
33. N. Bonanos, K.S. Knight, B. Ellis, *Solid State Ionics*, 79 (1995) 161.
34. N. Bonanos, *Solid State Ionics*, 53-56 (1992) 967.
35. H. Iwahara, *Solid State Ionics*, 77 (1995) 289.
36. N.Bonanos, B.Ellis, M.N. Mahmood, *Solid State Ionics*, 28-30 (1988) 579.
37. W. Wang, A. V. Virkar, *J. Electrochem. Soc*., 151 (2004) A1565.
38. C. Fu, K. Sun, N. Zhang, X. Chen, D. Zhou, *Electrochimica Acta*, 52 (2007) 4589.
39. V. Esposito, E. Traversa, E.D. Wachsman, J. *Electrochem. Soc*., 152 (12) (2005) A2300.
40. A. Ringuedè, J. Fouletier, *Solid State Ionics*, 139 (2001) 167.
41. B. White, E. Traversa, E.D. Wachsman, *J. Electrochem. Soc*., 155 (2008) J11.

Conclusions

The primary objective of the research was the development of a stable highly-conductive electrolyte and better performing electrodes for lower temperature SOFCs.

The first approach of the present work aimed to improve the electrochemical performance of $BaZrO_3$ based electrolytes producing powders of $BaZr_{0.8}Y_{0.2}O_{3-\delta}$ (BZY) with controlled compositional homogeneity and microstructure using a sol–gel synthetic method. The optimized sol–gel procedure allowed the reduction of the diffusion path down to nanometric scale, and thus required low calcination temperatures. The performance of the synthesized BZY proton conductor was examined in terms of chemical stability, electrical conductivity and operation in fuel cell conditions.

To further improve the electrochemical performance of barium zirconate electrolyte, solid solutions between barium cerate and barium zirconate were developed synthesizing different $BaZr_{0.8-x}Ce_xY_{0.2}O_{3-\delta}$ compounds ($0.0 \leq x \leq 0.8$). Among the tested electrolytes, $BaZr_{0.5}Ce_{0.3}Y_{0.2}O_{3-\delta}$ represented the best compromise between high proton conductivity and chemical stability. The above electrolyte was able to produce power density output more than twice than BZY, maintaining almost the same chemical stability.

Further improvement in HTPC electrolyte performance was obtained following a different approach. A sintered Y-doped barium cerate (BCY) pellet was protected with a thin BZY layer, grown by pulsed laser deposition. The overall performance of the bilayer electrolyte turned out to be of great interest for practical use in IT-SOFCs. The promising performance of this bilayer electrolyte rose from the very good crystallographic matching at the interface between the two materials, as well as the microstructure properties of the protecting layer in terms of uniformity, density and filling factor.

Both in the case of $BaZr_{0.5}Ce_{0.3}Y_{0.2}O_{3-\delta}$ and the bilayer electrolyte, the measured fuel cell performances were negatively affected by the Pt/electrolyte interfaces. For this reason the development of a superior cathode appeared crucial to make IT-SOFCs based on proton conductors competitive with the more established SOFCs using oxygen-ion conductor electrolytes.

To explore different cathode materials with respect to the most commonly used for proton conductor electrolytes, such as platinum or cobalto-ferrites, mixed H^+/e^- conductor and composite cathodes were investigated. Firstly, $BaCe_{0.9}Yb_{0.1}O_{3-\delta}$ (10YbBC) and $SrCe_{0.9}Yb_{0.1}O_{3-\delta}$ (10YbSC) mixed H^+/e^- conductors were tested. However, the measured area specific resistance (ASR) of these cathodes was extremely large, probably because of their too low electronic conductivity. Therefore, $La_{0.6}Sr_{0.4}Co_{0.2}Fe_{0.8}O_{3-\delta}$ (LSCF), which presents high electronic conductivity, was combined with 10YbSC or 10YbBC to form composite cathodes. LSCF was chosen also because it allows faster oxygen surface exchange being a mixed O^{2-}/e^- conductor. The lowest ASR values (0.139 Ωcm^2 at 700°C and 1 Ωcm^2 at 600°C) were achieved with the composite cathode made of LSCF and 10YbBC in a 1:1 ratio. On the contrary, the composite cathode made of LSCF and 10YbSC showed poor

performance because of chemical reactivity between the two phases. Single phase Pt and LSCF cathodes were tested for comparison and they showed higher interfacial resistance than LSCF/10YbBC(1:1) composite cathode. This finding clearly suggests the importance of the proton conductor phase within the electrode, which actually could increase the triple phase boundary (TPB) density and so improve the cathode performance. LSCF/10YbBC(1:1) was also tested in fuel cells experiments confirming its superior performance with respect to Pt. Therefore, the developed composite cathode represents a cheaper and more efficient alternative to the Pt cathode that can actually improve the performance of IT-SOFCs based on proton conductor electrolytes.

List of Papers

1. **E. Fabbri,** S. Licoccia, E. Traversa, E. D. Wachsman "*Composite Cathodes for Application in Intermediate Temperature Solid Oxide Fuel Cells (IT-SOFCs) based on a Proton Conducting Electrolyte"*
   Fuel Cells, submitted

2. **E. Fabbri**, S. Licoccia, E. Traversa, E. D. Wachsman "*Mixed Protonic-Electronic Conductors as Cathode Materials for Proton Conducting Electrolytes in Intermediate Temperature Solid Oxide Fuel Cells (IT-SOFCs)"*
   Journal of Electrochemical Society, 156 (1) (2009) B38-B45.

3. **E. Fabbri**, D. Pergolesi, A. D'Epifanio, E. Di Bartolomeo, G. Balestrino, S. Licoccia, and E. Traversa "*Design and Fabrication of a Chemically-Stable Proton Conductor Bilayer Electrolyte for Intermediate Temperature Solid Oxide Fuel Cells (IT-SOFCs)*"
   Energy Environ. Sci., 1 (2008) 355-359.

4. **E. Fabbri**, A. D'Epifanio, E. Di Bartolomeo, S. Licoccia and E. Traversa, "*Tailoring the chemical stability of* $Ba(Ce_{0.8-x}Zr_x)Y_{0.2}O_{3-\delta}$ *protonic conductors for Intermediate Temperature Solid Oxide Fuel Cells (IT-SOFCs)*"
   Solid State Ionics**,** 179 (2008) 558–564.

5. D'Epifanio, **E.Fabbri**, E. Di Bartolomeo, S.Licoccia and E.Traversa, "*Design of* $BaZr_{0.8}Y_{0.2}O_{3-\delta}$ *protonic conductor to improve the electrochemical performance in Intermediate Temperature Solid Oxide Fuel Cells (IT-SOFC).*
   Fuel Cells, 8 (1) (2008)69-76.

6. D'Epifanio, B. Mecheri, **E. Fabbri**, A. Rainer, E. Traversa, and S. Licoccia, *"Composite Ormosil/Nafion Membranes as Electrolytesfor Direct Methanol Fuel Cells"*
   Journal of The Electrochemical Society**,** 154 (11) (2007) B1148-B1151.

7. **E. Fabbri**, A. D'Epifanio, E. Di Bartolomeo, S. Licoccia and E. Traversa *"*$BaCe_{1-x-y}Zr_xY_yO_{3-\delta}$ *protonic conductors for Intermediate Temperature Solid Oxide Fuel Cells (IT-SOFCs)"*
   ECS Trans. 6, (17) 23 (2008) Editor(s): E. Wachsman, M. Heben, A. Manivannan, P. Maupin, V. Ramani, M. Williams.

8. D'Epifanio, **E. Fabbri**, E. Di Bartolomeo, S. Licoccia, and E. Traversa *"Synthesis and characterization of $BaZr_{0.8}Y_{0.2}O_{3-\delta}$ protonic conductor for Intermediate Temperature Solid Oxide Fuel Cells (IT-SOFCs)"*
   Solid-State-Ionics 2006, MRS Symposium Proc. Vol. 972, Materials Research Society, Warrendale, PA 2007, pp. 31-36, Editor(s): E. Traversa, T.R. Armstrong, C. Masquelier, Y. Sadaoka.

9. D'Epifanio, **E. Fabbri,** E. Di Bartolomeo, S. Licoccia and E. Traversa "*$BaZr_xY_{1-x}O_{3-\delta}$ and $BaCe_{1-x-z}Zr_xY_zO_{3-\delta}$ proton conductors for Intermediate Temperature Solid Oxide Fuel Cells (IT-SOFCs)*"
   ECS Trans. **7**, (1) 2337 (2007) Editor(s): K. Eguchi, J. Mizusaki, S. Singhal, H. Yokokawa.